

DISSERTATION

COUPLING ELECTROCHEMISTRY AND MICROFLUIDICS FOR BIOSENSOR
DEVELOPMENT

Submitted by

Rachel M. Feeny

Department of Chemistry

In partial fulfillment of the requirements

For the Degree of Doctor of Philosophy

Colorado State University

Fort Collins, Colorado

Fall 2016

Doctoral Committee:

Advisor: Charles S. Henry

Alan Van Orden
Justin B. Sambur
Matthew J. Kipper

Copyright by Rachel Marie Feeny 2016

All Rights Reserved

ABSTRACT

COUPLING ELECTROCHEMISTRY AND MICROFLUIDICS FOR BIOSENSOR DEVELOPMENT

Biosensors are valuable analytical tools across both scientific and medical fields. Improving and miniaturizing biosensors is an area of great interest in academic, medical, and diagnostic settings. There is a constant need to improve these systems by increasing accessibility through lower costs, greater portability, and enhanced ease-of-use. Interfacing microfluidics and electrochemical methods shows great potential to address these needs. The work described in this thesis aims to address gaps in biosensor development, including increasing accessibility and improving sensing capabilities such as sensitivity, selectivity, and resolution, by combining electrochemistry and microfluidics to develop new tools for use in a range of biosensor systems.

The primary focus of this research was to couple electrochemical detection methods with microfluidic devices for bioanalytical applications. Two main topics are reported. The first is a fluid transport mechanism employing the gas permeability of poly(dimethylsiloxane) (PDMS). Degassed PDMS pumps provide a simple, portable, inexpensive method to generate controlled fluid flow in a microfluidic device to transport a sample to electrodes for electrochemical detection.

The second topic reported does not aim to address cost or portability of the system, but rather focuses on improving the capabilities of electrode arrays as chemical imaging platforms. In this work, a platinum microelectrode system was developed for biomarker detection, primarily nitric oxide and norepinephrine. Microfluidic devices interfaced directly with the electrodes provided precise control of fluid delivery to the sensors enabling both localized control of

chemical concentrations as well as selective chemical stimulation of living tissue. The microelectrodes, when arranged in a high-density array, provided a platform capable of achieving electrochemical biomarker detection and imaging from live tissue slices with high spatiotemporal resolution.

Both technologies described required the effective interfacing of microfluidic devices with electrochemical sensors to generate biomarker detection platforms. Custom microfluidic systems were developed to directly integrate biological samples into the platforms, including dried serum spots on a filter paper matrix and live *ex vivo* murine adrenal slices embedded in agarose. To achieve reproducible biomarker detection in complex biological matrices, electrochemical cleaning methods were developed and utilized for electrode maintenance. All of the tools described in this thesis were designed to address specific applications, but were also intended to be translatable to other systems. The degassed PDMS pump could be used as a fluid transport mechanism for other microfluidic devices, improving the simplicity and portability of systems that could otherwise be limited by external pumping equipment. Similarly, the strategies described for interfacing microfluidic devices with the reported electrode arrays and platinum microelectrodes could be applied to other silicon microchips to accomplish precise control of fluid delivery to the electrodes. The technology developed to generate an electrochemical imaging platform could be further pursued to achieve a high level of chemical selectivity by employing alternative waveforms, such as fast scan cyclic voltammetry, or electrode modifications to better elucidate the role of chemical gradients in biological systems. All of these tools, when applied to other bioanalytical platforms, could continue to advance the field of biomarker detection using microfluidic systems.

ACKNOWLEDGMENTS

I would first like to thank my advisor, Dr. Chuck Henry, for his mentorship and support during my time in graduate school. His investment in and dedication to my education, research projects, and professional future have had a significant impact on what I have been able to achieve while I have been in his group. I am incredibly grateful for all of the opportunities that Chuck has provided for me, and truly appreciate that he has made my graduate school experience enjoyable under his guidance.

Secondly, I would like to thank John Wydallis for his support throughout graduate school. His research assistance was invaluable during our collaborative research projects, and his humor and optimism made long hours in the lab more enjoyable. John's support and encouragement helped me overcome the challenges I faced during my graduate education, and I am thankful to have shared my time at Colorado State University with him.

Next, I would like to thank all of the faculty, research scientists, post docs, international scholars, graduate students, and undergraduates with whom I have worked on collaborative projects during my graduate studies, including Dr. Tom Chen, Dr. Stuart Tobet, Dr. Melissa Reynolds, Dr. Scott Noblitt, Dr. Meghan Mensack, Tamsiri Songjaroen, William Wilson, Tucker Kern, Lang Yang, William Tedjo, Jasmine Nejad, Luke Schwerdtfeger, Chad Eitel, Stacy Willett, Nicole Puissant, and Alison Bailey. Their research assistance and support was critical to the success of the projects, and I am grateful for the contributions from each of them.

I would also like to thank all of the members of the Henry Laboratory, current and past, with whom I have had the pleasure of working. The support, collaboration, and teamwork both in and out of the lab have been remarkable, and I am fortunate to have had the opportunity to share my time in graduate school with each of them.

Finally, I would like to thank my parents, siblings, family, and friends for their extensive support and encouragement throughout my entire education. I have had them to turn to

throughout every step of my journey, and owe my accomplishments to them. I am incredibly grateful for everything that they have done for me, and know that I would not be where I am today without their support.

TABLE OF CONTENTS

Abstract.....	ii
Acknowledgments.....	iv
Chapter 1: Introduction	1
References.....	7
Chapter 2: Development of a Passive Pumping System for Microfluidic Devices Using Degassed PDMS	11
Introduction	12
Materials and Methods.....	14
PDMS Microfluidic Device Fabrication	15
Carbon Paste Electrode Fabrication and Modification	16
PMMA Microfluidic Device Fabrication.....	17
PDMS Pumping Mechanism Design and Fabrication	18
Design and Fabrication of 3D Printed Manifold.....	20
Flow Rate Experimental Protocol.....	20
Results and Discussion.....	21
Conclusions	32
References.....	34
Chapter 3: Degassed PDMS Pump for Controlled Extraction from Dried Filter Samples in Microfluidic Devices	36
Introduction	37
Materials and Methods.....	39
Materials and Sample Preparation.....	39
Microfluidic Design and Fabrication	40
Results and Discussion.....	44

Conclusions	48
References.....	50
Chapter 4: Label-Free Detection of C-Reactive Protein Using an Electrochemical DNA	
Immunoassay	52
Introduction	53
Material and Methods	55
Materials and Chemicals.....	55
Electrode Fabrication	55
Electrode Modification.....	56
ssDNA-anti-CRP Hybridization and CRP Detection on Au Electrode.....	57
Electrochemical Measurements	58
Results and Discussion.....	59
CRP Detection.....	59
Fluorescence Assay.....	61
Calibration Curve and CRP Detection in Serum Samples	62
Conclusions	63
References.....	65
Chapter 5: Analysis of Nitric Oxide from Chemical Donors Using CMOS Platinum	
Microelectrodes	69
Introduction	69
Experimental	71
Materials and Instrumentation.....	71
Design and Fabrication of Microfluidic Device	72
Preparation of DETA/NO.....	74
Electrochemical Characterization Using DPV	74
Electrochemical Cleaning of Electrodes.....	74

Hydrodynamic Voltammograms	75
Sensor Response.....	76
NO Concentration Validation by Chemiluminescence	76
Results and Discussion.....	76
Differential Pulse Voltammetry of DETA/NO	76
Electrode Fouling	77
Effect of Applied Potential	80
Sensor Response.....	81
Conclusions	82
References.....	84
 Chapter 6: Spatiotemporal Norepinephrine Mapping Using a High-Density CMOS	
Microelectrode Array.....	87
Introduction	88
Experimental	90
Materials and Instrumentation	90
Electrode Array Design, Fabrication, and Operation.....	91
Fabrication of Microfluidic Devices.....	100
Diffusion of Norepinephrine Across a Subarray	102
Norepinephrine Diffusion Across Array	103
Bimodal Distribution of Norepinephrine.....	103
Results and Discussion.....	104
Diffusion of Norepinephrine Across a Subarray	104
Norepinephrine Diffusion Across Array	106
Bimodal Distribution of Norepinephrine.....	109
Conclusions	112
References.....	114

Chapter 7: Electrochemical Spatiotemporal Imaging of Neurotransmitter Release from Live Adrenal Tissue Using a High-Density Electrode Array with Amperometric Detection	117
Introduction	118
Experimental	120
Materials and Instrumentation	120
Electrode Array and Supporting Electronics	120
Adrenal Tissue Slice Preparation	121
Microfluidic Device Fabrication	122
Interfacing with Upright Microscope	126
Stimulation Procedures	127
Data Collection and Analysis	129
Results and Discussion.....	130
Conclusions	138
References.....	140
Chapter 8: Development of a Multi-Assay System for Detection of Feline Immunodeficiency Virus from Dried Blood Spots	142
Specific Aims	142
Background and Significance	143
Research Design and Methods.....	145
Summary and Outcomes	154
References.....	155
Chapter 9: Conclusion	158
Future Directions.....	159
References.....	163

CHAPTER 1. INTRODUCTION

Development of new biosensors to provide diagnostic platforms with rapid, sensitive analysis of biological samples for specific applications has been of long-standing interest. Biological processes are driven by a wide range of chemical signals, which govern processes ranging from cellular movement and communication to disease progression, among many others.¹⁻³ The ability to detect the biomarkers that drive these processes is essential to understanding the systems and how they are functioning. There are a wide range of existing techniques for detecting biomarkers, including fluorescence,⁴⁻⁷ colorimetric,⁸⁻¹¹ and electrochemical methods.¹²⁻¹⁴ Each technique has inherent advantages and limitations. Fluorescence detection is highly sensitive, providing low detection limits for relevant biomarkers. It is, however, limited to species that are either natively fluorescent or modified with fluorescent tags. Colorimetric methods are generally simple and inexpensive, but often rely on indicators or complexing agents to generate a colorimetric response to biomarkers, resulting in lower sensitivity or higher limits of detection. Electrochemistry provides a sensitive technique capable of detecting biologically relevant biomarker concentrations in complex matrices while maintaining a high degree of specificity. While electrochemical detection methods are limited to analytes that are electrochemically active, electrode modifications or mediating reactions can be incorporated to expand the library of detectable species.^{15, 16} Electrochemical biomarker detection is tunable to specific applications due to the variety of electrochemical methods available, such as amperometry and voltammetry. Each method offers different strengths, which can be selected for optimized detection for each application.

Tunability in electrochemical biomarker detection also lies in the fabrication of the electrochemical system. Different materials can be incorporated into the system for use as electrodes. Biomarker detection has been accomplished using a range of electrode materials, including precious metals such as platinum and gold,¹⁷⁻¹⁹ carbon-based materials such as

graphite,²⁰⁻²² carbon nanotubes,^{23, 24} and diamond,²⁵ and organic materials such as silk.²⁶ Each material has benefits and downfalls in biomarker detection applications, including ease of modification, potential window, severity of biofouling, robustness, and cost. Selection of the appropriate material for individual applications can provide highly optimized systems for biomarker detection.

Biological matrices are complex chemical systems, however, making selective biomarker detection difficult. Multiple electrochemically active interferents are present at high concentrations in these types of samples, including catecholamines, ascorbic acid, and uric acid, among many others.^{23, 24, 27-31} Electrochemistry offers multiple detection techniques through control of waveform that can improve detection specificity. By tuning the applied potential in amperometry or using voltammetry techniques, the selectivity of the method can be improved to mitigate the effects of electrochemically active interferents. The next challenge to address is integration of electrochemical sensors into a platform suitable for analysis of biological samples.

Microfluidics have become increasingly utilized in biosensor applications.³²⁻³⁵ Many widely available biosensors, including pregnancy tests and blood glucose monitors, use microfluidics for simple, rapid transportation of small sample volumes to a detector. Microfluidic technology provides controlled transport of small volumes of fluid, with incorporation of components such as mixers,³⁶ preconcentration,³⁷ pretreatment,³⁸ and extraction,³⁹ to name a few key components. Biological applications benefit from small sample volume requirements, as it allows more frequent sampling in cases such as blood glucose monitoring, generally less painful sampling methods, and lower cost for required reagents. Additionally, microfluidic devices have been fabricated using a wide range of biocompatible materials, including paper, glass, and polymers such as poly(dimethylsiloxane) (PDMS), cyclic olefin copolymer (COC), and poly(methyl methacrylate) (PMMA). Due to the variety of compatible materials, microfluidic devices can be fabricated with tunable properties to fit the desired application. Material tunability

also provides compatibility with a range of detection techniques, including electrochemistry. Many microfluidic devices have been reported for use with electrochemical detection,^{40, 41} including electrodes incorporated directly into the devices during the fabrication process. Alternatively, microfluidic devices can be interfaced with electrodes post-production, allowing reversible sealing between microfluidic channels and complicated electrode platforms.⁴²⁻⁴⁴ The high degree of tunability in both microfluidics and electrochemical detection provides ideal technology to develop biosensors tunable to individual applications.

Biosensors are widely developed for use in research and commercial settings, and the field is continually expanding to target novel applications and improve existing technology. Further development of this technology will continue to advance understanding of the biomedical field and elucidate effective treatment methods for medical conditions and diseases. Systems such as live tissue can be studied as a model for biological function at an organ scale. Portable, inexpensive biosensors can be employed in point-of-care settings, allowing frequent sampling for monitoring biomarkers with temporal resolution, to elucidate the role of specific biomarkers on a patient's health and contribute to the development of medical treatment plans.

The work described here aims to contribute to the field by presenting systems that interface electrochemical detection with microfluidic devices for biomarker detection platforms. The systems developed range from simple, portable devices designed as tools for fluid transport mechanisms in microfluidic devices, to complex platforms used for imaging biomarkers released from live tissue slices with spatiotemporal resolution. Implementation of these tools for other bioanalytical applications could be readily achieved to further advance the field of electrochemical biomarker detection using microfluidic platforms.

The first tool described utilized degassed poly(dimethylsiloxane) (PDMS) as a portable mechanism for fluid transport in microfluidic devices. There are currently a wide variety of microfluidic platforms available for biosensor detection, but there is a constant need to make the devices more accessible by increasing portability, decreasing cost, and improving ease-of-use.

Sample collection and storage methods can be investigated as a means to improve biomarker detection systems. Porous membranes such as filters provide an advantageous method for sample collection because the collection procedure is generally less expensive and less complicated than other sample collection techniques.^{45, 46} Specifically, venipuncture is a painful, invasive, and expensive blood collection method, requiring a trained phlebotomist to perform. This standard procedure generates samples on the order of several mL. An ideal alternative to venipuncture is blood sampling *via* dried blood spots, where the blood is collected from the patient *via* a finger prick and dried directly onto a filter paper card. This simple technique is minimally invasive, relatively painless, and inexpensive, typically requiring less than 50 μ L of blood to be collected. Dried blood spots are already widely used in neonatal screening due to the low volume requirements,⁴⁷⁻⁴⁹ and could be readily expanded to other diagnostic applications. The use of dried filter samples such as dried blood spots, however, requires sample extraction from the filter matrix prior to analysis.

A degassed PDMS pumping mechanism was developed as an inexpensive, portable method to control fluid transport in a microfluidic device after on-chip extraction from a dried filter sample. On-chip extraction is critical to maintain the simplicity of the microfluidic system by limiting the number of steps a user must perform. The majority of microfluidic devices rely on external equipment such as syringe pumps to generate fluid flow in the device. Syringe pumps, however, can be costly, and their added bulk decreases the portability of the system. Alternatively, passive pumping mechanisms using a variety of techniques have been developed for fluid transport within a microfluidic device, eliminating the need for external pumping equipment. These methods include, but are not limited to, digital microfluidic systems,^{49, 50} flexible valves incorporated directly into the microfluidic device,⁵¹ capillary-driven flow,⁵² and degassed PDMS to generate pressure changes in the microfluidic channel.^{53, 54} The mechanism developed here further employed the gas permeability of PDMS as a method of fluid transport. When placed under vacuum, air within the PDMS diffuses out. Upon return to atmospheric

pressure, the pressure equilibrates by pulling surrounding air back into the PDMS. This includes air from within the microfluidic channel, resulting in a pressure drop in the channel, drawing fluid from the sample reservoir into the device. Previous reports required the entire microfluidic device be placed in a vacuum chamber immediately prior to use, preventing sample preloading on the device and generating immediate fluid transport upon addition to the device, limiting the extraction time of the sample from a filter matrix. The tool developed here consisted of a PDMS pump that was degassed separately from the microfluidic device, allowing on-chip extraction from dried filter samples prior to solution transport down. The degassed PDMS pump was then sealed into the microfluidic device, generating a pressure drop upon diffusion of air from the microfluidic channel into the PDMS pump, resulting in solution flow to an electrochemical detection region in the device. Separate PDMS pumps, such as the system described here, could be incorporated into other microfluidic platforms as a simple, portable fluid transport mechanism.

The other system described in this work was developed as an electrochemical imaging platform to image chemical gradients occurring at the surface of live tissue slices. Chemical gradients have been shown to drive a wide variety of biological processes, including cellular movement and communication.¹⁻³ Understanding how chemical gradients relate to corresponding biological phenomena is critical for elucidating disease progression, such as Alzheimer's development and cancer metastasis,^{55, 56} therefore it is essential to develop platforms capable of imaging chemical gradients with spatiotemporal resolution. A commonly used method for imaging biological systems is fluorescence microscopy, which achieves spatiotemporal resolution while maintaining a high level of sensitivity and selectivity.⁵⁻⁷ Fluorescence microscopy, however, has a target library limited to species that are inherently fluorescent or modified with fluorescent probes. The ability to expand this library to a wider range of biomarkers *via* electrochemical methods would enhance understanding of the role of chemical gradients in biological systems.

Electrochemical detection using an electrode array provides a complementary imaging platform capable of detecting biomarkers inaccessible to traditional optical methods and can provide quantitative information with spatiotemporal resolution. Images generated by electrode arrays are presented in the form of “heat maps,” where individual electrodes in the array act as “pixels” in the image, with a color intensity representing signal, and therefore biomarker concentration, at that electrode. Previously reported electrode arrays have consisted of up to 81,920 electrodes⁵⁷ to detect action potential across neuronal networks.⁵⁸⁻⁶⁰ These arrays achieve high spatiotemporal resolution, but lack chemical selectivity. Alternative arrays have achieved chemical selectivity using amperometric or voltammetric techniques at the scale of a single cell or cell-to-cell junction,^{14, 61, 62} but there is a need to develop systems capable of electrochemical imaging at the scale of an *ex vivo* murine tissue slice.

The electrode array described in this work was designed as a complementary imaging technique to optical methods to further expand the library of accessible biomarkers. The array consisted of 8,192 individually addressable Pt working electrodes in a 2 mm × 2 mm area. An *ex vivo* murine adrenal tissue slice was directly interfaced with the electrode array. Custom microfluidic devices were developed to provide precise fluid delivery to the tissue slice. The entire setup was designed to interface with an upright microscope for simultaneous optical and electrochemical imaging of chemical gradients released from live tissue slices upon chemical stimulation. Electrochemical imaging of stimulated biomarker release from live tissue slices was achieved with high spatiotemporal resolution. Implementation of this system as an imaging platform could elucidate the role of chemical gradients in biological systems for a wide range of studies.

REFERENCES

1. V. Sourjik and N. S. Wingreen, *Current opinion in cell biology*, 2012, **24**, 262-268.
2. S. H. Zigmond, *The Journal of cell biology*, 1977, **75**, 606-616.
3. J. Diao, L. Young, S. Kim, E. A. Fogarty, S. M. Heilman, P. Zhou, M. L. Shuler, M. Wu and M. P. DeLisa, *Lab on a Chip*, 2006, **6**, 381-388.
4. Y. Yi, L. Sanchez, Y. Gao and Y. Yu, *Analyst*, 2016.
5. K. T. Schomacker, J. K. Frisoli, C. C. Compton, T. J. Flotte, J. M. Richter, N. S. Nishioka and T. F. Deutsch, *Lasers in Surgery and Medicine*, 1992, **12**, 63-78.
6. Y. Amoh, K. Katsuoka and R. M. Hoffman, *Current Pharmaceutical Design*, 2008, **14**, 3810-3819.
7. H. Y. Peng, H. Tang and J. H. Jiang, *Science China-Chemistry*, 2016, **59**, 783-793.
8. D. M. Cate, W. Dungchai, J. C. Cunningham, J. Volckens and C. S. Henry, *Lab on a Chip*, 2013, **13**, 2397-2404.
9. Y. M. Guo, Y. Zhang, H. W. Shao, Z. Wang, X. F. Wang and X. Y. Jiang, *Analytical Chemistry*, 2014, **86**, 8530-8534.
10. X. K. Li, J. N. Wang, L. L. Sun and Z. X. Wang, *Chemical Communications*, 2010, **46**, 988-990.
11. L. Su, W. Jia, C. Hou and Y. Lei, *Biosensors and Bioelectronics*, 2011, **26**, 1788-1799.
12. S. R. I. Gabran, M. T. Salam, J. Dian, Y. El-Hayek, J. L. P. Velazquez, R. Genov, P. L. Carlen, M. M. A. Salama and R. R. Mansour, *Ieee Transactions on Neural Systems and Rehabilitation Engineering*, 2014, **22**, 1072-1082.
13. I. A. Ges, R. L. Brindley, K. P. M. Currie and F. J. Baudenbacher, *Lab on a Chip*, 2013, **13**, 4663-4673.
14. A. Kara, A. Reitz, J. Mathault, S. Mehoul-Loko, M. A. Amirdehi, A. Miled and J. Greener, *Lab on a Chip*, 2016, **16**, 1081-1087.
15. S. Cosnier, *Biosensors and Bioelectronics*, 1999, **14**, 443-456.
16. S. A. Wring and J. P. Hart, *Analyst*, 1992, **117**, 1215-1229.
17. H. Moller and P. C. Pistorius, *Journal of Electroanalytical Chemistry*, 2004, **570**, 243-255.
18. F. C. Moraes, I. Cesarino, D. Coelho, V. A. Pedrosa and S. A. S. Machado, *Electroanalysis*, 2012, **24**, 1115-1120.
19. L. Burke and P. Nugent, *Gold bulletin*, 1998, **31**, 39-50.

20. Y. Sameenoi, M. M. Mensack, K. Boonsong, R. Ewing, W. Dungchai, O. Chailapakul, D. M. Cropek and C. S. Henry, *Analyst*, 2011, **136**, 3177-3184.
21. Z. Taleat, A. Khoshroo and M. Mazloum-Ardakani, *Microchimica Acta*, 2014, **181**, 865-891.
22. I. Švancara, K. Vytřas, K. Kalcher, A. Walcarius and J. Wang, *Electroanalysis*, 2009, **21**, 7-28.
23. B. Habibi, M. Jahanbakhshi and M. H. Pournaghi-Azar, *Electrochimica Acta*, 2011, **56**, 2888-2894.
24. N. Li, J. Wang and M. Li, *Reviews in Analytical Chemistry*, 2003, **22**, 19-34.
25. A. Kraft, *Int. J. Electrochem. Sci*, 2007, **2**, 355-385.
26. S. Tsukada, H. Nakashima and K. Torimitsu, *PloS one*, 2012, **7**, e33689.
27. R. N. Goyal, V. K. Gupta, A. Sangal and N. Bachheti, *Electroanalysis*, 2005, **17**, 2217-2223.
28. J. Premkumar and S. B. Khoo, *Journal of Electroanalytical Chemistry*, 2005, **576**, 105-112.
29. J. Ho Shim, H. Do and Y. Lee, *Electroanalysis*, 2010, **22**, 359-366.
30. N. F. Atta, M. F. El-Kady and A. Galal, *Analytical biochemistry*, 2010, **400**, 78-88.
31. M. Ansari, S. Kazemi, M. A. Khalilzadeh, H. Karimi-Maleh and M. B. P. Zalousi, *International Journal of Electrochemical Science*, 2013, **8**, 1938-1948.
32. S. Kim, H. J. Kim and N. L. Jeon, *Integrative Biology*, 2010, **2**, 584-603.
33. J. Wu and M. Gu, *Journal of Biomedical Optics*, 2011, **16**, 12.
34. A. K. Yetisen, M. S. Akram and C. R. Lowe, *Lab on a Chip*, 2013, **13**, 2210-2251.
35. D. M. Cate, J. A. Adkins, J. Mettakoonpitak and C. S. Henry, *Analytical Chemistry*, 2015, **87**, 19-41.
36. Y. K. Suh and S. Kang, *Micromachines*, 2010, **1**, 82-111.
37. B. C. Giordano, D. S. Burgi, S. J. Hart and A. Terray, *Analytica chimica acta*, 2012, **718**, 11-24.
38. K. F. Lei, *Journal of laboratory automation*, 2012, **17**, 330-347.
39. Y. S. Huh, S. J. Jeon, E. Z. Lee, H. S. Park and W. H. Hong, *Korean Journal of Chemical Engineering*, 2011, **28**, 633-642.
40. F. Sassa, K. Morimoto, W. Satoh and H. Suzuki, *Electrophoresis*, 2008, **29**, 1787-1800.
41. D. G. Rackus, M. H. Shamsi and A. R. Wheeler, *Chemical Society Reviews*, 2015, **44**, 5320-5340.

42. H. Lee, Y. Liu, D. Ham and R. M. Westervelt, *Lab on a Chip*, 2007, **7**, 331-337.
43. E. Ghafar-Zadeh, M. Sawan and D. Therriault, *Analog Integrated Circuits and Signal Processing*, 2009, **59**, 1-12.
44. D. Welch and J. B. Christen, *Journal of Micromechanics and Microengineering*, 2013, **23**, 035009.
45. A. Sharma, S. Jaiswal, M. Shukla and J. Lal, *Drug Testing and Analysis*, 2014, **6**, 399-414.
46. N. Spooner, R. Lad and M. Barfield, *Analytical Chemistry*, 2009, **81**, 1557-1563.
47. R. Guthrie and A. Susi, *Pediatrics*, 1963, **32**, 338-&.
48. T. W. McDade, S. Williams and J. J. Snodgrass, *Demography*, 2007, **44**, 899-925.
49. M. J. Jebrail, H. Yang, J. M. Mudrik, N. M. Lafrenière, C. McRoberts, O. Y. Al-Dirbashi, L. Fisher, P. Chakraborty and A. R. Wheeler, *Lab on a Chip*, 2011, **11**, 3218-3224.
50. S. C. Shih, H. Yang, M. J. Jebrail, R. Fobel, N. McIntosh, O. Y. Al-Dirbashi, P. Chakraborty and A. R. Wheeler, *Analytical chemistry*, 2012, **84**, 3731-3738.
51. N. L. Jeon, D. T. Chiu, C. J. Wargo, H. K. Wu, I. S. Choi, J. R. Anderson and G. M. Whitesides, *Biomedical Microdevices*, 2002, **4**, 117-121.
52. L. Gervais and E. Delamarche, *Lab on a Chip*, 2009, **9**, 3330-3337.
53. I. K. Dimov, L. Basabe-Desmonts, J. L. Garcia-Cordero, B. M. Ross, A. J. Ricco and L. P. Lee, *Lab on a Chip*, 2011, **11**, 845-850.
54. N. J. Cira, J. Y. Ho, M. E. Dueck and D. B. Weibel, *Lab on a Chip*, 2012, **12**, 1052-1059.
55. S. D. Nathanson, *Cancer*, 2003, **98**, 413-423.
56. K. Hensley, M. L. Mairdt, Z. Yu, H. Sang, W. R. Markesbery and R. A. Floyd, *The Journal of neuroscience*, 1998, **18**, 8126-8132.
57. L. J. Johnson, E. Cohen, D. Ilg, R. Klein, P. Skeath and D. A. Scribner, *Journal of Neuroscience Methods*, 2012, **205**, 223-232.
58. E. Ferrea, A. Maccione, L. Medrihan, T. Nieuw, D. Ghezzi, P. Baldelli, F. Benfenati and L. Berdondini, *Frontiers in Neural Circuits*, 2012, **6**, 14.
59. D. J. Bakkum, U. Frey, M. Radivojevic, T. L. Russell, J. Muller, M. Fiscella, H. Takahashi and A. Hierlemann, *Nature Communications*, 2013, **4**, 12.
60. L. Berdondini, P. D. van der Wal, O. Guenat, N. F. de Rooij, M. Koudelka-Hep, P. Seitz, R. Kaufmann, P. Metzler, N. Blanc and S. Rohr, *Biosensors & Bioelectronics*, 2005, **21**, 167-174.
61. B. N. Kim, A. D. Herbst, S. J. Kim, B. A. Minch and M. Lindau, *Biosensors & Bioelectronics*, 2013, **41**, 736-744.

62. J. Rothe, O. Frey, A. Stettler, Y. H. Chen and A. Hierlemann, *Analytical Chemistry*, 2014, **86**, 6425-6432.

CHAPTER 2. DEVELOPMENT OF A PASSIVE PUMPING SYSTEM FOR MICROFLUIDIC DEVICES USING DEGASSED PDMS

Microfluidic platforms primarily aim to address the need for low-cost analysis for point-of-care applications. Many microfluidic systems, however, rely on bulky external equipment such as syringe pumps to accomplish fluid transport in the microfluidic device, increasing the cost of the system and limiting portability. Alternatively, the gas permeability of poly(dimethylsiloxane) (PDMS) offers a convenient, inexpensive, portable fluid transport mechanism in microfluidic devices. Degassed PDMS, when sealed into a microfluidic device, generates a pressure drop in the channel as a result of air diffusion into the PDMS, causing solution to be drawn down the channel. Existing reports require the entire PDMS microfluidic device to be degassed prior to solution transport, limiting the utility of the pumping mechanism as control over flow timing is limited. The work reported here details the development of a separate degassed PDMS pump to use as a tool for fluid transport in a microfluidic channel after controlled extraction from a dried filter sample. The PDMS pump allowed sample introduction into the microfluidic device prior to the degassing step, and provided precise control over activation of fluid flow. Iterative device development resulted in a microfluidic device composed primarily of poly(methyl methacrylate) (PMMA), with the channel geometry defined by laser-cut pressure sensitive adhesive. The PDMS pump contained a hollow core to reliably generate flow down the length of the microfluidic channel after degassing and sealing into the microfluidic device. Incorporation of microwire electrodes in the channel did not significantly affect flow, allowing the PDMS pumping mechanism to be used for fluid transport for electrochemical detection in a microfluidic device. This work is unpublished and was used as a precedent to develop the system reported in Chapter 3. The majority of the device designs, experimental work, and data analysis reported in this chapter were performed by Rachel Feeny. Undergraduate researcher Nicole Puissant contributed to experimental work and design development.

Introduction

Microfluidic devices have been extensively developed to provide low-cost, point-of-care diagnostic platforms for a wide range of applications.¹⁻⁴ There is, however, the continued need to develop tools that can be applied to microfluidic platforms to provide additional improvements to portability, simplicity of use, and cost. A specific area that can be addressed lies in the fluid transport mechanism used to analyze samples in a microfluidic context. Standard microfluidic devices utilize external pumping mechanisms, such as syringe pumps, to control fluid transport. Commercial syringe pumps, however, can be costly and bulky, significantly decreasing the portability and ease-of-use of the system.

Additional fluid transport mechanisms have been developed to eliminate the need for external pumping systems to operate microfluidic devices. Paper-based microfluidic devices circumvent the need for a separate fluid transport component by utilizing the capillary network of paper fibers inherent to the devices themselves.^{5, 6} Traditional polymer devices, however, require an additional mechanism to provide fluid transport. Flexible membranes incorporated directly into the microfluidic channel have served as valves that, when arranged in series, acted as micropumps to drive solution down the channel.⁷ These valves, however, required external application of pressure for activation, such as use of syringe pumps, limiting portability. Alternatively, flexible microvalves in microfluidic devices have been activated to generate fluid flow by finger-actuation.⁸ While generation of fluid movement in a microfluidic device using this method is simple, device fabrication is complex, requiring precise positioning of multiple polymer layers. Other passive-pumping mechanisms reported have included fluid evaporation from microfluidic reservoirs,⁹ capillary driven flow,¹⁰ and using the surface energy of drops of liquids positioned at the ends of microchannels,^{11, 12} to list a few. Capillary networks have also been developed to generate complicated capillary microfluidic networks.^{13, 14} Alternatively, digital microfluidic devices, such as those developed in the Wheeler lab,^{15, 16} offer a platform for automated control of fluid movement without the requirement of external pumping equipment.

This system has been employed for controlled extraction and analysis of dried blood spots with a high level of automation. Many of the reported passive-pumping mechanisms, however, are significantly influenced by environmental conditions such as temperature, pressure, and humidity, affecting control over fluid transport.

Degassed poly(dimethylsiloxane) (PDMS) devices have also been used to accomplish fluid transport in a microfluidic channel.^{17, 18} To generate flow using this mechanism, a microfluidic device composed of PDMS is placed a low pressure environment, such as a vacuum chamber. Alternatively, to maintain portability, the device could be sealed in a vacuum pouch prior to use. Due to the gas permeability of PDMS, air within the bulk polymer diffuses out while under vacuum. Upon removal from the vacuum chamber and return to atmospheric pressure, an aqueous sample is added to a reservoir at one end of a microfluidic channel. The opposite end of the channel is either a dead end within the PDMS or is covered with a gas-impermeable layer. Air is pulled from within the microfluidic channel into the bulk PDMS to equilibrate the pressure, resulting in a pressure drop in the microfluidic channel, in turn drawing solution from the sample reservoir into the microfluidic channel. This technique has previously been reported for generating flow of aqueous samples in microfluidic devices for bioanalytical applications. Dimov, *et al.* used a degassed PDMS microfluidic device for transport of whole blood samples for analysis,¹⁷ and Cira, *et al.* transported aqueous samples into dead end channels using degassed PDMS for antibiotics studies.¹⁸ The primary limitation of such previously reported methods is that activation of the flow mechanism requires the entire microfluidic device to be placed in the vacuum chamber, limiting when solutions can be added to the device, preventing control over the time of flow initiation, and minimizing device reusability.

To further advance the utility of degassed PDMS as a fluid transport mechanism in microfluidic devices, a system should be developed in which a “PDMS pump” separate from the bulk device is individually degassed and can be applied to the device to activate flow with

precise timing. Degassing the pumping mechanism separate from the microfluidic device allows sample loading and pretreatment within the device without immediate flow into the channel as a result of the degassed PDMS. Parameters such as flow rate and total flow volume could also be controlled by tuning the volume, geometry, and other specifications of the PDMS pump. Such a pump would provide precise control over fluid movement in a microfluidic channel without the need for external equipment.

This work aims to add to the tools available for incorporation into microfluidic platforms to provide fluid transport using a simple, low-cost, and portable method. An iterative design process resulted in development of a microfluidic device and degassed PDMS pump to allow precise timing of fluid transport down the microfluidic channel after sample extraction from a dried filter spot for electrochemical analysis. The system described here reproducibly generated solution transport using a simple, user-friendly, portable, and inexpensive degassed PDMS pump.

Materials and Methods

All chemicals used in this work were used as received without further purification. Sylgard 184 poly(dimethylsiloxane) (PDMS) oligomer and cross-linker were purchased from Dow Corning (Midland, MI, US). Poly(methyl methacrylate) (PMMA) was purchased from Fort Collins Plastics (Fort Collins, CO, US). Pressure sensitive adhesive (PSA) was obtained from 3M (467MP, 60 μm , Maplewood, MN, US). Food dye (Great Value, Bentonville, AR, US) was used for improved visualization of the solution in the microfluidic channels. Phosphate buffer (0.05 M, pH 6.8) used to extract samples from dried filter spots was prepared from KH_2PO_4 and Na_2HPO_4 , both purchased from Sigma-Aldrich (St. Louis, MO, US).

PDMS Microfluidic Device Fabrication

PDMS microfluidic devices were fabricated using well-established photolithography and stereolithography methods,^{19,20} as diagramed in Figure 2.1. A silicon wafer (Silicon, Inc., Boise, ID, US) was coated with SU-8 3050 (MicroChem, Westborough, MA, US) using a spin coater (WS-650MZ-23NPP/LITE, Laurell Technologies Corporation, North Wales, PA, US) to achieve a final feature height of 50 μm , as measured using a ZeScope optical profilometer (Zygo, Middlefield, CT, US). UV exposure with a UV lamp (OmniCure Series 2000, Lumen Dynamics, Mississauga, Ontario, Canada) was performed using a custom photomask (CAD/Art Services, Inc., Bandon, OR, US) to generate a mold for a rectangular channel. A degassed 10:1 mixture of PDMS oligomer to cross-linker was poured onto the mold, cured at 80 °C for >60 min, and subsequently removed from the mold. A second PDMS layer was generated by pouring PDMS onto a pristine wafer and curing as described above. A biopsy punch (Robbins Instruments, Inc., Chatham, NJ, US) was used to create 6-mm-diameter inlet and outlet reservoirs in the second PDMS layer. The two layers of PDMS were placed in a plasma cleaner and oxidized for 20 s before being immediately brought into conformal contact to form an irreversible seal. The microfluidic devices were left at room temperature for a minimum of 48 h to ensure hydrophobic recovery of the PDMS surface prior to use.

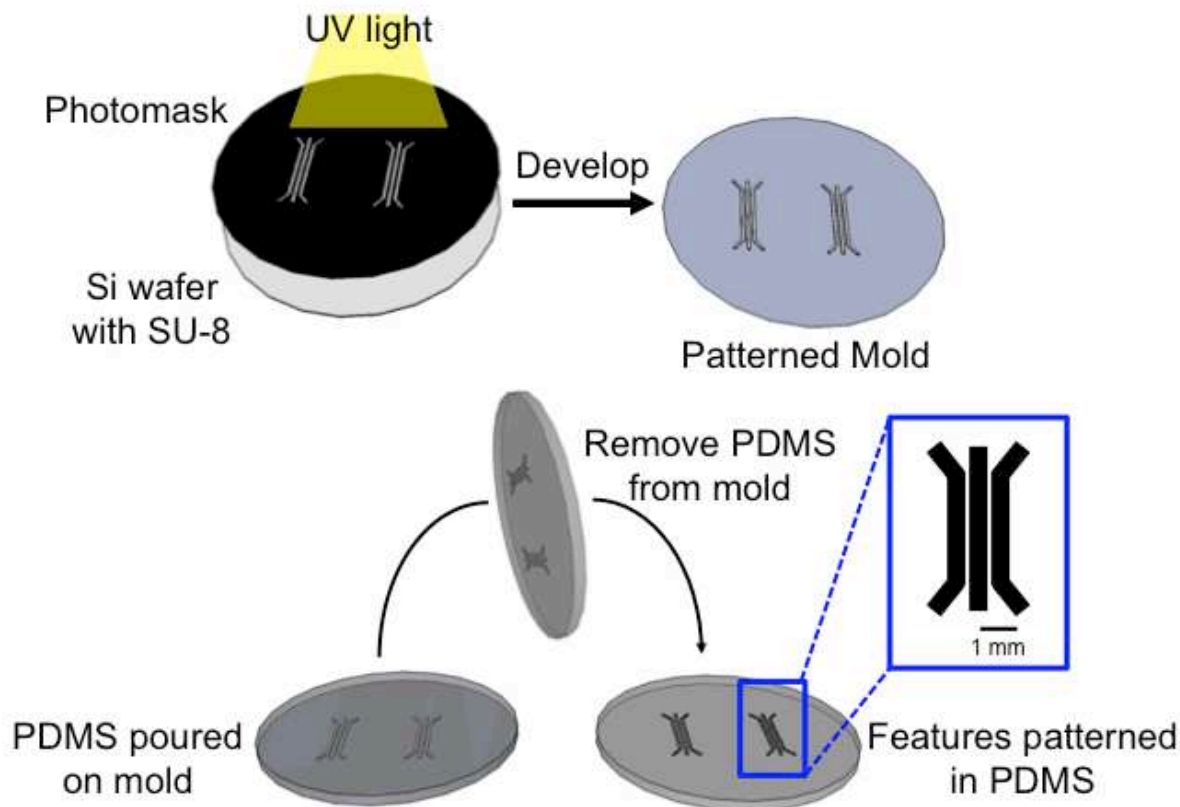


Figure 2.1: General schematic of the photolithography and soft lithography processes. A silicon wafer coated with SU-8 photoresist was exposed to UV light through a photomask to crosslink the photoresist. After developing away remaining photoresist, a patterned mold with raised features remained. PDMS was poured on the surface of the mold and cured. Removal of the PDMS from the mold generated recessed features patterned into the PDMS.

Carbon Paste Electrode Fabrication and Modification

The ultimate aim of this work was to incorporate a passive pumping system into a microfluidic device for electrochemical biomarker detection. Therefore, initial experimentation utilized enzyme-modified electrodes in a microfluidic channel for amperometric glucose detection. To generate these electrodes, photolithography and stereolithography methods described above were used to pattern 500- μm -wide electrode channels into PDMS. A binder was prepared by mixing equal parts of 10:1 PDMS and mineral oil. Two electrode channels (auxiliary and pseudo-reference) were filled with a carbon paste consisting of equal parts binder and graphite. The remaining working electrode channel was filled with a carbon paste consisting

of equal parts binder and a carbon mixture containing 1:1 graphite:carbon nanotubes. The electrodes were baked at 95 °C for 30 min and 120 °C for 60 min to crosslink the binder, followed by plasma treatment (5 min, 1 torr, 150 W). The working electrode was then modified with glucose oxidase for selective glucose detection. A solution containing 4 mg mL⁻¹ glucose oxidase and 50 mM 1-ethyl-3-(3-dimethylaminopropyl)carbodiimide in phosphate buffer was placed on the working electrode for enzyme attachment at room temperature for 2 h, followed by thorough rinsing with buffer. Further experimentation used simplified microfluidic devices consisting of channels without incorporated electrodes to focus solely on generating fluid flow in a reproducible manner using degassed PDMS.

PMMA Microfluidic Device Fabrication

Microfluidic channels were fabricated in PMMA devices using a variety of methods. The first method investigated was laser engraving. A laser engraving system (30 W Epilog, Golden, CO, US) was used to etch a channel into a piece of PMMA and cut reservoirs at either end. Prior to thermal bonding, a hydrophobic layer was incorporated into some PMMA microfluidic devices for increased fluid control. The layer consisted of PMMA microparticles, which were fabricated by coating pristine PMMA with a mixture of PMMA and polystyrene, followed by removal of polystyrene using tetrahydrofuran (THF).²¹ The PMMA channel was then thermally bonded to either the microparticle-modified PMMA layer or a pristine piece of PMMA to generate an enclosed device. Thermal bonding was accomplished in an oven (45 min at 110 °C, 10 min temperature ramps heating and cooling, then 30 min at room temperature to cool) using binder clips and aluminum plates, which were found to apply adequate pressure to bond the devices (Figure 2.2).

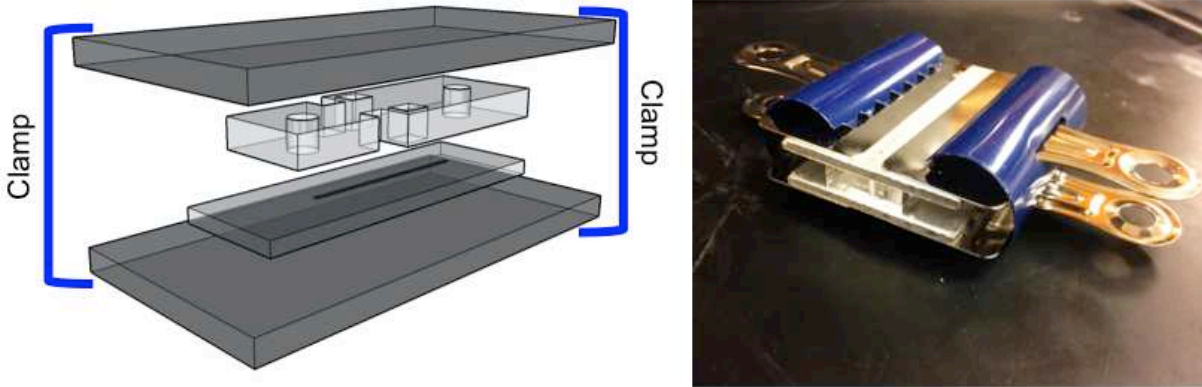


Figure 2.2: Schematic and photograph of method used to apply pressure to PMMA devices to thermally bond layers together. Binder clips provided sufficient, consistent pressure to the PMMA to seal two layers together without causing warping during bonding.

An alternative method for fabricating microfluidic channels in PMMA devices was to define the channel geometry in a thin layer (60 μm) of double-sided pressure-sensitive adhesive (PSA) and use it to seal two layers of PMMA together to generate the floor and ceiling of the channel. A laser engraving system was used to cut the channels into the adhesive and reservoirs into the PMMA. The layers were aligned manually, then bonded together using a press (room temperature, 15 s, 1500 lb). When electrodes were incorporated into the PMMA devices, two layers of 60- μm -thick adhesive were used, one each above and below the platinum wires, to maintain constant electrode area by preventing contact between the wires and the PMMA within the channel. One layer of adhesive was attached to each layer of PMMA. Platinum microwires (30 μm , California Fine Wire Co., Grover Beach, CA, US) were placed perpendicularly across the microfluidic channel on one side of the device, the other side of the device was placed on top, and all layers were sealed together using the press, as described above.

PDMS Pumping Mechanism Design and Fabrication

Multiple methods were investigated to use a degassed PDMS pumping mechanism to activate flow in a microfluidic channel. The first consisted of a PDMS cylinder cut to the same

diameter as the pumping well of the device (6 mm) using a biopsy punch. Three small vent holes were punched into the cylinder using a 1-mm-diameter biopsy punch to prevent applying positive pressure to the microfluidic channel when inserting the degassed pump into the device. After the degassed PDMS cylinder was applied to the device, a small piece of scotch tape was placed over the vent holes to close the system. Alternatively, a 5-mm-diameter PDMS cylinder generated using a biopsy punch was placed into the device, and the reservoir was covered with a piece of scotch tape. This second method avoided application of pressure to the microfluidic device during insertion of the PDMS cylinder and provided a consistent unoccupied volume within the well for each experiment.

A PDMS pump was also designed to eliminate the need for scotch tape, simplifying flow activation. To generate these PDMS pumps, a 5-mm-diameter PDMS cylinder was plasma bonded to a thin (2 mm) PDMS backing. Using a cylinder of smaller diameter than the well in the microfluidic device prevented induction of a positive pressure in the microfluidic channel upon insertion of the pump into the reservoir.

To generate a greater pressure drop in the microfluidic channel and provide greater pumping power, the PDMS pump was modified to include a hollow core in the PDMS cylinder. Two methods were developed for fabrication of the hollow-core PDMS pumps. The first utilized three separate PDMS layers (square backing, hollow core, and solid cylinder) plasma sealed together to generate a single pump. To improve fabrication simplicity, and prevent PDMS warping caused by creating PDMS cylinders with biopsy punches, which generated non-uniform walls on the PDMS pumps, a mold was developed using laser-cut PMMA. The mold consisted of a 3-mm-diameter, 3.175-mm-thick PMMA cylinder centered in a 5.5-mm-diameter, 6.35-mm-thick PMMA well on a piece of tape. Curing PDMS in the mold resulted in vertical, uniform walls for the PDMS pump. Additionally, the back of the PDMS pump was replaced with a 18 mm × 18 mm glass coverslip, preventing diffusion of air from the exterior of the device to contribute to equilibration of pressure within the PDMS pump.

Design and Fabrication of 3D Printed Manifold

An extrusion 3D printer (A-101, Lulzbot, Loveland, CO, US) was used to generate manifolds to simplify device operation and improve experimental reproducibility. The first manifold consisted of an applicator to seal the pump into the device. The applicator was a cube with a depressed center to apply pressure to the edges of the PDMS pump to seal to the device to accomplish flow while avoiding pressing on the center of the pump.

A more sophisticated manifold was designed and 3D printed to provide constant device alignment and consistent pressure when sealing the degassed PDMS pump into the device. The bottom layer of the manifold held the microfluidic device and housed a neodymium rare earth magnet (0.5 in diameter, 0.125 in thick, Applied Magnets, Plano, TX, US). The second layer of the manifold snapped into place on the bottom layer and fit over the top of the pumping well of the microfluidic device, holding the device securely in place and providing consistent alignment for the PDMS pump. After being degassed, the PDMS pump was aligned with the device using the manifold, and placed in the pumping well of the device without applying pressure to create a seal between the two. Finally, the new 3D printed pump applicator was gently placed directly on top of the PDMS pump. The applicator had an open cylinder that applied pressure to the back of the PDMS pump directly at the edge of the pumping well. The back of the applicator housed a second neodymium magnet, which, upon magnetic attraction to the magnet at the bottom of the manifold, provided uniform, constant pressure to seal the PDMS pump into the device.

Flow Rate Experimental Protocol

Throughout the work described here, a general procedure was followed to activate the degassed PDMS pumping mechanism in the microfluidic devices to generate flow. The PDMS pump was first placed into a vacuum chamber (Welch Vacuum, Niles, IL, US) under 500 mmHg vacuum below atmospheric pressure for 10 min. During this time, a dried filter spot, 6-mm-

diameter filter removed from a Whatman 903 sample collection card (GE Healthcare, Pittsburgh, PA, US), was placed in the sample well of the device, and 25 μL of phosphate buffer (0.05 M, pH 6.8) was added for extraction from the filter. After the PDMS pump had degassed for 10 min, it was removed from the vacuum chamber and immediately reversibly sealed into the pumping well on the microfluidic device. Diffusion of air from within the microfluidic channel and pumping well into the degassed PDMS pump resulted in a pressure drop in the microfluidic channel, drawing solution out of the sample well and down the channel. After initiating flow, either amperometric signals were measured as solution passed over electrodes in the microfluidic channel, or flow rate was determined by measuring the time it took for solution to travel a known length of the microfluidic channel. The goal in this work was to develop a pumping mechanism using degassed PDMS to transport sample down a microfluidic channel after controlled extraction from a dried filter spot to make electrochemical measurements at a consistent flow rate.

Results and Discussion

The goal of this work was to develop a passive mechanism for fluid transport in a microfluidic device that allows for on-chip sample extraction from a dried filter spot. The mechanism developed employs degassed poly(dimethylsiloxane) (PDMS) in a pumping chamber on the device to generate a vacuum in the microfluidic channel and drive fluid flow. Previous reports, including Dimov, *et al.*,¹⁷ have utilized degassed PDMS in dead end channels to transport blood from sample zones in the device to detection regions in the device. The system, while an effective method for fluid transport in the application described, is not easily translatable to many other microfluidic platforms. For example, sample pretreatment or extraction could not be performed due to the degassing step. To improve the utility of degassed PDMS as a fluid transport mechanism, on-chip sample treatment steps, such as extraction, should be made accessible by eliminating the need to degas the entire microfluidic device. To

demonstrate the need for increased utility of the degassed PDMS pumping mechanism, a simplified single-channel analog of the reported devices was generated, consisting of a single microfluidic channel connecting a sample well to a pumping well (Figure 2.3A). Carbon paste electrodes modified with glucose oxidase were incorporated into the device to demonstrate electrochemical analyte detection in the passive pumping system. Amperometric detection of glucose from dried filter samples resulted in highly variable signal (40% relative standard deviation, RSD), and statistically indistinguishable signals for 50 mM and 100 mM glucose (Figure 2.3B). Signal variability was likely a result of inconsistent sample extraction from the filter, caused by uncontrolled extraction times in the degassed PDMS device. By altering the design of the degassed PDMS pumping mechanism, the utility of the system could be expanded to analysis of dried sample spots by controlling extraction time prior to fluid transport.

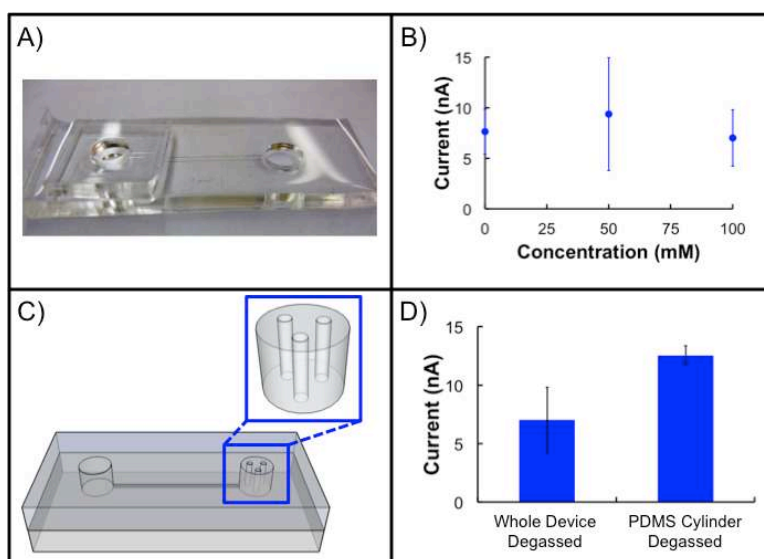


Figure 2.3: **A)** Photograph of original PDMS microfluidic device for fluid transport using degassed PDMS for the pumping mechanism. **B)** Data collected from dried glucose filter samples with fluid transport accomplished by degassing the entire device. Due to limited control of extraction time, all signals were statistically the same. **C)** 3D schematic of a PDMS cylinder in a microfluidic device. The inset blue box shows the separate PDMS cylinder that is degassed during sample extraction in the device for controlled timing of fluid flow activation. **D)** Signal comparison for 100 mM glucose filter samples acquired by degassing the whole device or the PDMS cylinder for extraction time control. Using the PDMS cylinder to control the extraction time increased the signal and reproducibility.

Control of the on-chip sample extraction time from filters was accomplished through the iterative design of a separate degassed PDMS pumping mechanism. This allowed sample extraction to occur in the sample well of the microfluidic device while the PDMS was degassing separately, providing precise control of the time of flow activation while avoiding additional sample handling and transfer steps that would be required to perform off-chip extraction. The PDMS cylinder of the same diameter as the pumping well of the device containing vent holes was degassed separately to generate flow after controlled extraction from dried glucose samples (Figure 2.3C). Using this method, the amperometric signal from 100 mM glucose was increased from 7.02 ± 2.8 nA (40% RSD) without controlled extraction time to 12.5 ± 0.8 nA (7% RSD) with 5 min extraction time using the degassed PDMS cylinder, as shown in Figure 2.3D. Control of extraction time resulted in an improvement in reproducibility and an increase in signal due to improved extraction efficiency from the filter.

Further investigation into the PDMS cylinder method elucidated inconsistencies in flow rate generated using degassed PDMS. Insertion of the PDMS cylinder into the device frequently resulted in manual initiation of flow due to physical deformation of the elastomeric polymer upon pressing on the device. The flow rate was highly variable, where different flow rates occurred for each experiment, which caused a significant effect on amperometric signal. To avoid applying pressure to the microfluidic device during application of the PDMS cylinder, the cylinder was fabricated to have a smaller diameter than the device well by 1 mm. After degassing, the cylinder was placed at the bottom of the well, and a piece of scotch tape was placed over the top of the device to close the system and allow flow to be induced. This method provided a consistent unoccupied volume within the well for each experiment, which can affect the solution flow rate and the extraction time. Despite these improvements, application of tape to the device continued to frequently result in manual initiation of solution flow, necessitating further system development.

Continued pump development aimed to eliminate the need for scotch tape to simplify flow activation and minimize the frequency of occurrence of manual flow activation. A PDMS pump consisting of a cylinder sealed to a square backing reduced the degassed PDMS pumping mechanism to a single piece, minimizing the number of steps required to activate solution flow (Figure 2.4A). Placing the pump in conformal contact with the device after degassing resulted in fluid flow with a decreased number of occurrences of manual initiation of flow (29% of experiments). Solution flow rate reproducibility improved using this method, where the solution traveled the length of the microfluidic channel in 21.2 ± 7.7 s (36% RSD), as shown in Figure 2.4B. Further development was required to continue improving the success rate of these experiments and the flow rate consistency in the microfluidic channel. The dependence of flow rate on individual PDMS pumps was also considered. When observing the flow rates generated by six individual PDMS pumps, there was no apparent influence on flow rate from each pump. The possibility of dependence of flow rate on individual PDMS pumps was considered throughout the course of remaining experiments. Flow rates generated by each individual pump were monitored, and there was no observed influence of single pumps on the solution flow rate.

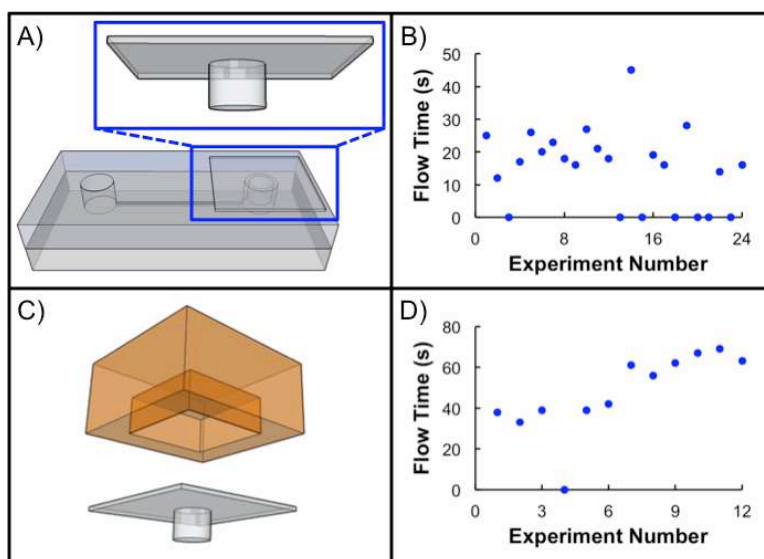


Figure 2.4: **A)** 3D schematic of a PDMS pump in a microfluidic device. The PDMS pump is shown in the inset blue box, and is composed of a PDMS cylinder sealed to a PDMS backing. **B)** Flow data collected using the PDMS pump. Flow times of 0 s indicate failed experiments. **C)** 3D schematic of the 3D printed applicator (orange) used to seal the edges of the PDMS pump to the device during the flow activation step. **D)** Flow data collected using the PDMS pump and 3D printed applicator. Flow times of 0 s indicate failed experiments.

Further improvement of the design to prevent manual initiation of flow employed a 3D printed applicator to seal the pump into the device (Figure 2.4C). The depressed center of the cube provided pressure application to the edges of the PDMS pump to seal to the device to accomplish flow while avoiding pressing on the center of the pump, which would result in manual flow initiation. Results from experiments using the applicator are shown in Figure 2.4D. Using the 3D printed applicator, manual flow initiation decreased to 8% of experiments, but significant variability in flow was observed (51.7 ± 13.5 s, 26% RSD).

Observed variability in flow down the length of the short microfluidic channel led to a design change for the microfluidic device. To employ the system for electrochemical detection as solution traveled down the channel, the flow rate needed to be consistent at a fixed location in the channel, where the electrodes would be incorporated, rather than for the entire length of the microfluidic channel. As a result, a new device was designed to have a longer (22.5 mm) flow channel, and the flow rate was monitored over a 5 mm length near the center of the

channel, representative of the electrochemical detection region. Still frames from a video collected of transport of a dye solution through the channel to determine the flow rate are shown in Figure 2.5. The flow rate was determined using the total time required for the solution to travel the total 5 mm length of the channel. Using the longer channel, 14% of experiments failed, either from manual initiation of flow, or unsuccessful fluid transport down the length of the channel using the PDMS pump. For the successful experiments, however, the variation in flow rate when monitored in the detection region was decreased to 21% RSD.

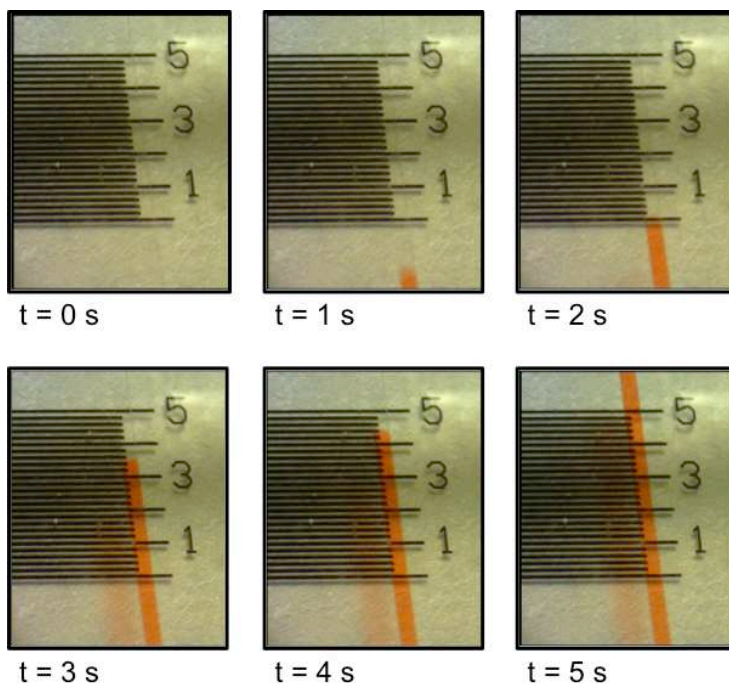


Figure 2.5: Time-lapse images of a dye solution transported down a PDMS microfluidic channel using the degassed PDMS pumping mechanism.

The longer microfluidic channel resulted in a greater internal volume in the microfluidic device, which required the PDMS pump to be modified to have a greater capacity for generating pressure differences in the device to transport fluid down the channel. The PDMS pump was redesigned to include a hollow core in the PDMS cylinder, and fabricated using the methods described above and shown in Figures 2.6A and 2.6B. Air from within the hollow core then diffused through the PDMS walls of the pump during the degassing step. Hollow core pumps

provided a 45% larger volume of available air within the PDMS pump relative to the solid PDMS pumps (68.3 mm^3 vs. 47.2 mm^3),²² allowing a larger pressure difference when sealed into the microfluidic device after being degassed. The completed PDMS pump is pictured in Figure 2.6C. The hollow core PDMS pumps eliminated experiment failure from unsuccessful fluid transport down the length of the channel, though manual initiation of flow still occurred for approximately 5% of experiments, shown in Figure 2.6D.

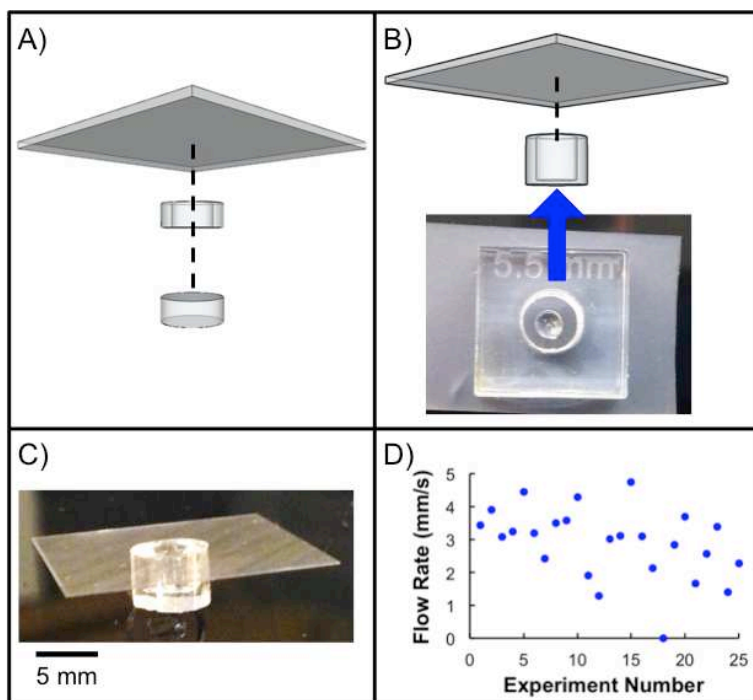


Figure 2.6: **A)** Schematic of 3-layer fabrication method. Each layer is composed of PDMS, and the hollow core is generated by plasma sealing a hollow cylinder between a PDMS backing and a solid cylinder. **B)** Fabrication schematic using a PMMA mold to generate the hollow core in the PDMS. The image at the bottom shows the mold composed of two pieces of PMMA positioned on a piece of tape. **C)** A PDMS pump with a hollow core. **D)** Flow data collected using the hollow core PDMS pump. Flow rates of 0 mm s^{-1} indicate failed experiments.

In effort to completely eliminate manual initiation of flow and provide fluid transport dependent only on the degassed PDMS pump, a 3D printed manifold was designed provide constant device alignment and consistent pressure when sealing the pump into the device. Schematics and photographs of the manifold are shown in Figure 2.7. Use of the manifold to consistently align the pump with the device and magnets to provide constant pressure between

the pump and the device eliminated the occurrence of manual flow initiation, limiting fluid transport to be dependent on the degassed PDMS pump. This system, however, still did not generate consistent flow rates across the detection region of the microfluidic channel, with 21-35% RSD observed.

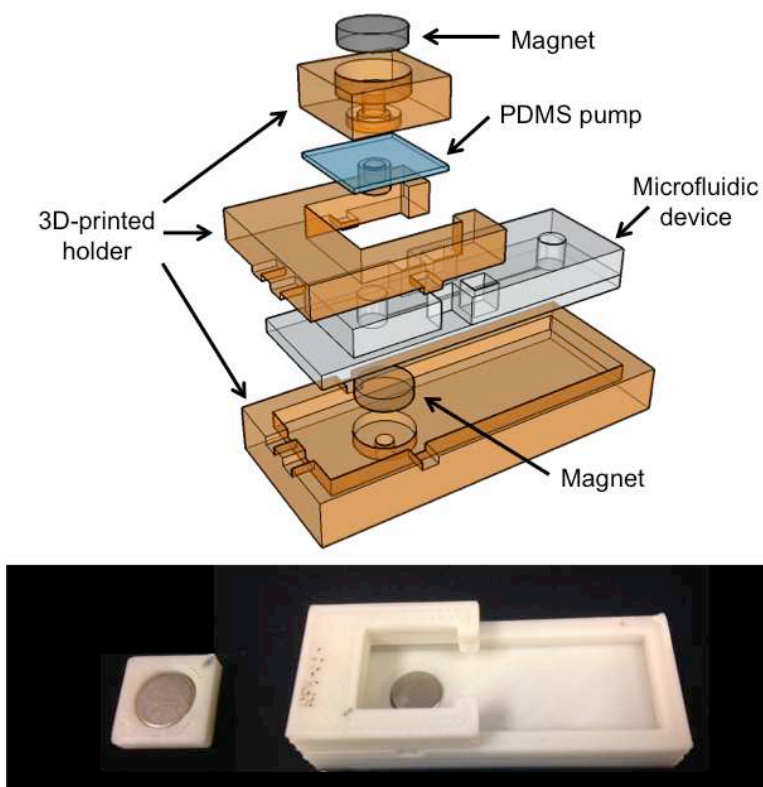


Figure 2.7: Schematic and photograph of 3D printed device holder. Magnets were integrated into the top and bottom pieces of the device holder to apply constant pressure between the PDMS pump and the microfluidic device.

A possible cause for flow rate variability in the microfluidic channel was the gas permeability of the PDMS used to fabricate the device. Diffusion of air within the bulk PDMS into the microfluidic channel during pressure equilibration could vary between experiments and between devices, affecting the flow rates. To address this, PMMA was investigated as an alternative material for device fabrication. Initial flow experiments in PMMA microfluidic devices demonstrated immediate fluid transport down the microfluidic channel upon solution addition to the device. Flow occurred automatically in the PMMA devices but not in the PDMS devices due

to differences in material hydrophobicity. The water contact angle was significantly lower for PMMA than for PDMS ($84.3 \pm 3.0^\circ$ vs. $112.6 \pm 0.9^\circ$, respectively) as measured by contact angle goniometry, shown in Figure 2.8. Use of PMMA for the microfluidic channels therefore required incorporation of an additional feature to limit solution flow until activation by the PDMS pump.

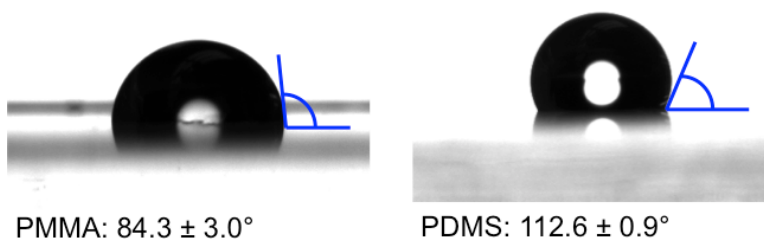


Figure 2.8: Water contact angle measurements on PMMA and PDMS ($n = 9$). The water contact angle was determined by subtracting the indicated angle from 180° . The water droplet size used was $2 \mu\text{L}$.

Incorporation of a hydrophobic layer on the surface of a region of the PMMA device was investigated to prevent solution flow until the PDMS pump is sealed into the device. The layer consisted of PMMA microparticles. The PMMA microparticle layer resulted in a more hydrophobic surface, and prevented automatic solution flow in the microfluidic channel (Figure 2.9A). Solution remained in the sample well until introduction of the degassed PDMS pump, allowing control of extraction time from dried filter samples.

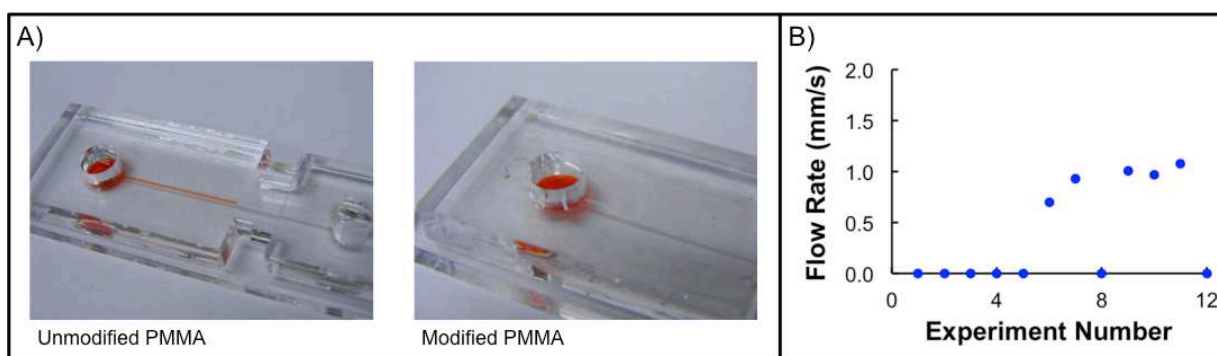


Figure 2.9: **A)** Dyed solution in the sample well of an unmodified PMMA microfluidic device and one modified with a layer of PMMA microparticles. Solution flowed readily down the unmodified PMMA channel, but remained in the sample well of the modified device until flow was activated using a PDMS pump. **B)** Flow data collected using the modified PMMA devices. Flow rates of 0 mm s^{-1} indicate failed experiments.

Flow in the modified PMMA microfluidic devices proved to be highly variable. A high rate of failure (58%) occurred, as shown in Figure 2.9B, where solution flow stopped partway down the channel rather than flowing the entire length. This high level of variability was likely a result of poor uniformity of the modified PMMA layer in the device, combined with the channel roughness caused by fabrication *via* laser engraving. The channel depth was $62 \pm 3 \mu\text{m}$ (5% RSD) as measured by contact profilometry (Dektak XT Stylus Profilometer, Bruker, Billerica, MA, US), and lack of uniformity likely contributed to variability in solution transport. Alternative fabrication methods were therefore investigated for generating microfluidic channels in PMMA devices to create smoother channels and improve flow reproducibility.

Thin layers of adhesive with laser-cut microfluidic channels sealed PMMA layers together to create the device (Figure 2.10A). Using pristine PMMA for the channel resulted in a root mean squared surface roughness of 9 nm as measured by optical profilometry (ZeScope, Zygo, Middlefield, CT, US), providing a smooth, uniform surface for the entire length of the microfluidic channel. When narrow ($< 250 \mu\text{m}$) channels were used in the adhesive, flow did not occur without an external application of pressure to drive the flow (i.e. PDMS pumps), which eliminated the need to incorporate hydrophobic regions on the PMMA to limit flow. Use of the laser cutter to define the geometry also allowed simple incorporation of a bubble cell detection region, where the channel was expanded to 1 mm wide to provide greater working area for the electrodes used for electrochemical detection. Additionally, it was observed that the degassed PDMS pumps consistently transported fluid from the sample well down the length of the microfluidic channel, but the pumping system did not provide enough pressure to break the solution surface tension at the end of the channel to draw it into the pumping well, causing the sample to consistently stop at the end of the microfluidic channel. This phenomenon allowed for electrochemical measurements on a static solution after fluid transport to the electrodes, eliminating the need to generate a constant flow rate in the channel and simplifying the device operation.

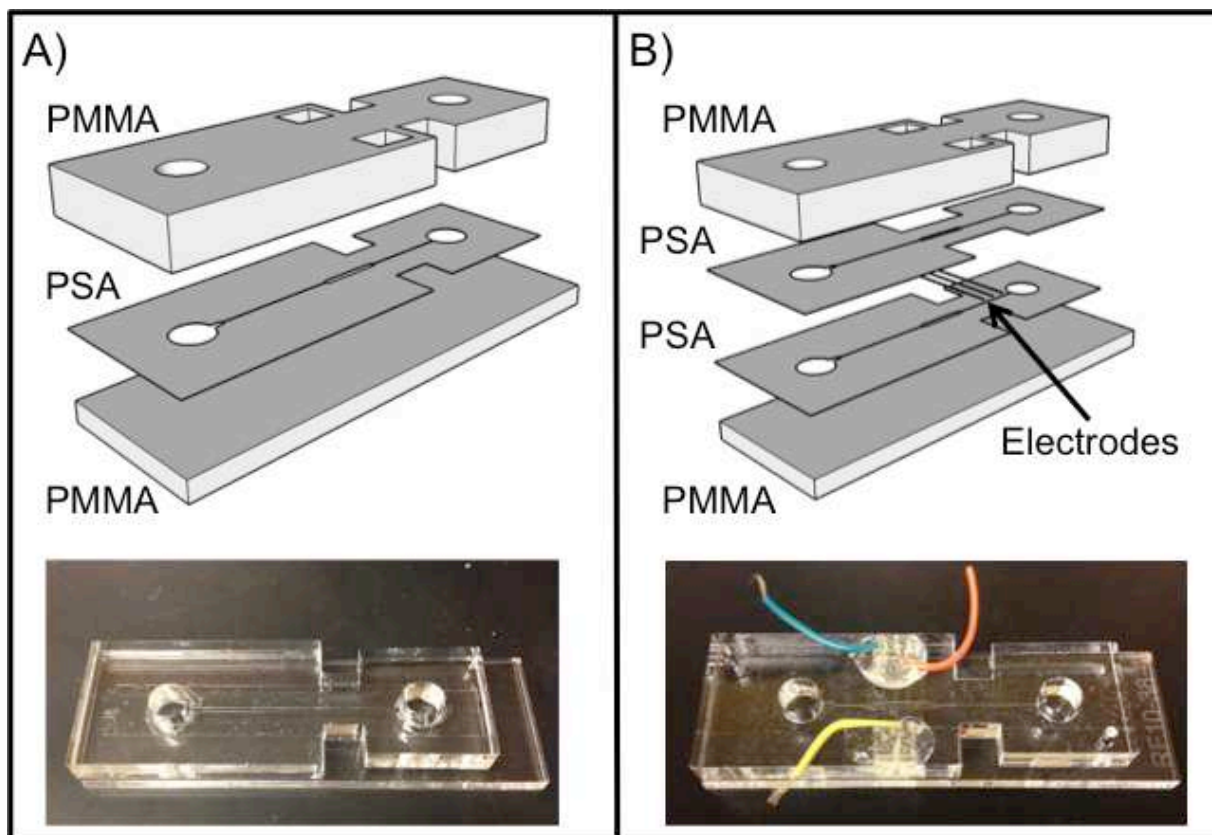


Figure 2.10: A) 3D schematic and photograph of PMMA microfluidic device with the channel defined by a layer of pressure sensitive adhesive (PSA). **B)** 3D schematic and photograph of PMMA microfluidic device with Pt microwire electrodes secured between two layers of PSA.

The final step in developing the degassed PDMS pumping system was to incorporate electrodes into the device to perform electrochemical detection after controlled extraction from a dried filter spot. Use of pressure sensitive adhesive for the channel layer in the device allowed simple, reproducible fabrication of microfluidic devices containing Pt microwire electrodes (Figure 2.10B). Integrating electrodes into the flow channel posed a threat of interfering with the solution flow, but flow experiments demonstrated a high success rate (> 95%) for these devices. Solution flow in the detection region of the device was demonstrated in Figure 2.11.

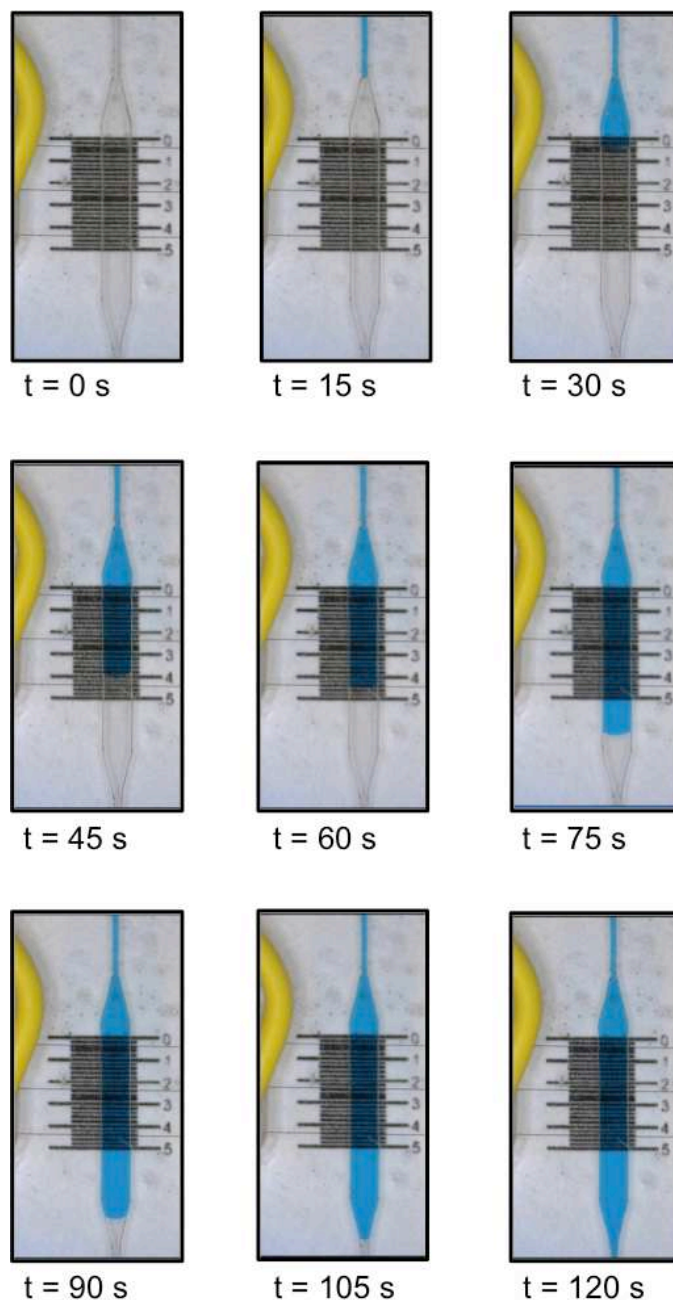


Figure 2.11: Time-lapse images of a dye solution transported down a PMMA/PSA microfluidic channel using the degassed PDMS pumping mechanism. The three horizontal lines near the center of each image were Pt microwire electrodes in the detection region of the channel.

Conclusions

Through iterative device development, a system was developed to achieve fluid transport in a microfluidic device using a degassed PDMS pump. The platform was designed to be user friendly, avoiding accidental manual initiation of flow using a 3D printed manifold, which

also provided reproducible alignment of each component. The small PDMS pump could be conveniently stored in a vacuum-sealed pouch prior to use, eliminating the need for bulky external equipment and improving device portability. After successful development of a microfluidic device and passive pumping system capable of transporting fluid to a detection region after controlled extraction time from a filter sample, the next task is to employ electrochemical detection for biomarker quantification.

A grateful acknowledgement is made to Dr. Morgan Hawker and Dr. Ellen Fisher's laboratory for water contact angle measurements performed in this study.

REFERENCES

1. C. D. Chin, V. Linder and S. K. Sia, *Lab on a Chip*, 2012, **12**, 2118-2134.
2. F. B. Myers and L. P. Lee, *Lab on a Chip*, 2008, **8**, 2015-2031.
3. A. K. Yetisen, M. S. Akram and C. R. Lowe, *Lab on a Chip*, 2013, **13**, 2210-2251.
4. W. Su, X. Gao, L. Jiang and J. Qin, *Journal of Chromatography A*, 2015, **1377**, 13-26.
5. D. M. Cate, J. A. Adkins, J. Mettakoonpitak and C. S. Henry, *Analytical Chemistry*, 2015, **87**, 19-41.
6. Y. Y. Xia, J. Si and Z. Y. Li, *Biosensors & Bioelectronics*, 2016, **77**, 774-789.
7. W. H. Zhang, S. C. Lin, C. M. Wang, J. Hu, C. Li, Z. X. Zhuang, Y. L. Zhou, R. A. Mathies and C. Y. J. Yang, *Lab on a Chip*, 2009, **9**, 3088-3094.
8. K. Xu, M. R. Begley and J. P. Landers, *Lab on a Chip*, 2015, **15**, 867-876.
9. N. S. Lynn and D. S. Dandy, *Lab on a Chip*, 2009, **9**, 3422-3429.
10. L. Gervais and E. Delamarche, *Lab on a Chip*, 2009, **9**, 3330-3337.
11. G. M. Walker and D. J. Beebe, *Lab on a Chip*, 2002, **2**, 131-134.
12. E. Berthier and D. J. Beebe, *Lab on a Chip*, 2007, **7**, 1475-1478.
13. D. Juncker, H. Schmid, U. Drechsler, H. Wolf, M. Wolf, B. Michel, N. de Rooij and E. Delamarche, *Analytical Chemistry*, 2002, **74**, 6139-6144.
14. R. Safavieh, A. Tamayol and D. Juncker, *Microfluidics and Nanofluidics*, 2015, **18**, 357-366.
15. M. J. Jebrail, H. Yang, J. M. Mudrik, N. M. Lafrenière, C. McRoberts, O. Y. Al-Dirbashi, L. Fisher, P. Chakraborty and A. R. Wheeler, *Lab on a Chip*, 2011, **11**, 3218-3224.
16. S. C. Shih, H. Yang, M. J. Jebrail, R. Fobel, N. McIntosh, O. Y. Al-Dirbashi, P. Chakraborty and A. R. Wheeler, *Analytical chemistry*, 2012, **84**, 3731-3738.
17. I. K. Dimov, L. Basabe-Desmonts, J. L. Garcia-Cordero, B. M. Ross, A. J. Ricco and L. P. Lee, *Lab on a Chip*, 2011, **11**, 845-850.
18. N. J. Cira, J. Y. Ho, M. E. Dueck and D. B. Weibel, *Lab on a Chip*, 2012, **12**, 1052-1059.
19. D. C. Duffy, J. C. McDonald, O. J. A. Schueller and G. M. Whitesides, *Analytical Chemistry*, 1998, **70**, 4974-4984.
20. Y. Sameenoi, M. M. Mensack, K. Boonsong, R. Ewing, W. Dungchai, O. Chailapakul, D. M. Cropek and C. S. Henry, *Analyst*, 2011, **136**, 3177-3184.
21. Y. Ma, X. Y. Cao, X. J. Feng, Y. M. Ma and H. Zou, *Polymer*, 2007, **48**, 7455-7460.

22. T. C. Merkel, V. I. Bondar, K. Nagai, B. D. Freeman and I. Pinnau, *Journal of Polymer Science Part B-Polymer Physics*, 2000, **38**, 415-434.

CHAPTER 3. DEGASSED PDMS PUMP FOR CONTROLLED EXTRACTION FROM DRIED FILTER SAMPLES IN MICROFLUIDIC DEVICES

Simplified sample collection methods can continue to advance the field of biosensors by decreasing the cost required to acquire and store samples and/or increasing the number of locations where the sensors can be used. Filter samples have become increasingly popular as low-cost, simple methods to collect samples and are widely used for a variety of applications including dried blood spots in neonatal screening. Dried filter samples, however, limit the available sample volume and require sample extraction for analysis, increasing analysis time and cost. Combining microfluidic devices with low-cost, power-free pumps made from degassed PDMS allows for simple control over extraction time from dried filters prior to fluid transport to internal electrodes for electrochemical biomarker detection while also removing the need for traditional powered pumps. When combined with an electrochemical microfluidic device, extraction for 5 min provided an extraction efficiency of $31.8 \pm 5.6\%$ for dopamine samples dried onto filters. The reported system provides a sensitivity of $9.9 \pm 0.3 \text{ nA mM}^{-1}$ for dopamine as a model analyte in a simple phosphate buffer, which could be further improved by stacking filters for simultaneous extraction and improving extraction efficiency from the filters. Dopamine-spiked control serum provided signal distinguishable from the serum background, demonstrating the capability of the system to measure biomarkers in complex matrices. This work applies the technology developed in Chapter 2 to on-chip extraction of dopamine from dried filter samples for electrochemical dopamine detection. The work reported here has been accepted for publication in *Analytical Methods*.¹ The majority of the device fabrication, experimental design, and data collection and analysis were performed by Rachel Feeny. Nicole Puissant aided with some device design and data collection.

Introduction

With many existing technologies for biomarker detection, there is a constant effort towards lower costs, increased portability and ease-of-use, and improved sensitivity and selectivity. Additional opportunities for improving biomarker detection systems lie in alternative sample collection and storage methods. Filters and other porous membranes offer advantageous platforms for sample collection, as the procedure is often simpler and less expensive to perform.²⁻⁴ In the case of blood samples, venipuncture is an expensive, involved process, requiring a trained phlebotomist to collect tubes of blood (several mL). Additionally, this can be a painful experience for the patient. Blood samples can also be collected onto filter cards *via* a simple finger prick, which is simple, inexpensive, relatively painless, and requires less than 50 μ L of blood. Dried blood spots are used widely for neonatal screening from infants, due to their small sample volume requirements and pain-free collection methods.⁵⁻⁸ Once dried onto filters, samples can be stored for long periods of time with minimal environmental control and are not significantly affected by changes in temperature, provided they are protected from elevated humidity.^{2, 4, 9-11} Sample stability when dried onto filters also simplifies the sample transportation process. Filters can be transported *via* regular mail, while many other sample types require temperature-controlled trucks.² Additionally, sample pretreatment can be accomplished by using chemically modified filters for sample collection.^{12, 13}

Filter samples, however, require biomarker extraction from the filter for analysis. Sample lost to the filter matrix affects the detection limit of the system, but extraction efficiency can be optimized to circumvent this problem.^{10, 14} Solvent selection, surfactant addition, and mixing techniques can be employed to improve extraction efficiency.^{13, 15, 16} The filters limit the sample volume available for analysis, which is advantageous during sample collection, but can be detrimental to achieving adequate detection limits and restricts analysis to techniques compatible with small volume samples.

Microfluidic devices have been extensively developed for biomarker detection,¹⁷ and can be tuned to be compatible with a variety of sample types, including material dried onto filters,^{7, 18} are capable of biomarker detection from small sample volumes, and can accomplish fluid transport using a range of approaches.¹⁹⁻²² The ideal microfluidic system would employ simple, portable, and inexpensive strategies to transport fluid for biomarker detection from samples dried onto filters. The Wheeler lab has developed a digital microfluidic platform for automated dried blood spot analysis without the need for external pumps to control fluid movement.^{7, 23} Digital microfluidic devices provide on-chip extraction from dried blood spots and fluid manipulation without manual intervention. The majority of methods in microfluidics use pressure-driven flow from syringe pumps, which add complexity and cost to the system. Other methods have been developed as passive-pumping mechanisms, including using the surface energy in drops of liquids at the entrance of a microchannel,^{24, 25} flexible valves and pumps incorporated directly into the microfluidic device,²⁶ fluid evaporation from microfluidic reservoirs,²⁷ and capillary-driven flow,²⁸ among others. Many of these systems, however, are dependent on environmental conditions such as temperature, pressure, and humidity, causing a significant effect on fluid transport in the microfluidic devices. Other systems have utilized degassed poly(dimethylsiloxane) (PDMS) to drive fluid flow in microfluidic channels for analysis of aqueous samples. In these systems, the entire microfluidic device was degassed and held under vacuum until use. Dimov *et al.* reported a blood analysis system fabricated from PDMS that is degassed prior to use to draw whole blood samples into microfluidic channels for analysis.²⁹ Similarly, Cira *et al.* used a degassed PDMS device to accomplish transport of aqueous samples into dead-end channels for antibiotics studies.³⁰ Degassed PDMS provides a mechanism to activate fluid flow with precise control over timing with limited dependence on environmental factors, making it ideal for developing a microfluidic platform with an alternative pumping mechanism. Utilizing degassed-PDMS devices is challenging, however, because of

the need for the entire device to be held under vacuum until use and the inability to control initiation of flow at a specific time.

The goal of the system reported here was to provide a controlled extraction time from dried filter samples in a microfluidic device using a simple, controlled passive pumping. Here, poly(methyl methacrylate) (PMMA) microchips were combined with small degassed PDMS pumps that initiated flow on contact with the rest of the system. The PDMS pumps were degassed in a benchtop vacuum chamber, and could be easily stored and then implemented in a portable setting through storage in vacuum-sealed pouches prior to use. The system employs the gas permeability of PDMS to generate a pressure drop in the microfluidic channel upon sealing the degassed PDMS pump in the device resulting in fluid transport to internal electrodes after precise control of extraction time from dried filter samples. To demonstrate general viability of the approach, dried dopamine-spiked serum samples spotted on filters were analyzed in a microfluidic device by combining the pumping system with electrochemical detection. A simple 3D-printed device was used to assemble the system. Control of extraction time allowed for improvements in extraction efficiency.

Materials and Methods

Materials and Sample Preparation

All chemicals were of at least ACS grade and were used as received without further purification. All solutions were prepared using 18.2 M Ω •cm water from a MilliPore Milli-Q system (Billerica, MA, US). Phosphate buffer (0.05 M, pH 6.8) was prepared from KH₂PO₄ and Na₂HPO₄, purchased from Sigma-Aldrich (St. Louis, MO, US). Dopamine hydrochloride was purchased from Alfa Aesar (Ward Hill, MA, US). H₂SO₄ used for cleaning the electrodes was purchased from EMD Chemicals, Inc. (Gibbstown, NJ, US). Level II control serum was purchased from Pointe Scientific, Inc. (Canton, MI, US).

Samples were deposited on Whatman 903 sample collection cards (GE Healthcare, Pittsburgh, PA, US). For all samples used in this study, 25 μL of each solution was pipetted into each sample circle on the Whatman 903 sample collection cards. After the samples dried completely (>24 h) at room temperature ($22\pm 1^\circ\text{C}$), a 6-mm-diameter punch was removed for analysis from a sample spot on the card using a biopsy punch (Robbins Instruments, Inc., Chatham, NJ, US). This method eliminated dependence on sample volume applied to the filter card, as a constant punch size, and therefore a constant sample volume due to saturation of the paper during sample application, was removed for analysis in each experiment.

Microfluidic Design and Fabrication

The microfluidic device used in this work was composed of two outer poly(methyl methacrylate) (PMMA) (Fort Collins Plastics, CO, US) layers enclosing channels in two layers of pressure-sensitive adhesive (PSA) (3M 467MP, 60 μm , Maplewood, MN, US) as shown in Figure 3.1A. All layers were cut using a laser engraving system (30 W Epilog, Golden, CO, US). Laser engraving systems provide a simple, reproducible method to fabricate microfluidic devices.³¹⁻³³ The overall footprint of the device was 25 mm \times 75 mm. The bottom, 3.18-mm-thick PMMA layer acted as the bottom face of the microfluidic channel, while the top, 6.35-mm-thick PMMA layer acted as the top face of the channel and contained 6-mm-diameter reservoirs for sample extraction and flow activation. Two layers of PSA were cut to dictate the geometry of the microfluidic channel. The channel connecting the two reservoirs was 250 μm wide, with the exception of the detection region, which was a 1-mm-wide bubble cell in order to increase the working area of the electrodes for improved sensitivity.³⁴ After each layer was laser cut, the device was assembled to include three parallel Pt microwire electrodes (30 μm , California Fine Wire Co., Grover Beach, CA, US) between the two PSA layers.³⁵ The device layers were sealed together using a hydraulic press (1500 lb, 30 s, room temperature) (Carver 4122, Carver Inc., Wabash, IN, US). Copper wires (NTE Electronics, Inc., Bloomfield, NJ, US) were then attached

to the Pt microwire electrodes using silver paint (SPI Supplies, West Chester, PA, US) and plastic epoxy (Loctite, Rocky Hill, CT, US) to make external connections to the potentiostat.

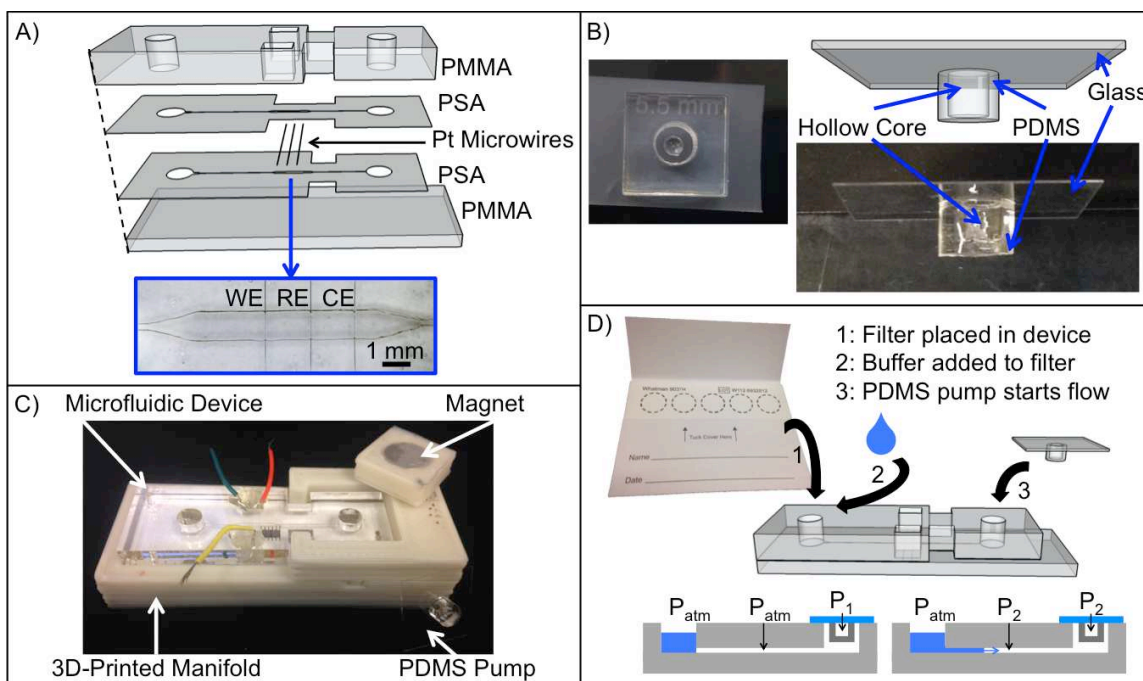


Figure 3.1: **A)** Schematic of the layers used to fabricate the microfluidic devices. The inset blue box shows the detection region containing the Pt microwire working electrode (WE), reference electrode (RE), and counter electrode (CE). **B)** Image of mold for PDMS pump fabrication, and schematic and image of the PDMS pumps. **C)** Photograph of microfluidic device and PDMS pump with custom 3D-printed manifold. **D)** Schematic of procedural steps for device operation. The schematic at the bottom demonstrates how the PDMS pump generates flow.

The PDMS pumps were fabricated using a straightforward process of plasma bonding hollow PDMS cylinders to a glass coverslip. The hollow PDMS cylinders were generated using molds cut from PMMA on the laser engraving system. A hollow pump design was used to maximize pumping efficiency. The mold was prepared by positioning a 3-mm-diameter cylinder of 3.18-mm-thick PMMA in the center of a 5.5-mm-diameter cylindrical hole in 6.35-mm-thick PMMA using a piece of tape (Figure 3.1B). The mold was filled with a degassed 10:1 mixture of PDMS oligomer and cross-linker (Sylgard 184, Dow Corning, Midland, MI, US). After curing, the PDMS was removed from the mold, cut to a height of 3.5 mm, and sealed to the center of a 18 mm × 18 mm glass coverslip (VWR Scientific, Inc., Media, PA, US) using a plasma system

(Harrick Scientific Products, Inc., Pleasantville, NY, US). This generated a PDMS pump with a hollow 3-mm-diameter core. Schematics and images of the PDMS pump fabrication are shown in Figure 3.1B.

The entire device assembly and pump are pictured in Figure 3.1C. A custom PDMS O-ring, 3D-printed manifold (A-101, Lulzbot, Loveland, CO, US), and neodymium rare earth magnets (0.5 in diameter, 0.125 in thick, Applied Magnets, Plano, TX, US) were used to maintain constant pressure between the PDMS pump and the device during operation. Use of the 3D printed manifold and magnets to secure the pump in the microfluidic device improved the simplicity of device operation. The custom PDMS O-ring provided a secure, reversible seal between the PDMS pump and the microfluidic device, preventing leakage during fluid transport. An overall schematic of the device operation from sample extraction to fluid transport *via* the degassed PDMS is shown in Figure 3.1D.

The PDMS pump was placed in a vacuum chamber (Welch Vacuum, Niles, IL, US) under 500 mmHg vacuum below atmospheric pressure for 10 min. Although the PDMS pumps were degassed in a vacuum chamber immediately prior to use here, the pumps could be stored in vacuum-sealed pouches after being degassed to eliminate the need for on-site vacuum chambers. A sample was removed from the Whatman 903 filter card using a 6-mm-diameter biopsy punch and loaded into the sample well of the microfluidic device. Phosphate buffer (25 μ L, unless otherwise indicated) was added to the sample well to extract material from the filter for 5 min (unless otherwise noted). To initiate fluid transport, the PDMS pump was removed from the vacuum chamber and sealed into the pumping well of the microfluidic device using the manifold described above. The schematic at the bottom of Figure 3.1D details how flow was generated using the degassed PDMS pumping mechanism. While in the vacuum chamber, the hollow core in the PDMS pump was evacuated *via* diffusion of air through the PDMS walls. Upon removal of the pump from the vacuum chamber and subsequent sealing into the PMMA device, the external and internal pressure (P_{atm}) of the microfluidic channel were equal. Air

diffused from within the reservoir and channel of the microfluidic device into the lower pressure (P_1) degassed PDMS pump. Diffusion of air from within the enclosed device to the hollow pump core generated a pressure drop in the channel, where the pressure in the channel (P_2) was lower than the external pressure (P_{atm}), resulting in fluid transport from the sample well to the end of the channel. Surface tension prevented the fluid from travelling into the pumping well of the device, allowing electrochemical measurements on static solutions.

The pumping capabilities of the system described here were comparable to those previously reported. Typical flow rates in the bubble cell portion of the microfluidic devices used in this work when using the PDMS pumping mechanism were approximately $1.1 \mu\text{L min}^{-1}$. Existing literature values encompassed a wide range of flow rates generated using degassed PDMS, from slow flow rates ($0.5 - 2 \text{ nL min}^{-1}$)³⁶ to faster rates ($0.8 - 16.7 \mu\text{L min}^{-1}$).²⁹ Flow rate variability in the device reported here was not significant as the goal of this system was to transport fluid down the microfluidic channel after sample extraction to perform electrochemical detection on a stationary solution. Consequently, the total volume of solution pumped into the microfluidic device was the critical parameter in the device design. Pumping solution to the end of the microfluidic channel without entering the pumping well provided a consistent volume of solution transported ($2.1 \mu\text{L}$, the internal channel volume) and ensured electrochemical detection on a stationary solution. Other devices reported provided a range of solution volume pumped using a degassed PDMS pumping mechanism, including filling dead-end channels ($<5 \mu\text{L}$)²⁹ and diffusional mixing in a Y-shaped channel (filling a 90 nL channel with continued flow into the reservoir).³⁶ The degassed PDMS pump in this work was specifically intended to transport fluid down the channel without breaking into the pumping well. The PDMS pumps were used repeatedly ($n>20$) with no observed loss in integrity or pumping capability. Each microfluidic device was used multiple times ($n>5$) with no signal degradation provided the microwire electrodes were cleaned after each use according to the procedure described below. No changes in flow in the microfluidic channel were observed upon repeated use of the devices

as long as the devices were completely dry before being used. The only cause of failed devices observed in this work was occasional transport of filter fibers into the microfluidic channel.

After the microfluidic channel was filled, electrochemical detection by differential pulse voltammetry (DPV, -200 mV to $+500$ mV at 50 mV s⁻¹) was performed using an eDAQ QuadStat and e-corder 821 with eDAQ EChem v2.1.11 software (eDAQ, Denistone East, Australia). Prior to each use of the devices, the Pt electrodes were cleaned in 50 mM H₂SO₄ using cyclic voltammetry (-400 mV to $+1400$ mV at 100 mV s⁻¹, 20 cycles) based on previously reported methods.³⁷ For all data reported, $n \geq 3$ and uncertainties are listed as \pm one standard deviation, collected on different devices from a set of 36.

Results and Discussion

Previously reported systems employing the gas permeability of PDMS as a fluid transport mechanism in microfluidic devices focused on transport and analysis of liquid samples and did not provide control over extraction time.^{29, 30} We first demonstrate the impact of controlling extraction time for dopamine dried on standard blood collection filter membranes. As seen in Figure 3.2, the signal increases with increasing extraction time until reaching a maximum at approximately 5 min. The ability to activate the pumping mechanism after sample and buffer addition provides precise control of sample extraction time from the filters. Dopamine samples (1 mM) were extracted from the filters in 25 μ L of phosphate buffer. Increasing extraction time from immediate transport to the detection region to 5 min extraction prior to fluid transport resulted in a signal increase from 11.5 nA to 15.2 nA, measured at $+0.1$ V.

Estimation of the percentage of the sample-modified filter removed from the card and signal comparison to aqueous standard solutions (data not shown) suggests an extraction efficiency of $31.8 \pm 5.6\%$ at 5 min. After 5 min, the dopamine signal does not significantly increase, indicating that the maximum extraction efficiency is reached in a short period of time.

This trend was observed for $n \geq 3$ replicates. For the remaining studies, all samples were extracted from the filters for 5 min prior to fluid transport *via* the PDMS pumping mechanism.

The extraction efficiency determined in this study is lower than desired for implementation of the system for clinical applications, but is adequate for demonstrating the proof-of-concept device and pumping mechanism. Low extraction efficiency is likely due the simplicity of the extraction step, which only requires addition of buffer to the filter without any mixing, and is dependent on sample diffusion from the filter network into the extraction buffer. Upon further development of the system, additional strategies could be employed to increase the extraction efficiency from the filters. Such strategies include incorporation of surfactants and/or organic solvents during the extraction step and instituting a mixing step within the sample well.

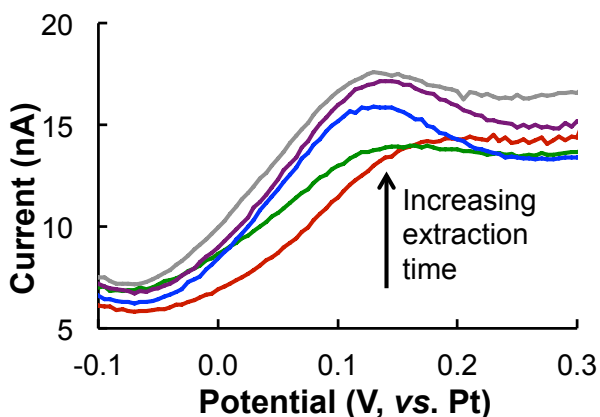


Figure 3.2: Effect of extraction time (— 0, — 2, — 5, — 8, and — 10 min) from 1 mM dopamine filter samples in 25 μ L of phosphate buffer. Increasing extraction time increases the resulting dopamine signal, which plateaus after 5 min. Replicate experiments ($n \geq 3$) supported the observed trend.

Calibration of the system using dopamine solutions (250 μ M – 1 mM) dried onto filter cards demonstrated a linear relationship (sensitivity = 9.89 ± 0.28 nA mM^{-1}) between dopamine concentration and electrochemical signal (Figure 3.3). The control sample consisted of phosphate buffer dried onto a Whatman 903 filter card. The current for each concentration was measured at +0.1 V in order to minimize the background signal. The system showed good

linearity over the range tested ($R^2 = 0.998$), with good reproducibility (4.1 – 16.0% RSD). The highest variability occurred at high dopamine concentrations above clinically relevant levels, while the best reproducibility was observed at low dopamine levels approaching the range expected in biological samples (0.1 – 1 μM dopamine).^{38, 39}

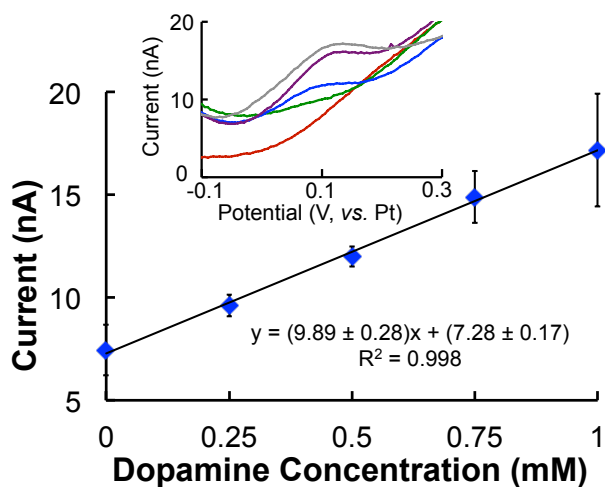


Figure 3.3: Calibration curve of dopamine extracted from dried filter samples for 5 min in 25 μL of phosphate buffer. Current was measured at +0.1 V. Error bars represent the standard deviation for each concentration ($n \geq 3$). **Inset:** Representative voltammograms of each dopamine concentration (— phosphate buffer, — 0.25, — 0.50, — 0.75, and — 1.00 mM dopamine).

In an effort to improve signal and demonstrate sample flexibility, multiple filter samples were stacked in the device for simultaneous extraction. Stacking three 6-mm-diameter samples of 1 mM dopamine filters and extracting with 50 μL of phosphate buffer for 5 min was found to increase the response from 14.2 ± 1.4 nA (one filter) to 17.4 ± 2.5 nA (three filters) (Figure 3.4). This increase in signal is lower than the desired 3 \times improvement. Increasing the number of filters required a larger volume of extraction buffer to successfully transport solution into the channel using the PDMS pump. This increased volume dilutes the sample, slightly decreasing the signal for a single filter. In fact, simultaneous extraction from three filter samples using 50 μL of buffer generated the same response as extraction from a single filter sample using 25 μL of buffer (17.4 ± 2.5 nA vs. 17.2 ± 2.7 nA). The expected signal increase was 1.5 \times , indicating a concomitant decrease in extraction efficiency when analyzing multiple filters. Further

improvement of extraction efficiency from the dried filter samples can provide a greater impact on the system when stacking multiple filters and will be the subject of future studies.

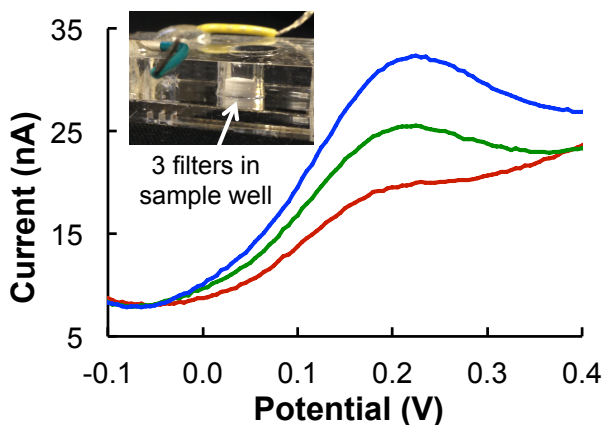


Figure 3.4: Representative voltammograms demonstrating the effect of increasing the number of filter samples (— 1, — 2, and — 3 filters), simultaneously extracted for 5 min in 50 μ L of phosphate buffer. Repetition ($n \geq 3$) showed a reproducible trend. **Inset:** Three filter samples stacked in the microfluidic device.

To demonstrate the utility of this system for biomarker detection in complicated sample matrices, control serum was spiked with known concentrations of dopamine and dried onto Whatman 903 filter cards. The serum samples were analyzed by removing a 6-mm-diameter sample from the filter card and extracting with 25 μ L of phosphate buffer for 5 min, prior to fluid transport *via* the PDMS pump, followed by DPV detection. The current was measured at +0.1 V vs. Pt to minimize background interference from the serum. As shown in Figure 3.5, dopamine provided a distinguishable signal relative to the serum background, with an estimated detection limit of 0.21 ± 0.06 mM ($S/N = 3$). Although this study does not reach clinically relevant dopamine levels, which have been reported in the range of 0.01 – 1 μ M,^{38, 39} the proof-of-concept work described here demonstrates the ability to use degassed PDMS pumps to control on-chip extraction time from dried filter samples prior to electrochemical detection. Further improvements could be implemented in the system to detect biomarker concentrations at clinically relevant levels. These include increasing the working area of the electrode, incorporating surfactants and/or organic solvents to improve extraction efficiency, optimizing the

size of the filter sample, and optimizing the volume of extraction buffer. Additionally, the utility of the PDMS-pumping mechanism could be expanded through implementation in microfluidic devices with other detection motifs, such as optical systems, to accomplish sample extraction and fluid transport.

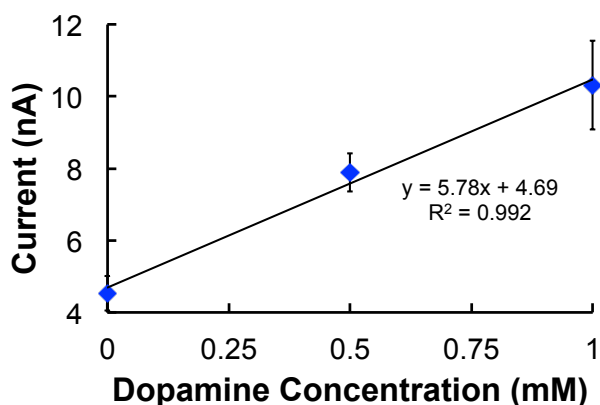


Figure 3.5: Signal from dopamine-spiked serum samples, extracted from dried filters for 5 min in 25 μL of phosphate buffer. Current was measured at +0.1 V. Error bars represent the standard deviation for each concentration ($n \geq 3$).

Conclusions

A proof-of-concept pumping mechanism utilizing the gas permeability of PDMS for fluid transport in a microfluidic channel was demonstrated to achieve controlled extraction time from samples dried onto filters for electrochemical detection of biomarkers. Utilizing the gas permeability of PDMS as a microfluidic pumping mechanism provides control of extraction by dictating the time at which the flow is initiated. The system achieved improved extraction efficiency after 5 min of extraction time, demonstrating improvement over previously reported systems incompatible with controlling extraction from filters. DPV was employed to detect 250 μM – 1 mM dopamine from dried filter samples, and dopamine was quantified in the background matrix of control serum, demonstrating compatibility with complex samples. Further improvements to this system can provide electrochemical detection of a range of biomarkers from biological samples such as dried blood spots after controlled extraction from the filters.

The authors would like to thank Scott Noblitt for his contribution to the design of the PDMS pumping mechanism.

REFERENCES

1. R. M. Feeny, N. L. Puissant and C. S. Henry, *Analytical Methods*, 2016, DOI: 10.1039/c6ay01880g.
2. A. Sharma, S. Jaiswal, M. Shukla and J. Lal, *Drug Testing and Analysis*, 2014, **6**, 399-414.
3. N. Spooner, Y. Ramakrishnan, M. Barfield, O. Dewit and S. Miller, *Bioanalysis*, 2010, **2**, 1515-1522.
4. J. Deglon, A. Thomas, P. Mangin and C. Staub, *Analytical and Bioanalytical Chemistry*, 2012, **402**, 2485-2498.
5. R. Guthrie and A. Susi, *Pediatrics*, 1963, **32**, 338-343.
6. T. W. McDade, S. Williams and J. J. Snodgrass, *Demography*, 2007, **44**, 899-925.
7. M. J. Jebrail, H. Yang, J. M. Mudrik, N. M. Lafreniere, C. McRoberts, O. Y. Al-Dirbashi, L. Fisher, P. Chakraborty and A. R. Wheeler, *Lab on a Chip*, 2011, **11**, 3218-3224.
8. T. Waterboer, B. Dondog, K. M. Michael, A. Michel, M. Schmitt, S. Vaccarella, S. Franceschi, G. Clifford and M. Pawlita, *Cancer epidemiology, biomarkers & prevention : a publication of the American Association for Cancer Research, cosponsored by the American Society of Preventive Oncology*, 2012, **21**, 287-293.
9. M. Wagner, D. Tonoli, E. Varesio and G. Hopfgartner, *Mass Spectrometry Reviews*, 2016, **35**, 361-438.
10. W. K. Li and F. L. S. Tse, *Biomedical Chromatography*, 2010, **24**, 49-65.
11. C. L. Bowen, M. D. Hemberger, J. R. Kehler and C. A. Evans, *Bioanalysis*, 2010, **2**, 1823-1828.
12. G. W. Liu, Q. C. Ji, M. Jemal, A. A. Tymiak and M. E. Arnold, *Analytical Chemistry*, 2011, **83**, 9033-9038.
13. I. Taneja, M. Erukala, K. S. R. Raju, S. P. Singh and M. Wahajuddin, *Bioanalysis*, 2013, **5**, 2171-2186.
14. N. Spooner, R. Lad and M. Barfield, *Analytical chemistry*, 2009, **81**, 1557-1563.
15. A. J. Wilhelm, J. C. G. den Burger, R. Chahbouni and A. Sinjewel, *Journal of Chromatography B-Analytical Technologies in the Biomedical and Life Sciences*, 2009, **877**, 1595-1598.
16. C. W. N. Damen, H. Rosing, J. H. M. Schellens and J. H. Beijnen, *Analytical and Bioanalytical Chemistry*, 2009, **394**, 1171-1182.
17. S. T. Sanjay, G. Fu, M. Dou, F. Xu, R. Liu, H. Qi and X. Li, *Analyst*, 2015, **140**, 7062-7081.

18. M. Dou, S. T. Sanjay, M. Benhabib, F. Xu and X. Li, *Talanta*, 2015, **145**, 43-54.
19. E. K. Sackmann, A. L. Fulton and D. J. Beebe, *Nature*, 2014, **507**, 181-189.
20. C. Zhou, H. Zhang, Z. H. Li and W. Wang, *Lab on a Chip*, 2016, **16**, 1797-1811.
21. J. Puigmarti-Luis, *Chemical Society Reviews*, 2014, **43**, 2253-2271.
22. G. Luka, A. Ahmadi, H. Najjaran, E. Alocilja, M. DeRosa, K. Wolthers, A. Malki, H. Aziz, A. Althani and M. Hoorfar, *Sensors*, 2015, **15**, 30011-30031.
23. S. C. Shih, H. Yang, M. J. Jebrail, R. Fobel, N. McIntosh, O. Y. Al-Dirbashi, P. Chakraborty and A. R. Wheeler, *Analytical chemistry*, 2012, **84**, 3731-3738.
24. G. M. Walker and D. J. Beebe, *Lab on a Chip*, 2002, **2**, 131-134.
25. E. Berthier and D. J. Beebe, *Lab on a Chip*, 2007, **7**, 1475-1478.
26. N. L. Jeon, D. T. Chiu, C. J. Wargo, H. K. Wu, I. S. Choi, J. R. Anderson and G. M. Whitesides, *Biomedical Microdevices*, 2002, **4**, 117-121.
27. N. S. Lynn and D. S. Dandy, *Lab on a Chip*, 2009, **9**, 3422-3429.
28. L. Gervais and E. Delamarche, *Lab on a Chip*, 2009, **9**, 3330-3337.
29. I. K. Dimov, L. Basabe-Desmonts, J. L. Garcia-Cordero, B. M. Ross, A. J. Ricco and L. P. Lee, *Lab on a Chip*, 2011, **11**, 845-850.
30. N. J. Cira, J. Y. Ho, M. E. Dueck and D. B. Weibel, *Lab on a Chip*, 2012, **12**, 1052-1059.
31. I. A. Choudhury and S. Shirley, *Optics and Laser Technology*, 2010, **42**, 503-508.
32. G. S. Fiorini and D. T. Chiu, *Biotechniques*, 2005, **38**, 429-446.
33. D. Patko, Z. Martonfalvi, B. Kovacs, F. Vonderviszt, M. Kellermayer and R. Horvath, *Sensors and Actuators B-Chemical*, 2014, **196**, 352-356.
34. S. D. Noblitt and C. S. Henry, *Analytical Chemistry*, 2008, **80**, 7624-7630.
35. C. D. Garcia and C. S. Henry, *Anal Chem*, 2003, **75**, 4778-4783.
36. K. Hosokawa, K. Sato, N. Ichikawa and M. Maeda, *Lab on a Chip*, 2004, **4**, 181-185.
37. L. M. Fischer, M. Tenje, A. R. Heiskanen, N. Masuda, J. Castillo, A. Bientien, J. Emneus, M. H. Jakobsen and A. Boisen, *Microelectronic Engineering*, 2009, **86**, 1282-1285.
38. J.-M. Zen and P.-J. Chen, *Analytical Chemistry*, 1997, **69**, 5087-5093.
39. A. Özcan and Y. Şahin, *Electroanalysis*, 2009, **21**, 2363-2370.

CHAPTER 4. LABEL-FREE DETECTION OF C-REACTIVE PROTEIN USING AN ELECTROCHEMICAL DNA IMMUNOASSAY

A label-free electrochemical immunoassay that combines DNA-directed immobilization (DDI) with electrochemical impedance spectroscopy (EIS) on microwire sensors is reported for the detection of C-reactive protein (CRP). CRP is an acute-phase protein that is strongly correlated with systemic inflammation. Since inflammation plays a role in pathogenesis of cardiovascular diseases, CRP can be used to predict the likelihood of coronary events. To demonstrate the new chemistry, 25- μm Au electrodes were modified with single strand DNA (ssDNA) and exposed to a solution containing complementary ssDNA conjugated to monoclonal anti-CRP. The charge-transfer resistance of the $[\text{Fe}(\text{CN})_6]^{3-/4-}$ redox couple was used to determine the CRP concentration after binding. A stepwise increase in the charge transfer resistance was observed using EIS for each modification step, ssDNA, ssDNA-anti-CRP hybridization and the final CRP capture. Cyclic voltammetry (CV) was used to verify the EIS results, and showed an increase in peak potential splitting in a similar stepwise manner for each modification step. Finally, fluorescence microscopy was used to confirm the DNA hybridization and CRP binding. Standard addition of CRP revealed that EIS could be used to detect CRP at clinically relevant levels in serum samples. This new form of electrochemical DNA immunoassay (eDI) has significant potential as a simple, label-free sensor for proteins in microfluidic devices. This work was published in *Sensing and Bio-Sensing Research* in 2016 and was a collaborative effort.¹ Tamsiri Songjaroen performed the majority of the data collection and analysis, and Rachel Feeny helped develop the device fabrication protocol and the experimental setup, and aided in data analysis. Meghan Mensack helped in the device and experimental design.

Introduction

C-reactive protein (CRP) is an acute-phase protein that has been widely associated with medical diagnostics in routine laboratory procedures as a biomarker for a acute infection or inflammation²⁻⁵ with clinical reference intervals of $1 \mu\text{g mL}^{-1}$.⁶ In the case of acute inflammation, however, levels can increase 1000-fold above baseline levels.^{7, 8} Since inflammation plays a role in pathogenesis of cardiovascular disease, CRP can be used to predict the likelihood of coronary events.⁹⁻¹² As a result of its importance, many CRP detection methods have been reported including immunoturbidimetry,^{13, 14} immunoagglutination,^{15, 16} and enzyme-linked immunosorbent assay (ELISA).¹⁷⁻¹⁹ However, these techniques have disadvantages including requiring large (mL) volumes of costly reagents and expensive automated equipment. As a result, most CRP measurements are done in centralized laboratories resulting in significant time delays for patient feedback.

One solution for reducing feedback time is to perform point-of-care measurements using biosensors. Biosensors play an important role in point-of-care diagnosis, utilizing rapid, low-cost, and accurate detection techniques as typified by the handheld glucometer. Many techniques have been developed for CRP detection, including biosensors,^{2, 6, 20-22} point-of-care testing platforms,^{3, 23-26} immunosensors,^{27, 28} and electrochemical detection systems.²⁹⁻³³ Among these techniques, electrochemistry is widely used as a detection motif because of its high accuracy and sensitivity coupled with the low cost and portability of the associated instrumentation.

DNA hybridization-directed antibody immobilization biosensors for highly sensitive and selective detection have been reported.³⁴⁻³⁹ DNA is useful as a capture agent for biosensors because of the sequence specific nature of hybridization coupled with the strong interactions that exist in hybridized DNA. DNA can be modified chemically with functional groups to improve its properties. Moreover, DNA can also be combined with antibodies.^{40, 41} Thus, DNA is widespread for use in biosensor applications.

We report a new electrochemical biosensor for CRP detection as part of a first step in the development of simple, multi-electrode microfluidic clinical diagnostic tools. One of the biggest challenges with multi-analyte electrochemical biosensors is localization of the affinity agents on individual electrodes. One elegant solution to this problem is the use of DNA hybridization to direct localization of antibodies or other affinity agents.⁴² These techniques, referred to as DNA Zipcoding or DNA-Directed Immobilization (DDI) have been widely used with traditional colorimetric or fluorescence detection but not with electrochemical immunoassays. This report detailing the development of an electrochemical DNA immunoassay (eDI), is made possible by selective modification of Au microwires in an electrochemical cell. The use of microwire electrodes for electrochemical detection in conjunction with paper-based analytical devices has been reported recently.⁴³ Au is used because it is easily modified with thiolated DNA.^{44, 45} Once modified, the electrode can be readily blocked to reduce non-specific interactions using mercaptohexanol (MCH).⁴⁵⁻⁴⁷ After modification with the ssDNA, an antibody modified with complementary ssDNA is added, resulting in an electrode modified with the target antibody. Finally, binding is measured using Electrochemical Impedance Spectroscopy (EIS). EIS is a common electrochemical technique capable of quantifying surface binding.^{48, 49} EIS has been used to detect biomolecular events including protein-protein interactions,^{50, 51} DNA hybridization,⁵²⁻⁵⁴ and DNA-RNA⁵⁵ and DNA-protein interactions.⁵⁶⁻⁵⁹

In the current report, a label-free electrochemical biosensor based on DNA-directed immobilization was exploited for CRP detection. A 25- μm -diameter Au wire was utilized to fabricate working electrodes in a 3 mm polymer-based electrochemical cell, using an Ag wire as the common reference electrode. ssDNA was immobilized on the gold microwire electrode surface *via* thiol chemistry with MCH as the blocking agent. The electrode was then modified using a complementary strand of ssDNA conjugated to monoclonal anti-CRP (ssDNA-anti-CRP) *via* hybridization with the ssDNA previously bound to the Au electrode surface. The anti-CRP was able to specifically capture CRP in different samples with signal changes after ssDNA

modification, ssDNA-anti-CRP hybridization, and CRP capture monitored by EIS and cyclic voltammetry (CV). Finally, CRP was quantified in human serum using EIS and showed good correlation with reported levels.

Materials and Methods

Materials and Chemicals

Gold microwire was obtained from California Fine Wire Company (Grover Beach, CA, US). SH-ssDNA probe (5'-/5ThioMC6-D/TTT TTT TTT TCC TGC GTC GTT TAA GGA AGT AC-3') and NH-ssDNA (5'-/5AmMC6/GTA CTT CCT TAA ACG ACG CAG G-3') were synthesized by Integrated DNA Technologies (Coralville, IA, US). C-reactive protein and CRP monoclonal antibody were purchased from Fitzgerald Industries (Acton, MA, US). Ethylenediaminetetraacetic acid (EDTA), 6-mercapto-1-hexanol (MCH), 1-ethyl-3-(dimethylaminopropyl)carbodiimide (EDC), and bovine serum albumin (BSA) were purchased from Sigma Aldrich (St. Louis, MO, US). N-(2-hydroxyethyl)succinimide (NHS) was a product of Pierce (Rockford, IL, US). Tris was manufactured by J.T. Baker (Center Valley, PA, US). Sodium chloride was purchased from Macron Chemicals (St. Louis, MO, US). Fluorescein isothiocyanate (FITC) was a product of Thermo Scientific (Pittsburg, PA, US). Potassium phosphate monobasic (KH₂PO₄) and potassium ferricyanide were products of Fisher Scientific (Pittsburg, PA, US). Potassium ferrocyanide was from Mallinkrodt (St. Louis, MO, US). Poly(dimethylsiloxane) (PDMS) was purchased from Dow Corning (Sylgard 184, Midland, MI, US). All chemicals were used as received.

Electrode Fabrication

The electrochemical cell consisted of three 25- μ m Au microwires, used as working electrodes, and a single 25- μ m Ag wire, used as the reference electrode. Multiple working electrodes were added to allow multiple measurements of the same target analyte in each

experiment for improved statistics. The electrodes were placed on a flat piece of PDMS, and a second piece of PDMS, containing a 3-mm-diameter opening, was sealed over the electrodes using plasma bonding. Braided Cu wires were connected to each microwire using Ag paint and epoxy to provide robust electrical contacts. The Ag wire was used as the common reference electrode against all three working electrodes.

Electrode Modification

The DNA probe length was 32 bases. Previous work reported that varied length of DNA (8 – 48 bases) could be immobilized on solid surfaces *via* the thiol group, although the surface coverage begins to decrease with increasing probe length.⁶⁰ The probe was tethered with a thiol group through a 5' poly(T) tail in order to facilitate the immobilization of the designed DNA probe on the Au microwires. The length of the poly(T) tail allows the probe to freely hybridize with the corresponding 22 base pair complementary strand.

To modify the electrode surface, the Au electrodes were cleaned using previously published methods.^{61, 62} Electrodes were electrochemically polished by potential cycling between – 1.0 V to + 1.0 V at 100 mV s⁻¹ for ten cycles in 50 mM KOH. Next, 50 μ L of 1 μ M SH-ssDNA in KH₂PO₄ (1 M, pH 3.8) was added to the well containing the working electrodes for 1 h at room temperature (22 \pm 2 °C). In this step, the DNA probe was immobilized on the microwire *via* the thiol group. The remaining ssDNA was removed by thorough washing with deionized water. To block the electrode surface, 1 mM MCH was added to the working electrodes and incubated for 1 h at room temperature. Excess MCH was removed by extensive washing with deionized water. After modification, the electrodes were used for subsequent measurements of CRP binding.

ssDNA-anti-CRP Hybridization and CRP Detection on Au Electrodes

Anti-CRP monoclonal antibody was modified with the complementary ssDNA using EDC/NHS bioconjugation according to established methods.⁶³ Briefly, anti-CRP was activated in a solution of EDC/NHS for 15 min (0.1 mg mL⁻¹ of EDC and 0.6 mg mL⁻¹ of NHS in 0.1 M MES, 0.5 M NaCl, pH 6.0). Next, the activated anti-CRP was combined with amine-modified single strand DNA (NH-ssDNA) at a 1:1 ratio and reacted for 2 h at room temperature (22 ± 2 °C). Finally, the solution was filtered using a centrifugal molecular weight cutoff filter (30 kDa cutoff, 14,500 rpm, 5 min) to remove unreacted EDC/NHS/anti-CRP and rinsed three times using phosphate buffered saline (PBS). ssDNA-anti-CRP (1 μM) diluted in TE buffer (10 mM tris-HCl, 1 mM EDTA, 1 M NaCl) was added to the well and allowed to hybridize with SH-ssDNA bound to the Au microwire electrodes for 1 h, resulting in an electrode surface modified with the anti-CRP. The electrode was then rinsed with PBS and deionized water to remove unhybridized DNA. Following this, the electrode surface was submerged in a BSA solution (5% w/v in PBS) for 20 min to minimize nonspecific adsorption, followed by washing with PBS and deionized water. Then a sample containing CRP was incubated on the electrode surface for 10 min to complete the reaction. After rinsing the electrode as described above, EIS spectra were recorded. Figure 4.1 shows a schematic representation of the electrode modification steps and resulting changes in the EIS spectra.

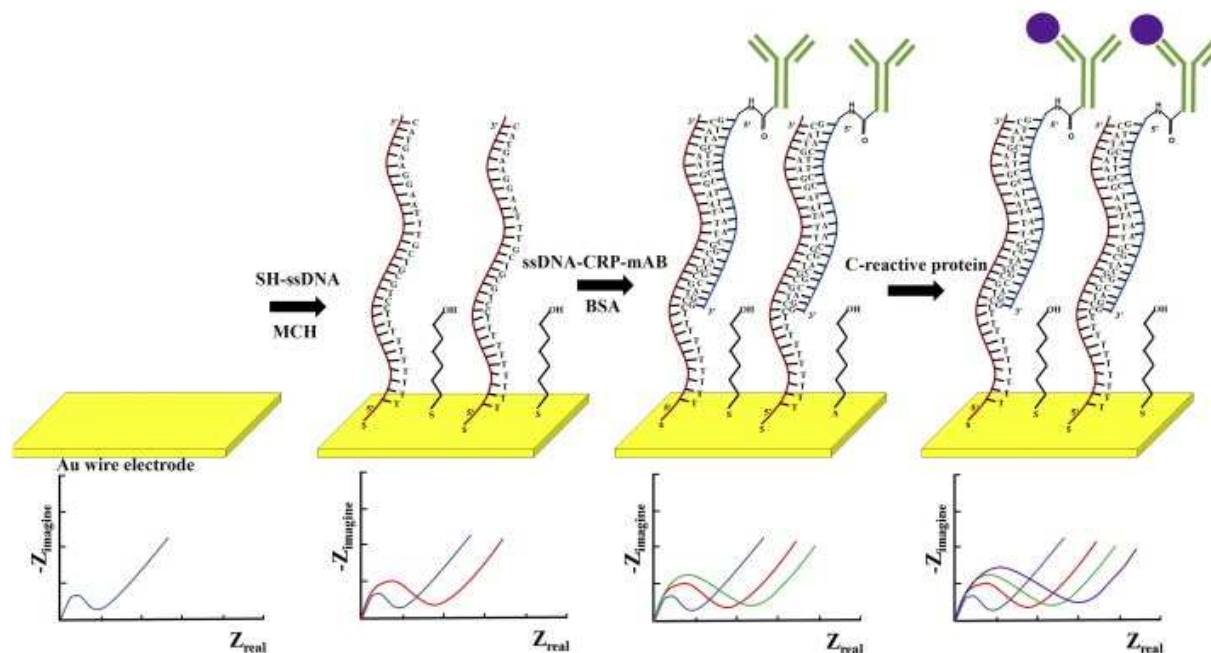


Figure 4.1: Schematic diagram of the electrode modification processes and expected EIS results. From left to right, bare Au electrode, electrode modified with thiolated ssDNA and blocked with MCH, electrode hybridized with ssDNA-anti-CRP, and CRP captured on the Au microwire electrode.

Electrochemical Measurements

All electrochemical experiments were carried out using the Au microwire working electrodes (WE) with a Ag common reference electrode (RE). Electrochemical experiments were performed on a CHI-660 electrochemical workstation (CH Instruments, Austin, TX, US). Cyclic voltammetry (CV) and EIS were carried out in 5 mM $[\text{Fe}(\text{CN})_6]^{3-/4-}$ prepared in PBS (pH7.4, containing 0.1 M KCl). Unless otherwise stated, cyclic voltammetry was performed at 100 mV s^{-1} and cycled from -0.6 V to $+0.8 \text{ V}$. EIS was recorded using 0.1 Hz – 100 kHz frequency range. The amplitude was 0.01 V with the potential set at 0.2 V. Data were plotted in Nyquist plots. For standard CRP detection, commercial human serum spiked with various CRP concentrations were used to generate a calibration curve. CRP in a serum control was measured by EIS using the optimized conditions. For blind sample studies, samples were

prepared in the same way as the CRP standards by a laboratory coworker. The concentration of CRP for each unknown was not reported until the sample was analyzed by EIS.

Results and Discussion

CRP Detection by Cyclic Voltammetry and Electrochemical Impedance Spectroscopy

Changes in the electrode impedance and voltammetry were measured in a stepwise fashion using CV and EIS in 5.0 mM $[\text{Fe}(\text{CN})_6]^{3-/4-}$ (Figure 4.2) to monitor electrode modification. CV shows a significant shift in the peak potential after modification with ssDNA as a result of the combination of electrostatic repulsion between the anionic DNA and redox probes and the barrier created by the adsorbed organic layer. The ΔE_p of the bare electrode was 0.175 V, while the ΔE_p of the ssDNA modified electrode was 0.395 V. Upon electrode modification with ssDNA-anti-CRP and subsequent CRP binding, the ΔE_p shifted further to ΔE_p 0.487 V and ΔE_p 0.561 V, respectively, indicative of the further increase in the thickness of the organic layer (Figure 4.2A). The changes in peak potential clearly indicate successful DNA hybridization and protein capture on the electrode.

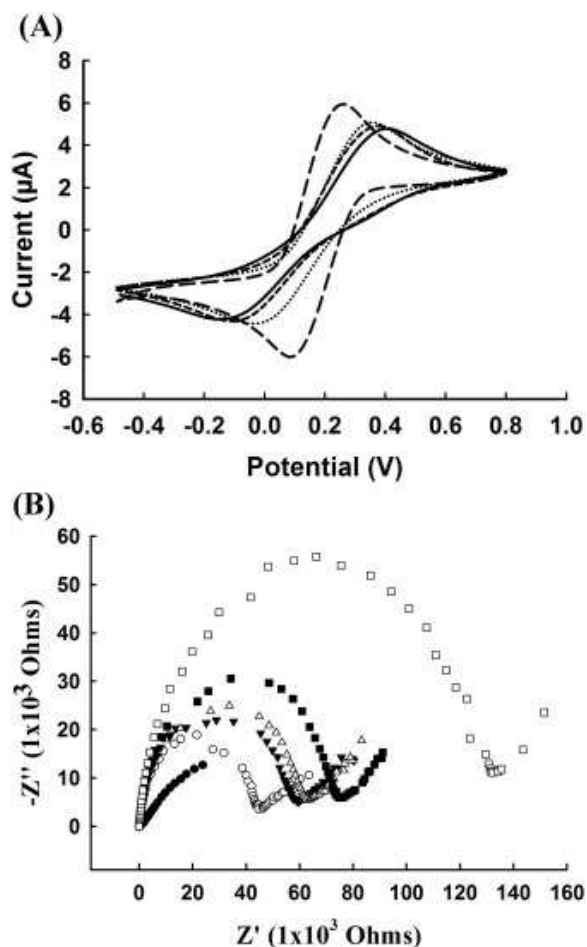


Figure 4.2: Cyclic voltammograms (CV) and electrochemical impedance spectroscopy (EIS) measurements for electrode modifications. **A)** — — bare gold, ssDNA self-assembled monolayer on gold, - - - - - ssDNA-anti-CRP hybridized to the probe, — — — — and CRP capture with anti-CRP. **B)** Nyquist plots for ● bare gold, ○ ssDNA self-assembled monolayer on gold, ▼ ssDNA-anti-CRP hybridized on the electrode, and △ 6.25 mg L⁻¹ CRP, ■ 12.5 mg L⁻¹ CRP, and □ 25 mg L⁻¹ CRP at 0.1 Hz – 100 kHz frequency range, amplitude at 0.01 V with the potential at 0.2 V in 5.0 mM [Fe(CN)₆]^{3-/4-}.

EIS was also used to confirm electrode modification. Each point of the Nyquist plot represents the impedance of one frequency scanned from high to low. The semicircle of the Nyquist plot at low frequency represents the charge transfer resistance (R_{ct}). DNA hybridization or protein capture on the electrode surface causes a change in R_{ct} . From the results in Figure 4.2B, it was observed that the Z' of the self-assembled monolayer (SAM) functionalized electrode (44.67 kΩ) was larger than the Z' of the bare Au electrode (1170 Ω). The impedance increase indicates the successful modification by SH-ssDNA. When the SH-ssDNA modified

electrode was hybridized with the ssDNA-anti-CRP, the R_{ct} value increased further due to increased blocking of the electrode surface to the redox probe (59.54 k Ω). Finally, when CRP was conjugated to the immobilized anti-CRP, an additional increase in the R_{ct} value was observed at 63.27, 75.50, and 132.1 k Ω for 6.25, 12.5, and 25.0 mg L⁻¹ CRP, respectively. The increase in R_{ct} demonstrated binding of CRP to anti-CRP on the surface of the Au electrode.

Fluorescence Assay for ssDNA-anti-CRP Hybridization and CRP Capture on Au Microwire Electrodes

To further verify electrode modification, a simple fluorescence assay was developed. The Au microwire electrode was first modified with SH-ssDNA. Then, FITC labeled ssDNA-anti-CRP was allowed to hybridize with ssDNA on the electrode. Fluorescence was then measured using a fluorescence microscope (100 \times magnification). Figure 4.3A clearly shows fluorescence from the FITC immobilized on the Au electrode indicating successful hybridization. Next, the experiment was repeated using unlabeled ssDNA-anti-CRP and FITC-labeled CRP. Figure 4.3B shows clear fluorescence indicating FITC-CRP binding to the modified electrode. The fluorescence results verify the electrochemical results measured for each modification step and clearly indicate the viability of the method for selective detection.

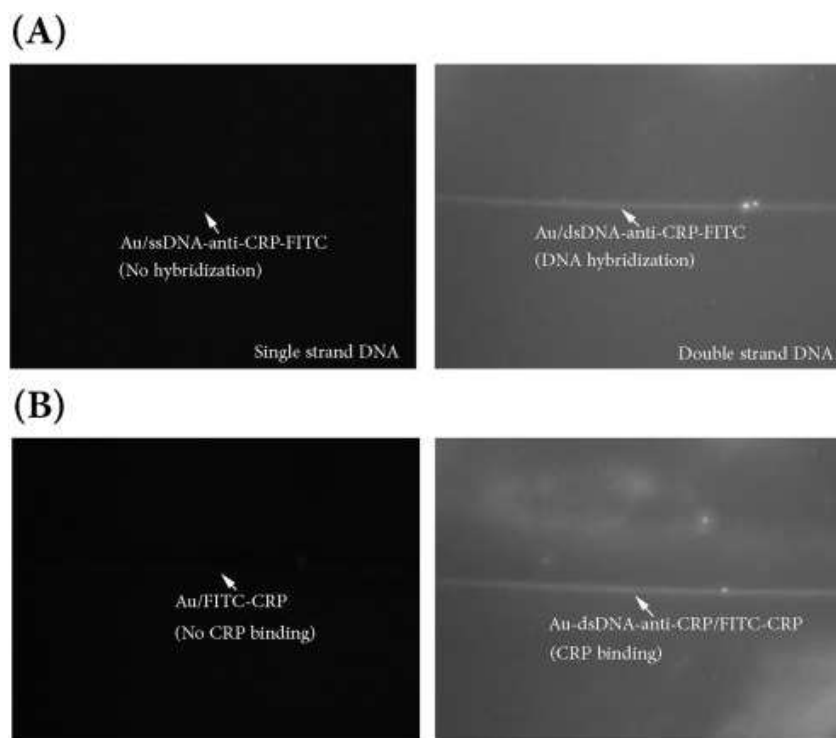


Figure 4.3: **A)** Fluorescence assay of ssDNA-anti-CRP hybridization. Left: Au/ssDNA-anti-CRP-FITC (control). Right: Au/dsDNA-anti-CRP-FITC. **B)** CRP capture on Au microwire electrode. Left: Au/FITC-CRP (control). Right: Au/dsDNA-anti-CRP/FITC-CRP.

Calibration Curve and CRP Detection in Serum Samples

The binding of CRP to anti-CRP was indicated by the change in R_{ct} . After demonstrating the ability of DNA-directed immobilization to localize anti-CRP on an electrode surface, a calibration curve was generated. CRP levels in control serum were analyzed by EIS. After modification, the electrodes were incubated with the serum sample to allow CRP binding to anti-CRP. After thorough rinsing, impedance spectra were obtained in the presence of 5 mM $[\text{Fe}(\text{CN})_6]^{3-/4-}$ in PBS. EIS data were normalized by using the equation following R. K. Gupta:³¹

$$\Delta R_{ct} = \left[\frac{R_{ct} dsDNA - anti - CRP / CRP}{R_{ct} dsDNA - anti - CRP} \right] - 1$$

Figure 4.4 shows a plot of ΔR_{ct} versus CRP concentrations. The measured ΔR_{ct} value increased proportionally to CRP concentration. The response became nonlinear at 50 mg mL⁻¹. The nonlinearity is caused by excess analyte concentration at the electrode surface, resulting in

surface binding site saturation on the microelectrodes. A linear response ($y = 0.0067x + 0.0502$, $R^2 = 0.989$) was observed over the range of 3.125 – 25 mg L⁻¹ for CRP detection by EIS (Figure 4.4 inset). Blind CRP samples were then analyzed using the sensor system with the results shown in Table 4.1. EIS was demonstrated to show good correlation between CRP concentration in serum samples and reported values.

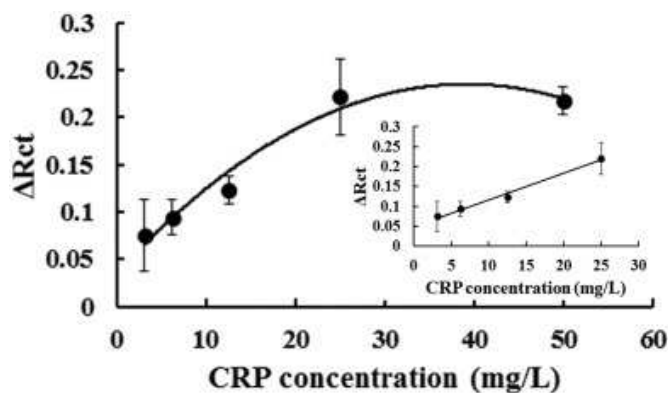


Figure 4.4: Calibration curve for detection of CRP spiked in human control serum on Au mirowire electrodes, 5.0 mM [Fe(CN₆)^{3-/4-}, frequency 0.1 Hz – 100 kHz, amplitude 0.01 V, potential 0.2 V, n = 3, $R^2 = 0.989$). Inset: Linear range of calibration curve.

Table 4.1: CRP detection in serum samples

Sample	Spiked CRP Concentration (mg L ⁻¹)	CRP Concentration by EIS (mg L ⁻¹)
1	5	6.07 ± 0.76
2	10	10.53 ± 1.68
3	20	19.02 ± 3.00

Conclusions

A label-free electrochemical biosensor using DNA-directed immobilization for C-reactive protein detection has been developed. Au microwires were used as working electrodes because of the ease of their incorporation into microfluidic devices. Electrochemical impedance spectroscopy and cyclic voltammetry were used to follow the electrode surface modification processes with each step increasing the faradaic impedance of the system. Finally, the system was used to detect CRP in human control serum samples as an example application. Future

work will focus on developing the biosensor for multiple targets of inflammation and cardiovascular disease in microfluidic devices for rapid, point-of-care screening.

REFERENCES

1. T. Songjaroen, R. M. Feeny, M. M. Mensack, W. Laiwattanapaisal and C. S. Henry, *Sensing and Bio-Sensing Research*, 2016, **8**, 14-19.
2. M. H. F. Meyer, M. Hartmann, H. J. Krause, G. Blankenstein, B. Mueller-Chorus, J. Oster, P. Miethe and M. Keusgen, *Biosensors & Bioelectronics*, 2007, **22**, 973-979.
3. C. H. Kim, J. H. Ahn, J. Y. Kim, J. M. Choi, K. C. Lim, T. J. Park, N. S. Heo, H. G. Lee, J. W. Kim and Y. K. Choi, *Biosensors & Bioelectronics*, 2013, **41**, 322-327.
4. R. J. Delfino, N. Staimer, T. Tjoa, A. Polidori, M. Arhami, D. L. Gillen, M. T. Kleinman, N. D. Vaziri, J. Longhurst, F. Zaldivar and C. Sioutas, *Environmental Health Perspectives*, 2008, **116**, 898-906.
5. M. Wolf, D. Juncker, B. Michel, P. Hunziker and E. Delamarche, *Biosensors & Bioelectronics*, 2004, **19**, 1193-1202.
6. Y. K. Yen, Y. C. Lai, W. T. Hong, Y. Pheanpanitporn, C. S. Chen and L. S. Huang, *Sensors*, 2013, **13**, 9653-9668.
7. S. Black, I. Kushner and D. Samols, *Journal of Biological Chemistry*, 2004, **279**, 48487-48490.
8. C. Gabay and I. Kushner, *New England Journal of Medicine*, 1999, **340**, 448-454.
9. A. May and T. J. Wang, *Expert Review of Molecular Diagnostics*, 2007, **7**, 793-804.
10. V. M. Miller, M. M. Redfield and J. P. McConnell, *Current Vascular Pharmacology*, 2007, **5**, 15-25.
11. J. K. Pai, K. J. Mukamal, K. M. Rexrode and E. B. Rimm, *PLoS One*, 2008, **3**, e1395.
12. J.-J. Li and C.-H. Fang, *Medical hypotheses*, 2004, **62**, 499-506.
13. A. M. Dupuy, S. Badiou, B. Descomps and J. P. Cristol, *Clinical Chemistry and Laboratory Medicine*, 2003, **41**, 948-949.
14. L. Borque, L. Bellod, A. Rus, M. L. Seco and F. Galisteo-Gonzalez, *Clinical Chemistry*, 2000, **46**, 1839-1842.
15. O. Senju, Y. Takagi, R. Uzawa, Y. Iwasaki, T. Suzuki, K. Gomi and T. Ishii, *Journal of Clinical & Laboratory Immunology*, 1986, **19**, 99-103.
16. N. E. Thomas and W. T. Coakley, *Ultrasound in Medicine and Biology*, 1996, **22**, 1277-1284.
17. N. Barka, J. P. Tomasi and S. Stadtsbaeder, *Journal of Immunological Methods*, 1985, **82**, 57-63.
18. T.-L. Wu, I. C. Tsai, P.-Y. Chang, K.-C. Tsao, C.-F. Sun, L. L. Wu and J. T. Wu, *Clinica chimica acta*, 2007, **376**, 72-76.

19. S. Sadir, M. P. Prabhakaran, D. H. Wicaksono and S. Ramakrishna, *Sensors and Actuators B: Chemical*, 2014, **205**, 50-60.
20. H. W. Choi, Y. Sakata, Y. Kurihara, T. Ooya and T. Takeuchi, *Analytica Chimica Acta*, 2012, **728**, 64-68.
21. H. Yuan, B. H. Kang, J. S. Lee, H. M. Jeong, S. H. Yeom, K. J. Kim, D. H. Kwon and S. W. Kang, *Journal of Semiconductor Technology and Science*, 2013, **13**, 1-7.
22. A. Pomowski, C. Baricham, B. E. Rapp, A. Matern and K. Lange, *Ieee Sensors Journal*, 2015, **15**, 4388-4392.
23. X. L. Cheng, X. Pu, P. Jun, X. B. Zhu, D. Zhu and M. Chen, *International Journal of Nanomedicine*, 2014, **9**, 5619-5626.
24. J. S. Ahn, S. Choi, S. H. Jang, H. J. Chang, J. H. Kim, K. B. Nahm, S. W. Oh and E. Y. Choi, *Clinica Chimica Acta*, 2003, **332**, 51-59.
25. Y. B. Gu, Y. L. Yang, J. Zhang, S. X. Ge, Z. H. Tang and X. B. Qiu, *Instrumentation Science & Technology*, 2014, **42**, 635-645.
26. S. H. Yeom, O. G. Kim, B. H. Kang, K. J. Kim, H. Yuan, D. H. Kwon, H. R. Kim and S. W. Kang, *Optics Express*, 2011, **19**, 22882-22891.
27. C. Sapsanis, S. Sivashankar, H. Omran, U. Buttner, K. N. Salama and Ieee, Fort Collins, CO, 2015.
28. C. Kokkinos, M. Prodromidis, A. Economou, P. Petrou and S. Kakabakos, *Analytica Chimica Acta*, 2015, **886**, 29-36.
29. Y.-S. Sohn, S.-K. Lee and S.-Y. Choi, *Sensor Letters*, 2007, **5**, 421-424.
30. T. Bryan, X. L. Luo, P. R. Bueno and J. J. Davis, *Biosensors & Bioelectronics*, 2013, **39**, 94-98.
31. R. K. Gupta, A. Periyakaruppan, M. Meyyappan and J. E. Koehne, *Biosensors & Bioelectronics*, 2014, **59**, 112-119.
32. J. Chatterjee, 2014.
33. Z. Yang, Y. Liu, C. Lei, X. C. Sun and Y. Zhou, *Microchimica Acta*, 2015, **182**, 2411-2417.
34. K. W. Ren, J. Wu, F. Yan and H. X. Ju, *Scientific Reports*, 2014, **4**, 6.
35. K. Chuah, L. M. H. Lai, I. Y. Goon, S. G. Parker, R. Amal and J. J. Gooding, *Chemical Communications*, 2012, **48**, 3503-3505.
36. K. W. Ren, J. Wu, Y. Zhang, F. Yan and H. X. Ju, *Analytical Chemistry*, 2014, **86**, 7494-7499.
37. C. Boozer, J. Ladd, S. F. Chen, Q. Yu, J. Homola and S. Y. Jiang, *Analytical Chemistry*, 2004, **76**, 6967-6972.
38. H. Li, W. Zhang and H. H. Zhou, *Analytical Biochemistry*, 2014, **449**, 26-31.

39. N. S. Ferreira and M. G. F. Sales, *Biosensors & Bioelectronics*, 2014, **53**, 193-199.
40. C. S. M. Ferreira, K. Papamichael, G. Guilbault, T. Schwarzacher, J. Gariépy and S. Missailidis, *Analytical and Bioanalytical Chemistry*, 2008, **390**, 1039-1050.
41. I. Burbulis, K. Yamaguchi, R. H. Yu, O. Resnekov and R. Brent, *Nature Methods*, 2007, **4**, 1011-1013.
42. C. M. Niemeyer, L. Boldt, B. Ceyhan and D. Blohm, *Analytical Biochemistry*, 1999, **268**, 54-63.
43. J. A. Adkins and C. S. Henry, *Analytica Chimica Acta*, 2015, **891**, 247-254.
44. S. D. Keighley, P. Li, P. Estrela and P. Mighorato, *Biosensors & Bioelectronics*, 2008, **23**, 1291-1297.
45. J. N. Murphy, A. K. H. Cheng, H. Z. Yu and D. Bizzotto, *Journal of the American Chemical Society*, 2009, **131**, 4042-4050.
46. T. M. Herne and M. J. Tarlov, *Journal of the American Chemical Society*, 1997, **119**, 8916-8920.
47. F. Lucarelli, G. Marrazza, A. P. F. Turner and M. Mascini, *Biosensors & Bioelectronics*, 2004, **19**, 515-530.
48. X. X. Li, L. H. Shen, D. D. Zhang, H. L. Qi, Q. Gao, F. Ma and C. X. Zhang, *Biosensors & Bioelectronics*, 2008, **23**, 1624-1630.
49. B. Y. Chang and S. M. Park, in *Annual Review of Analytical Chemistry, Vol 3*, eds. E. S. Yeung and R. N. Zare, Annual Reviews, Palo Alto, 2010, vol. 3, pp. 207-229.
50. A. C. Barton, F. Davis and S. P. J. Higson, *Analytical Chemistry*, 2008, **80**, 9411-9416.
51. G. Tsekenis, G. Z. Garifallou, F. Davis, P. A. Millner, T. D. Gibson and S. P. J. Higson, *Analytical Chemistry*, 2008, **80**, 2058-2062.
52. V. Vermeeren, N. Bijnens, S. Wenmackers, M. Daenen, K. Haenen, O. A. Williams, M. Ameloot, A. Vandeven, P. Wagner and L. Michiels, *Langmuir*, 2007, **23**, 13193-13202.
53. J. Weng, J. F. Zhang, H. Li, L. P. Sun, C. H. Lin and Q. Q. Zhang, *Analytical Chemistry*, 2008, **80**, 7075-7083.
54. F. Davis, M. A. Hughes, A. R. Cossins and S. P. J. Higson, *Analytical Chemistry*, 2007, **79**, 1153-1157.
55. E. A. Lusi, M. Passamano, P. Guarascio, A. Scarpa and L. Schiavo, *Analytical Chemistry*, 2009, **81**, 2819-2822.
56. C. F. Pan, M. L. Guo, Z. Nie, X. L. Xiao and S. Z. Yao, *Electroanalysis*, 2009, **21**, 1321-1326.
57. D. K. Xu, D. W. Xu, X. B. Yu, Z. H. Liu, W. He and Z. Q. Ma, *Analytical Chemistry*, 2005, **77**, 5107-5113.
58. R. Y. Lai, K. W. Plaxco and A. J. Heeger, *Analytical chemistry*, 2007, **79**, 229-233.

59. A. Bogomolova, E. Komarova, K. Reber, T. Gerasimov, O. Yavuz, S. Bhatt and M. Aldissi, *Analytical Chemistry*, 2009, **81**, 3944-3949.
60. A. B. Steel, R. L. Levicky, T. M. Herne and M. J. Tarlov, *Biophysical Journal*, 2000, **79**, 975-981.
61. A. R. Heiskanen, C. F. Spegel, N. Kostasheva, T. Ruzgas and J. Emneus, *Langmuir*, 2008, **24**, 9066-9073.
62. L. M. Fischer, M. Tenje, A. R. Heiskanen, N. Masuda, J. Castillo, A. Bentien, J. Emneus, M. H. Jakobsen and A. Boisen, *Microelectronic Engineering*, 2009, **86**, 1282-1285.
63. J. Tominaga, Y. Kemori, Y. Tanaka, T. Maruyama, N. Kamiya and M. Goto, *Chemical Communications*, 2007, 401-403.

CHAPTER 5. ANALYSIS OF NITRIC OXIDE FROM CHEMICAL DONORS USING CMOS PLATINUM MICROELECTRODES

Electrochemical detection of NO generated from chemical donors is reported. Because NO is an important biological messenger, many donor sources and detection methods have been developed. Few reports have characterized NO donors using electrochemistry despite electrochemical techniques being sensitive and selective. Here, a CMOS platinum microelectrode array is interfaced with a microfluidic device for the electrochemical analysis of NO from (Z)-1-[N-(2-aminoethyl)-N-(2-ammonioethyl)amino]diazene-1,2-diolate (DETA/NO). The donor parent amine fouls the electrode, resulting in substantial signal loss, but an electrochemical cleaning method was developed that substantially reduces fouling and allows detection of NO between 90 nM and 1 μ M. This work was published in *Electroanalysis* in 2015, and was a collaborative effort.¹ Rachel Feeny performed the majority of the data collection and analysis, and John Wydallis designed and fabricated the microfluidic devices used in this work and aided in data collection and analysis.

Introduction

Nitric oxide (NO) has a significant impact in biological systems through its role in cellular signaling by promoting vasodilation,² wound healing,^{3,4} and angiogenesis.^{5,6} Additionally, NO is involved in neurotransmission⁷ and has antibacterial properties.⁸ Of particular interest is the role of NO in directing cell migration,^{9,10} proliferation, survival, and differentiation.¹¹ Simultaneously monitoring NO release from tissue while observing the cells could help in the understanding of how NO drives cellular processes. NO detection can be challenging, however, due to its short aqueous lifetime.^{2,7} Samples for laboratory studies are typically generated by bubbling NO gas through water to make a saturated solution, reducing nitrate or nitrite in solution to form NO, or by using a NO-releasing compound.¹² NO-releasing compounds can provide long-term,

constant NO release, allowing samples to be easily prepared and generate steady state NO concentrations. Many NO donors have been synthesized, and decompose through various mechanisms to generate NO. S-nitrosothiols can decompose through a variety of mechanisms, including catalysis by Cu^+ , light, and pH, and NONOates (1-substituted diazen-1-ium-1,2-diolates) decompose to form NO in an acid-catalyzed dissociation.¹²⁻¹⁴ Of these, (Z)-1-[N-(2-aminoethyl)-N-(2-ammonioethyl)amino]diazen-1-ium-1,2-diolate (DETA/NO) offers the advantage of a long half-life in solution (56 hr at 25 °C) relative to other NO-donating compounds.^{13, 15, 16}

NO has been detected using a range of both direct and indirect techniques.^{13, 17, 18} For complex matrices, electrochemistry offers the advantage of direct detection of NO oxidation, allowing NO detection as it is released from biological sources such as cells in tissue slices. Electrochemical detection in biological matrices can be hindered by the presence of multiple electrochemically active species, but selectivity of the detection can be improved through electrode modifications, including electropolymerization to form polymer membranes on electrode surfaces.¹⁹ Many studies have used electrochemical techniques to detect NO,^{12, 19-23} though a limited number have employed DETA/NO as the donating compound.^{24, 25} The use of DETA/NO as a donor for electrochemical NO detection can be advantageous as the long half-life of DETA/NO provides easily controllable experimental conditions by generating a more constant NO concentration relative to other donors. Electrochemical methods can also provide multiplexed analyte detection with spatial resolution by arranging electrodes in an array.

One advantage of microelectrodes made using modern microfabrication methods is the ability to create arrays that provide spatial resolution. One method to fabricate electrode arrays uses Silicon Metal Oxide Semiconductor (MOS) processes standard to the modern semiconductor industry. Silicon MOS microchips incorporating Complementary Metal Oxide Semiconductor (CMOS) circuits have been used for a wide range of electrochemical sensor applications including measuring neurotransmitter release from chromaffin cells,²⁶ constructing

portable cell-based biosensors,²⁷ and development of a multiplexed electrochemical biosensor using a label-free, DNA hybridization-based sensor.²⁸ Silicon MOS technology has been employed to fabricate high-density electrode arrays,²⁹ allowing electrochemical detection with high spatiotemporal resolution. The density of the electrode array determines the spatial resolution capabilities of the CMOS chip, and on-board electronics can be incorporated to form expanded biosensor systems to allow simultaneous monitoring at each electrode to provide temporal resolution.^{26, 30} These advantages make the silicon-based electrode arrays ideal as a spatiotemporal biosensor for directly monitoring chemical release from cells in tissue slices or cells in dissociated cultures.

In this study, analysis of NO released from DETA/NO using silicon-based microelectrodes in a microfluidic flow system is reported as a first step towards high resolution *in vitro* and *in vivo* monitoring. Potential interfering species were studied using voltammetry, and an electrochemical cleaning method is reported that minimizes the effect of electrode fouling. The detection of NO from DETA/NO by flow injection analysis resulted in a 94±1% signal loss over 10 sequential injections when no cleaning method was used. Cleaning the electrodes prior to each injection reduced this to a 17±13% signal loss over 10 sequential injections. The sensor response was linear for NO detection from 90 nM to 1.0 µM ($R^2=0.9987$), spanning the reported cellular concentration range.^{31, 32}

Experimental

Materials and Instrumentation

All chemicals were at least of ACS grade and were used as received without further purification. SU-8 2075 photoresist was obtained from MicroChem (Westborough, MA, US). Sylgard 184 poly(dimethylsiloxane) (PDMS) oligomer and cross-linker were purchased from Dow Corning (Midland, MI, US). Hexamethyldisilazane (HMDS), diethylenetriamine (DETA),

Tween-20, HCl, KCl, Na₂HPO₄, and KH₂PO₄ were obtained from Sigma-Aldrich (St. Louis, MO, US). NaNO₂ was purchased from Fisher (Fair Lawn, NJ, US), and NaCl was purchased from Macron (Avantor, Center Valley, PA, US). All solutions were prepared using 18.2 MΩ·cm water from a MilliPore (Billerica, MA, US) Milli-Q system. Phosphate buffered saline (PBS) was prepared from 8.00 g NaCl, 0.20 g KCl, 1.44 g Na₂HPO₄, 0.24 g KH₂PO₄ in 1 L of water, and the pH was adjusted to 7.4 with HCl. All electrochemical experiments were performed using an eDAQ Picostat and e-corder 1621, with eDAQ EChem v2.1 software for voltammetry and eDAQ Chart v5.5.8 for amperometry (eDAQ, Denistone East, Australia). Chemiluminescence experiments were performed using a GE 280i Nitric Oxide Analyzer (GE Analytical Instruments, Boulder, CO, US).

The microelectrodes were produced by Avago Technologies (Fort Collins, CO, US) using silicon-based MOS technology and were arranged into 21 groups as previously described.³³ A probe station (Micromanipulator Inc., Carson City, NV, US) was used to make electrical contact with the silicon microelectrode chip. The probe station was surrounded by a copper faraday cage to reduce electrical noise. Fluid control was accomplished using a NE-1000 Single Syringe Pump (New Era Pump Systems, Farmingdale, NY, US).

Design and Fabrication of Microfluidic Device

A microfluidic manifold was created using a combination of soft lithography, laser cutting, and 3D printing. The design of the microfluidic manifold and silicon microelectrode chip is shown in Figure 5.1. Figure 5.1A shows a schematic of the four-layered device used to house the silicon microelectrode chip (Figure 5.1B). A microfluidic flow channel was fabricated using standard photolithography and soft lithography techniques.^{34, 35} SU-8 2075 photoresist was spin coated onto a 10-cm diameter silicon wafer (Silicon Inc., Boise, ID, US) to give a final feature height of 174 μm as measured by a ZeScope optical profilometer (Zygo, Middlefield, CT, US). UV exposure was performed with a photomask (CAD/Art Services, Inc., Bandon, OR, US) to

generate a mold for a fluidic channel with dimensions 1.5 mm × 20 mm. The mold was coated with HMDS and baked at 115 °C for 15 min. Standard soft lithography was performed using a degassed 10:1 mixture of PDMS oligomer and cross-linker to generate microfluidic channels. Inlet and outlet ports were cut using 1.5-mm diameter biopsy punches (Robbins Instruments, Inc., Chatham, NJ, US).

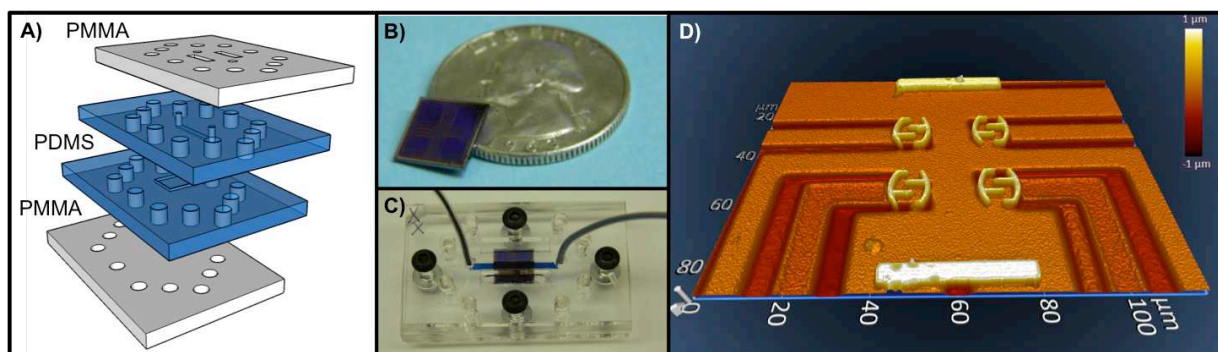


Figure 5.1: Microfluidic setup for the microelectrode chip. **A)** Schematic of device layers and assembly. The bottom and top are PMMA with holes for assembly and access to chip contact pads. The PDMS layers serve to house the microelectrode chip and provide a fluidic interface with the microelectrodes. **B)** 1 cm × 1 cm silicon microelectrode chip, with quarter for size reference. **C)** Assembled device containing the chip. Blue dye is added to the channel for visualization. **D)** One set of microelectrodes on the chip imaged by optical profilometry. The sensor is composed of eight interdigitated working electrodes, a reference electrode at the top, and an auxiliary electrode at the bottom. Scale in z-dimension ranges from -1 μm to 1 μm.

The bottom PDMS layer of the device was fabricated by gluing a microelectrode chip onto a glass slide, coating it with HMDS and baking at 115 °C for 15 min, and pouring 10:1 PDMS over the chip. The PDMS was used to house a microelectrode chip under the microfluidic channel. Outer plates were cut from 1/8-inch poly(methyl methacrylate) (PMMA) (Fort Collins Plastics, CO, US) using a laser engraving system (30 W Epilog, Golden, CO, US) with holes for assembly and access to the contact pads for the microelectrodes. The microelectrode chip was placed in the bottom PDMS layer, and the microfluidic channel was aligned over the electrodes. The device layers were held together using 3-mm diameter, 20-mm long bolts (Figure 5.1C) and placed in a 3D-printed holder (A-101, Lulzbot, Loveland, CO, US) to interface with the microscope stage. FEP tubing (0.01" ID, 0.0625" OD, IDEX Health and Science, Oak Harbor,

WA, US) was inserted into the PDMS ports for interfacing the chip with fluid. One set of microelectrodes on the chip was imaged by optical profilometry (Figure 5.1D) and was previously determined to have the optimal electrode geometry among the electrodes on the chip.³³ The set of electrodes used for this work is composed of eight interdigitated working electrodes, a pseudo-reference electrode, and an auxiliary electrode. All microelectrodes on the chip are coated with 700-800 nm Pt with Al routing from the base of the microelectrodes to contacting pads on the edge of the chip. The line width of the microelectrode pattern (Figure 5.1D) is 2 μm .

Preparation of DETA/NO

DETA/NO was prepared using a previously reported method.¹⁵ Briefly, the parent amine, DETA, was reacted in acetonitrile with 80-psi nitric oxide for 24 h. The material was then filtered and rinsed with acetonitrile, placed under vacuum for 5 h to remove remaining solvent, and stored at -20 °C. Purity was determined using UV-Vis analysis.

Electrochemical Characterization using Differential Pulse Voltammetry

Differential pulse voltammetry (DPV) was performed with 10 mM DETA/NO and 10 mM DETA prepared separately in PBS. The microfluidic channel was filled with the analyte solution, and voltammetry was performed without flow using previously reported parameters.²⁴ The scan range was +0.2 V to +1.0 V (vs. Pt) at a scan rate of 5 mV s^{-1} , with pulse amplitude of 50 mV and pulse width of 70 ms.

Electrochemical Cleaning of Electrodes

An electrochemical cleaning method was developed and optimized to maintain injection-to-injection signal levels. The cleaning method employed a two-step procedure in PBS flowing at 50 $\mu\text{L min}^{-1}$. In the first step, +1.2 V was applied for 100 ms. In the second step, two pulses at

-1.2 V, each 800 ms long, were applied 400 ms apart (Figure 5.2). This cleaning procedure was used prior to every sample injection in flow injection analysis unless otherwise noted.

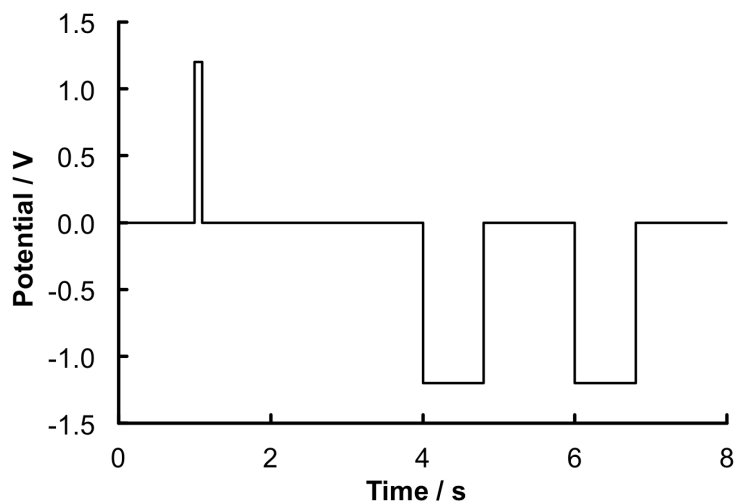


Figure 5.2: Waveform of 2-step cleaning method. The first step is a 100-ms pulse at +1.2 V (vs. Pt). The second step is two 800-ms pulses at -1.2 V that are 1.2 s apart.

Hydrodynamic Voltammograms

The effect of applied potential on the output current was studied for DETA/NO and possible interferences DETA and nitrite.¹³ Both DETA and nitrite are byproducts generated during the detection of NO from DETA/NO. DETA is generated as DETA/NO decomposes and releases NO, and nitrite is produced after the nitrosonium ion (the oxidation product of NO) reacts with hydroxide in solution.¹³ DETA/NO, DETA, and nitrite were prepared separately in PBS at concentrations of 3.5 mM, 5.0 mM, and 10 μ M, respectively. Flow injection analysis was performed applying potentials from 0 to +0.8 V (vs. Pt) in 0.1 V increments. Nitrite was only analyzed up to +0.7 V because the nitrite signal became indistinguishable from baseline noise at higher potentials. Samples were injected (n=3) at 10 μ L volumes into PBS flowing at 50 μ L min^{-1} . Signal was calculated as peak area, and baseline noise was calculated at each potential as the standard deviation of blank injections of PBS (n=6). Error bars represent the standard deviation of replicate (n=3) sample injections.

Sensor Response

The response of the sensor to DETA/NO was evaluated using flow injection analysis. DETA/NO samples (0.5-10 mM) in PBS were injected (n=4) at 10 μL volumes into PBS flowing at 50 $\mu\text{L min}^{-1}$ using an applied potential of +0.6 V (vs. Pt).

NO Concentration Validation by Chemiluminescence

DETA/NO solutions were simultaneously monitored using chemiluminescent and electrochemical methods to determine the concentration of NO generated by DETA/NO. A commercial Nitric Oxide Analyzer (NOA) was used for chemiluminescent detection. All measurements were performed at room temperature. NOA calibration was performed using nitrogen (zero gas) and 45 ppm NO/nitrogen. The cell pressure was maintained in the range of 5.5 to 8.5 torr, and the supply pressure was maintained in the range of 4.6 to 6.5 psi. The photomultiplier tube cooler temperature was set at -12 °C. An empty NOA cell was used to collect baseline measurements for 5 min. Next, 2 mL of PBS was added to the NOA cell. To perform simultaneous electrochemical detection, 200- μL aliquots were removed from the cell and used to fill the 10- μL injection loop for the microelectrode chip. Injections were made into PBS flowing at 50 $\mu\text{L min}^{-1}$ using an applied potential of +0.6 V (vs. Pt). Replicate injections (n=3) were performed from sequential 200- μL aliquots removed from the NOA cell. This process was repeated with DETA/NO solutions (1.0-10 mM) in PBS.

Results and Discussion

Differential Pulse Voltammetry of DETA/NO

Differential pulse voltammetry (DPV) of DETA/NO and DETA in PBS was performed to determine the optimum oxidation potential for NO detection from DETA/NO without interference from DETA. Oxidation of NO released from DETA/NO occurs at a lower potential than DETA (Figure 5.3), allowing detection of NO from DETA/NO without interference from DETA present in

the solution. DPV of DETA/NO has previously resulted in an oxidation peak at +0.8 V vs. Ag/AgCl,²⁴ which corresponds to the oxidation potential of NO,²⁰ indicating that the current observed on the electrodes is a result of NO oxidation rather than oxidation of the DETA/NO molecule. DETA, a byproduct of DETA/NO decomposition, can be oxidized at high potentials due to the presence of amine functional groups. Oxidation of DETA on platinum electrodes has previously been studied using cyclic voltammetry, and the anodic current peak occurred at 1.25 V vs. Ag/AgCl, though the peak potential was observed to shift with different supporting electrolytes.³⁶ The DPV shown here for DETA reaches the maximum oxidation current at approximately 0.9 V, with negligible signal observed at the 0.6 V used for NO detection.

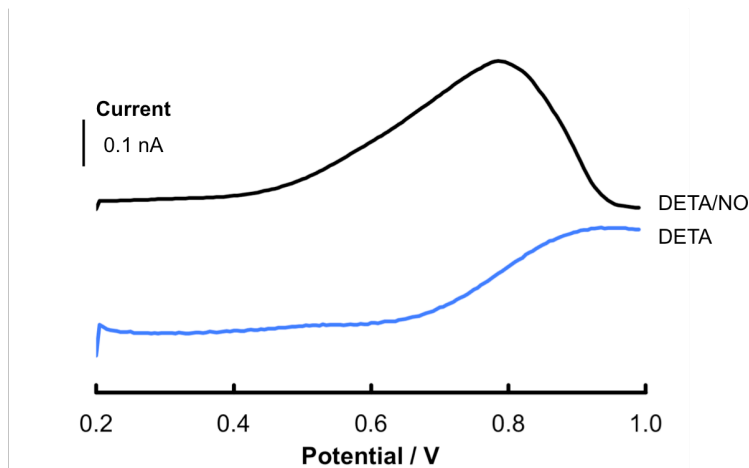


Figure 5.3: Representative scans of 10 mM DETA/NO (—) and 10 mM DETA (—) in PBS pH 7.4. Experimental conditions for differential pulse voltammetry: range +0.2 V to +1.0 V (vs. Pt), pulse amplitude 0.050 V, pulse width 70 ms, scan rate 5 mV s⁻¹. Voltammograms offset for visualization.

Electrode Fouling

A loss in electrochemical signal from DETA/NO was observed with subsequent injections in flow injection experiments likely due to oxidative polymerization of DETA on the platinum surface.^{36, 37} The DETA generated from the decomposition of DETA/NO contacts the electrode surface, resulting in the formation of a coating that decreases the working area of the electrode. Sets of 10 sequential injections of 12.5, 6.25, and 1.25 mM DETA/NO resulted in a

60±8% loss in signal after one injection, and a 94±1% loss in signal after 10 injections (Figure 5.4).

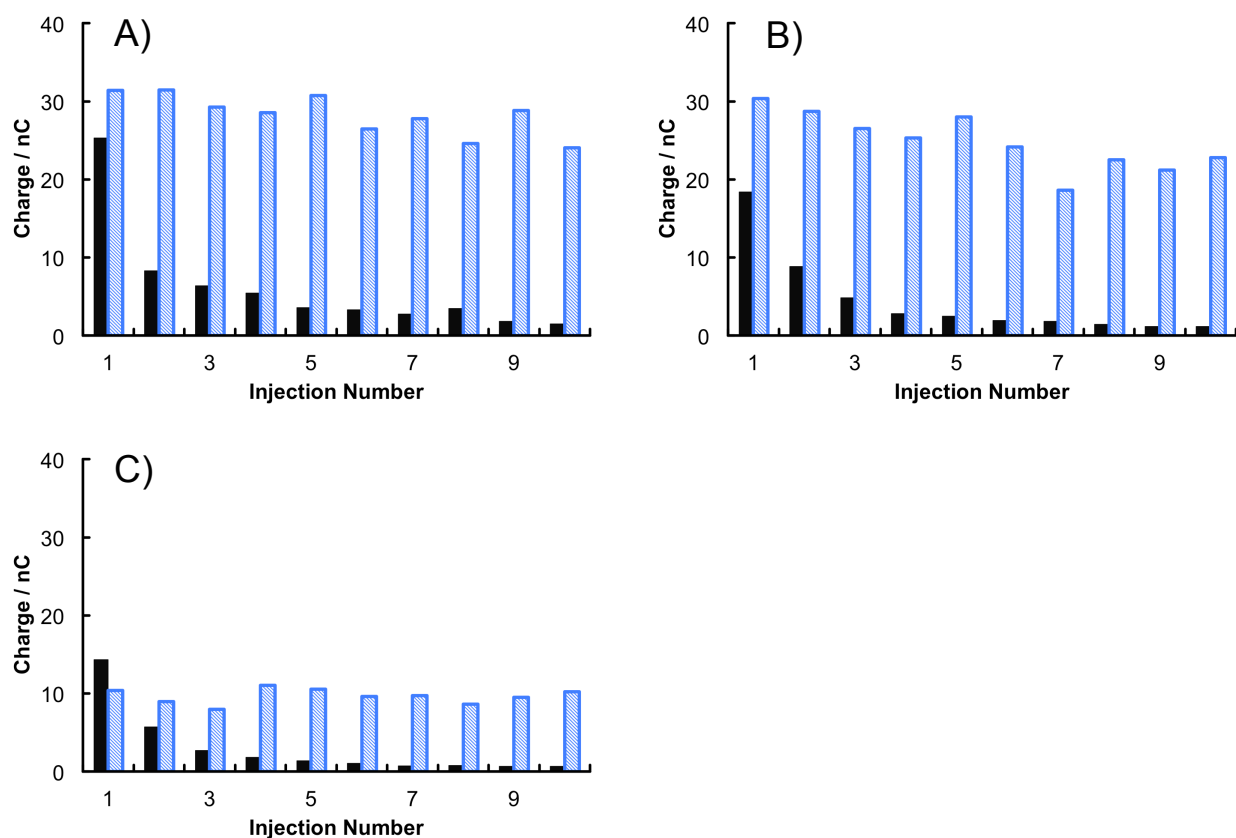


Figure 5.4: Fouling and electrochemical cleaning of electrode surface. Signal plotted as peak area from sequential 10 μL injections of **A)** 12.5 mM DETA/NO (2.5 μM NO) **B)** 6.25 mM DETA/NO (1.25 μM NO) or **C)** 1.25 mM DETA/NO (0.25 μM NO) without (■) and with (▨) electrochemical cleaning step prior to each injection in PBS pH 7.4. Applied potential of 0.6 V (vs. Pt). Flow rate 50 $\mu\text{L min}^{-1}$.

Multiple methods were investigated to reduce or eliminate electrode fouling. Previous studies have shown that surfactants can minimize fouling of the electrode surface.^{38, 39} Injecting a surfactant, 1 mM Tween-20, with the DETA/NO solution to prevent material from accumulating on the electrode surface did not prevent signal degradation (Figure 5.5). Electrochemical cleaning methods have been previously reported to remove material from the electrode surface and maintain constant performance.^{40, 41} After investigating multiple waveforms (Figure 5.6), a two-step electrochemical cleaning method was employed prior to every injection. Manica *et al.*⁴⁰

reported that applying a high oxidation potential to platinum electrodes removes adsorbed organic materials by forming platinum oxide. Applying a subsequent reduction potential will reduce the platinum oxide and regenerate the original electrode surface. In the electrochemical cleaning waveform employed here, +1.2 V was applied for 100 ms followed by two pulses at -1.2 V, each 800 ms long and 400 ms apart (Figure 5.2). Using the cleaning method prior to every injection reduced the signal loss to $17\pm 13\%$ over 10 injections for 12.5, 6.25, and 1.25 mM DETA/NO with variation in signal across those injections of $11\pm 3\%$ relative standard deviation, indicating that the electrochemical cleaning method was effective at preventing a significant loss in signal (Figure 5.4). Alternative multistep waveforms were investigated utilizing different cleaning potentials, waveform times, and pulse repetitions. These waveforms either did not significantly affect the signal degradation, or were not as effective as the method described above.

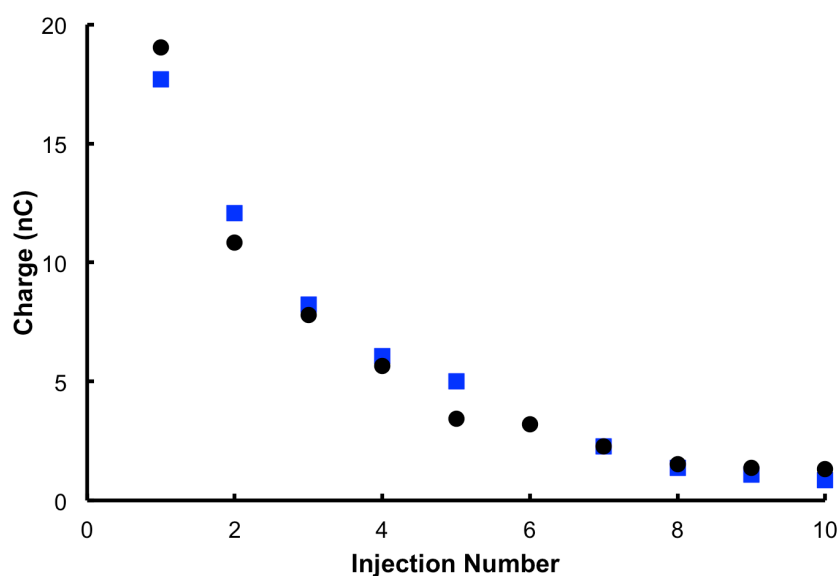


Figure 5.5: Sequential injections of 50 mM DETA/NO without (●) and with (■) alternating 1 mM Tween-20 injections. Flow rate $50 \mu\text{L min}^{-1}$. Applied potential of 0.6 V (vs. Pt).

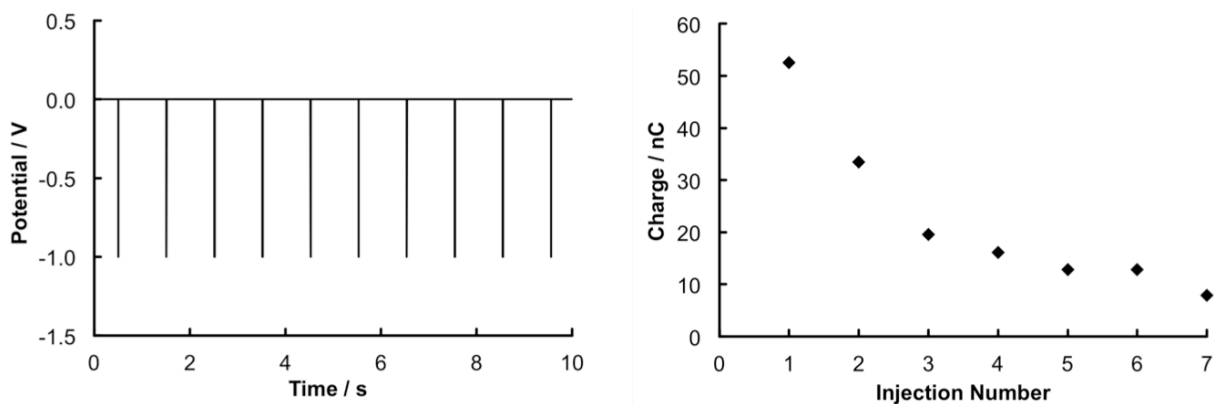


Figure 5.6: Ineffective electrochemical cleaning method. Left panel is waveform of electrochemical cleaning method used in PBS pH 7.4 prior to each injection: 10 pulses 5 ms long at -1 V, 1 s between each pulse. Right panel shows sequential 10 μL injections of 50 mM DETA/NO (10 μM NO) plotted as peak area. Flow rate 50 $\mu\text{L min}^{-1}$. Applied potential of 0.6 V (vs. Pt).

Effect of Applied Potential

Hydrodynamic voltammograms (HDV) of DETA/NO and possible interferences, DETA and nitrite,¹³ were next generated to study the effect of applied potential on electrochemical response (Figure 5.7). The response was plotted as the ratio of signal to noise, where the signal was the integrated peak area ($n=3$), and noise was the standard deviation of the peak area of blank injections ($n=6$) at each potential. The 10 μM nitrite concentration was chosen as it represents the theoretical maximum concentration present in the DETA/NO solutions at the time of analysis, and nitrite is present at nanomolar to micromolar concentrations *in vivo*.^{42, 43} Nitrite generated a negligible signal relative to DETA/NO at all applied potentials. The DETA/NO and DETA responses noticeably increase at 0.6 V and above. The signal was less stable at higher applied potentials, leading to an increase in the variation between injections. An applied oxidation potential of 0.6 V was selected for all subsequent experiments because the DETA/NO signal response is distinguishable from that of DETA, and is more precise than at higher potentials, and the potential is low enough to avoid interfering signals from many naturally occurring species in real samples.

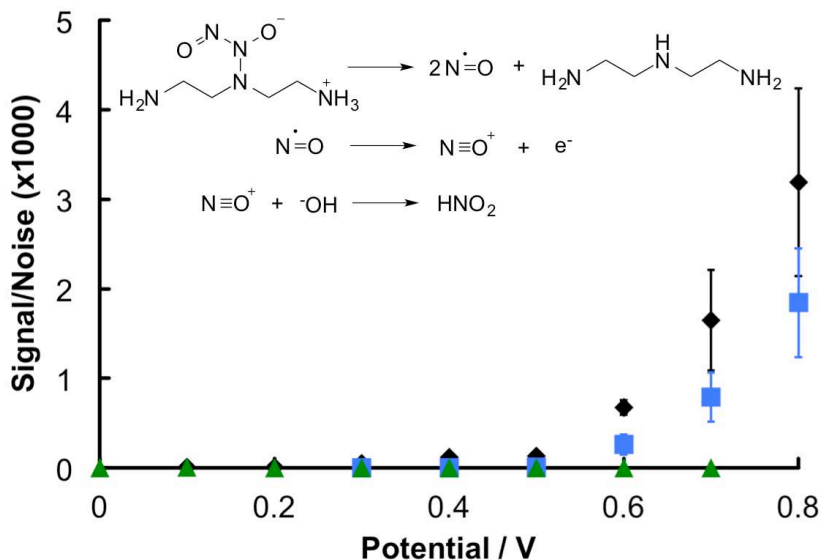


Figure 5.7: Hydrodynamic voltammograms of 3.5 mM DETA/NO (710 nM NO) (◆), 2.5 mM DETA (■), and 10 μM sodium nitrite (▲). Signal is calculated as peak area, and noise is calculated as the standard deviation of the peak area for 6 blank injections at the corresponding potential. Error bars are the standard deviation of replicate 10 μL injections ($n=3$). Species being analyzed are shown in the reactions at the top of the figure. Flow rate 50 $\mu\text{L min}^{-1}$. Potential applied vs. Pt.

Sensor Response

The response of the sensor to NO was evaluated using flow injection analysis of DETA/NO (Figure 5.8). The NO concentration produced from the decomposition of DETA/NO was determined using a commercial NOA. The response from the microelectrodes follows a non-linear trend over the concentration range studied. The response can be approximated as linear ($R^2=0.9987$) in the range of 90 nM to 1 μM NO, which spans the estimated range of cellular NO concentration,^{31, 32} making this electrode system a viable technique for monitoring NO released from cells in dissociated cultures or tissue slices. Deviations from linearity at high concentrations may be a result of decreasing collection efficiency with increasing concentration. Collection efficiency was calculated assuming all NO injected could reach the electrode surface, and resulted in a 3-17% range. The collection efficiency is low because of the size of the

working electrode relative to the dimensions of the flow channel, the analysis was performed at a fast flow rate, and the rate of diffusion of DETA/NO to the surface of the electrodes.

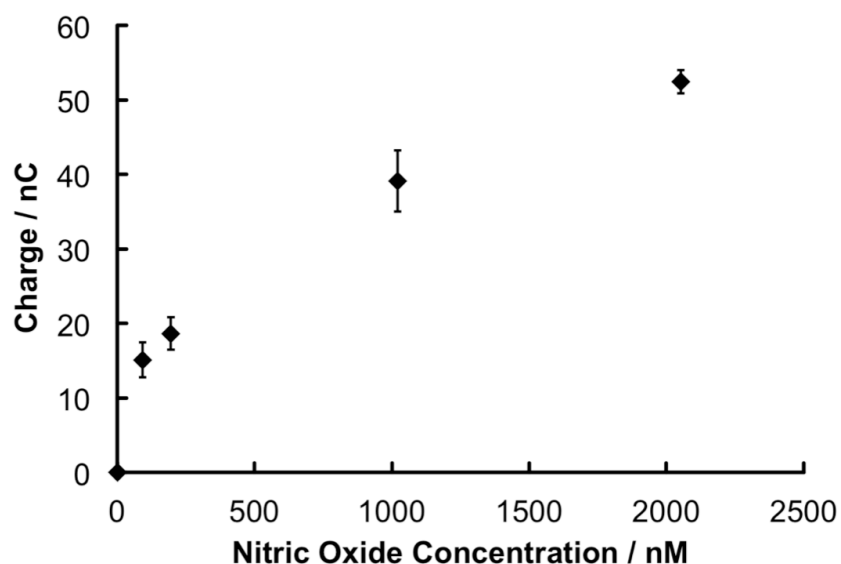


Figure 5.8: Nitric oxide calibration curve from flow injection analysis of DETA/NO in PBS pH 7.4. Signal is plotted as peak area, with error bars representing the standard deviation of replicate 10 μL injections ($n=4$). Flow rate 50 $\mu\text{L min}^{-1}$. Applied potential of 0.6 V (vs. Pt).

Conclusions

The work reported here has shown that platinum microelectrodes are a viable technique for monitoring NO. Use of the NO donor DETA/NO results in electrode fouling, but a method for electrochemically cleaning these microelectrodes was demonstrated. The response of the CMOS chip as a function of NO concentration requires further investigation to explain deviations from linearity, but exhibits moderate linearity within the range of cellular NO concentrations. This system can be further developed to generate an array of CMOS electrodes capable of detecting NO release from cells in dissociated cell cultures or tissue slices with high spatiotemporal resolution.

This work is supported in part by National Science Foundation Grant No. GDE-0841259. The authors gratefully acknowledge Sarah M. Lantvit, Jessica M. Joslin, and Bella Neufeld at Colorado State University for synthesizing DETA/NO and use of their NOA. The silicon-based

microelectrode chip was manufactured by Avago Technologies. Their technical assistance and generous support for this project are greatly appreciated.

REFERENCES

1. R. M. Feeny, J. B. Wydallis, T. Chen, S. Tobet, M. M. Reynolds and C. S. Henry, *Electroanalysis*, 2014, **26**.
2. R. M. J. Palmer, A. G. Ferrige and S. Moncada, *Nature*, 1987, **327**, 524-526.
3. M. R. Schaffer, U. Tantry, S. S. Gross, H. L. Wasserkrug and A. Barbul, *Journal of Surgical Research*, 1996, **63**, 237-240.
4. M. B. Witte and A. Barbul, *American Journal of Surgery*, 2002, **183**, 406-412.
5. M. Ziche and L. Morbidelli, *Journal of Neuro-Oncology*, 2000, **50**, 139-148.
6. E. Pipilisynetos, E. Sakkoula and M. E. Maragoudakis, *British Journal of Pharmacology*, 1993, **108**, 855-857.
7. S. H. Snyder, *Science*, 1992, **257**, 494-496.
8. M. A. Degroote and F. C. Fang, *Clinical Infectious Diseases*, 1995, **21**, S162-S165.
9. G. Bicker, *Bioessays*, 2005, **27**, 495-505.
10. S. Bulotta, C. Perrotta, A. Cerullo, C. De Palma, E. Clementi and N. Borgese, *Neurotoxicology*, 2005, **26**, 841-845.
11. A. Contestabile and E. Ciani, *Neurochemistry International*, 2004, **45**, 903-914.
12. T. L. Xu, N. Scafa, L. P. Xu, L. Su, C. Z. Li, S. F. Zhou, Y. Liu and X. J. Zhang, *Electroanalysis*, 2014, **26**, 449-468.
13. L. K. Keefer, R. W. Nims, K. M. Davies and D. A. Wink, *Nitric Oxide, Pt a - Sources and Detection of No; No Synthase*, 1996, **268**, 281-293.
14. J. M. Joslin, S. M. Lantvit and M. M. Reynolds, *Acs Applied Materials & Interfaces*, 2013, **5**, 9285-9294.
15. J. A. Hrabie, J. R. Klose, D. A. Wink and L. K. Keefer, *Journal of Organic Chemistry*, 1993, **58**, 1472-1476.
16. K. M. Davies, D. A. Wink, J. E. Saavedra and L. K. Keefer, *Journal of the American Chemical Society*, 2001, **123**, 5473-5481.
17. O. C. Zafiriou and M. McFarland, *Analytical Chemistry*, 1980, **52**, 1662-1667.
18. F. L. Kiechle and T. Malinski, *American Journal of Clinical Pathology*, 1993, **100**, 567-575.
19. F. Bedioui and N. Villeneuve, *Electroanalysis*, 2003, **15**, 5-18.
20. D. Christodoulou, S. Kudo, J. A. Cook, M. C. Krishna, A. Miles, M. B. Grisham, R. Murugesan, P. C. Ford and D. A. Wink, *Nitric Oxide, Pt a - Sources and Detection of No; No Synthase*, 1996, **268**, 69-83.

21. C. Amatore, S. Arbault and A. C. W. Koh, *Analytical Chemistry*, 2010, **82**, 1411-1419.
22. K. Shibuki, *Neuroscience Research*, 1990, **9**, 69-76.
23. C. Calas-Blanchard, G. Catanante and T. Noguer, *Electroanalysis*, 2014, **26**, 1277-1286.
24. V. C. Diculescu, R. M. Barbosa and A. M. O. Brett, *Analytical Letters*, 2005, **38**, 2525-2540.
25. N. R. Ferreira, A. Ledo, J. G. Frade, G. A. Gerhardt, J. Laranjinha and R. M. Barbosa, *Analytica Chimica Acta*, 2005, **535**, 1-7.
26. B. N. Kim, A. D. Herbst, S. J. Kim, B. A. Minch and M. Lindau, *Biosensors & Bioelectronics*, 2013, **41**, 736-744.
27. B. D. DeBusschere and G. T. A. Kovacs, *Biosensors & Bioelectronics*, 2001, **16**, 543-556.
28. J. Rothe, M. K. Lewandowska, F. Heer, O. Frey and A. Hierlemann, *Journal of Micromechanics and Microengineering*, 2011, **21**, 10.
29. K. M. Roth, K. Peyvan, K. R. Schwarzkopf and A. Ghindilis, *Electroanalysis*, 2006, **18**, 1982-1988.
30. S. Ayers, K. D. Gillis, M. Lindau and B. A. Minch, *Ieee Transactions on Circuits and Systems I-Regular Papers*, 2007, **54**, 736-744.
31. M. B. Grisham, D. Jourd'Heuil and D. A. Wink, *American Journal of Physiology-Gastrointestinal and Liver Physiology*, 1999, **276**, G315-G321.
32. D. A. Wink and J. B. Mitchell, *Free Radical Biology and Medicine*, 1998, **25**, 434-456.
33. W. Pettine, M. Jibson, T. Chen, S. Tobet, P. Nikkel and C. S. Henry, *Ieee Sensors Journal*, 2012, **12**, 1187-1192.
34. D. C. Duffy, J. C. McDonald, O. J. A. Schueller and G. M. Whitesides, *Analytical Chemistry*, 1998, **70**, 4974-4984.
35. Y. Sameenoi, M. M. Mensack, K. Boonsong, R. Ewing, W. Dungchai, O. Chailapakul, D. M. Crokek and C. S. Henry, *Analyst*, 2011, **136**, 3177-3184.
36. L. Ouattara, T. Diaco and Y. Bokra, *Bulletin of the Chemical Society of Ethiopia*, 2006, **20**, 269-277.
37. G. Herlem, K. Reybier, A. Trokourey and B. Fahys, *Journal of the Electrochemical Society*, 2000, **147**, 597-601.
38. B. Hoyer and N. Jensen, *Electroanalysis*, 2005, **17**, 2037-2042.
39. B. Hoyer and N. Jensen, *Electrochemistry Communications*, 2006, **8**, 323-328.
40. D. P. Manica, Y. Mitsumori and A. G. Ewing, *Analytical Chemistry*, 2003, **75**, 4572-4577.
41. H. Moller and P. C. Pistorius, *Journal of Electroanalytical Chemistry*, 2004, **570**, 243-255.

42. J. Rodriguez, R. E. Maloney, T. Rassaf, N. S. Bryan and M. Feelisch, *Proceedings of the National Academy of Sciences of the United States of America*, 2003, **100**, 336-341.
43. P. Kleinbongard, A. Dejam, T. Lauer, T. Rassaf, A. Schindler, O. Picker, T. Scheeren, A. Godecke, J. Schrader, R. Schulz, G. Heusch, G. A. Schaub, N. S. Bryan, M. Feelisch and M. Kelm, *Free Radical Biology and Medicine*, 2003, **35**, 790-796.

CHAPTER 6. SPATIOTEMPORAL NOREPINEPHRINE MAPPING USING A HIGH-DENSITY CMOS MICROELECTRODE ARRAY

A high-density amperometric electrode array containing 8,192 individually addressable platinum working electrodes with an integrated potentiostat fabricated using Complementary Metal Oxide Semiconductor (CMOS) processes is reported. The array was designed to enable electrochemical imaging of chemical gradients with high spatiotemporal resolution. Electrodes are arranged over a 2 mm × 2 mm surface area into 64 subarrays consisting of 128 individual Pt working electrodes as well as Pt pseudo-reference and auxiliary electrodes. Amperometric measurements of norepinephrine in tissue culture media were used to demonstrate the ability of the array to measure concentration gradients in complex media. Poly(dimethylsiloxane) microfluidics were incorporated to control the chemical concentrations in time and space, and the electrochemical response at each electrode was monitored to generate electrochemical heat maps, demonstrating the array's imaging capabilities. A temporal resolution of 10 ms can be achieved by simultaneously monitoring a single subarray of 128 electrodes. The entire 2 mm × 2 mm area can be electrochemically imaged in 64 seconds by cycling through all subarrays at a rate of 1 Hz per subarray. Monitoring diffusional transport of norepinephrine is used to demonstrate the spatiotemporal resolution capabilities of the system. This work was published in *Lab on a Chip* in 2015, and resulted from a collaborative effort.¹ John Wydallis and Rachel Feeny designed and fabricated the microfluidic devices used, and performed the data collection and analysis, and William Wilson and Tucker Kern designed and built the supporting electronics required to operate the system and wrote the MATLAB scripts for operating the system and electrochemical image generation.

Introduction

Molecular gradients are important driving forces in biology, directing phenomena such as chemotaxis,²⁻⁴ cancer metastasis,⁵ and cell-to-cell communication.⁶⁻⁸ These processes occur over multiple length scales, ranging from synaptic gaps in angstroms to entire organs in centimeters, and time periods ranging from milliseconds to minutes. The ability to simultaneously monitor chemical gradients and observe cellular responses to those gradients across multiple length scales can provide a critical foundation for understanding biological phenomena.

Monitoring biological processes driven by molecular gradients requires a system capable of generating images with high spatiotemporal resolution and chemical selectivity. Optical and fluorescence microscopies have long been used to observe molecular gradients in biology. Microscopy techniques are ideal in many respects for monitoring chemical gradients in biological systems with spatial and temporal resolution. Unstained living tissue can be imaged using endogenous fluorophores, such as nicotinamide adenine dinucleotide (NADH) and hemoglobin,^{9, 10} avoiding the necessity for exogenous probes. Genetic modification, stains, and probes, including fluorescent proteins, quantum dots, and metal chelates can be used to expand the library of molecules detectable by fluorescence techniques, but many species remain inaccessible or have altered activity when conjugated with fluorescent probes.¹¹⁻¹³ Other techniques such as mass spectrometry can detect a large library of molecules with spatial resolution, though these systems typically lack the temporal resolution required to monitor dynamic changes in concentration gradients, as tissues are no longer viable at the time of analysis.^{14, 15}

Electrochemistry can provide an alternative way to create a chemical map or “image” that can augment observations from traditional microscopy by detecting, with spatial and temporal resolution, changes in key signaling molecules that cannot be readily measured using microscopy methods. Electrochemical imaging on a microscopic scale has previously been

described in the context of scanning electrochemical microscopy (SECM),¹⁶⁻¹⁸ microfluidic sampling devices,^{19, 20} and microelectrode arrays.²¹⁻²⁵ SECM measures current response from a single electrode rastered over a surface to generate images.¹⁶⁻¹⁸ SECM can provide evidence of chemical release with high spatial resolution but requires physical scanning over the surface and thus has limited temporal resolution. Microelectrode arrays offer improved temporal resolution because the electrodes do not move and multiple electrodes can be operated simultaneously. The Baltes, Hierlemann, and Matsue groups have described micro- and nanoelectrode systems fabricated from Complementary Metal Oxide Semiconductor (CMOS) techniques as analytical tools.²⁶⁻³¹ These reports use high-density electrode systems to map cellular electrical signals with subcellular resolution or use redox cycling to generate electrochemical responses to image chemical distributions. While effective, most electrode array-based imaging applications have used tens of electrodes for cellular or sub-cellular imaging or use larger arrays to define voltage gradients across neuronal networks.^{21, 22, 32-34} Arrays with higher electrode density and/or large numbers of electrodes have primarily been employed for impedance or voltage-based sensing and not amperometric detection.^{24, 35-39} As a preliminary study of the capabilities of an electrode array to image chemical distributions on the scale of an *ex vivo* tissue slice, the system described here was used to image controlled distributions of norepinephrine as a model neurotransmitter.

The system described here uses a high-density electrode array with an on-board potentiostat to make amperometric measurements across a 2 mm x 2 mm array. The array has a spatial resolution of 30 μm , a temporal resolution of 10 ms per 250 μm x 250 μm subarray region, and contains 8,192 individual Pt microelectrodes in addition to on-board reference and auxiliary electrodes. The array was fabricated using standard commercial Complementary Metal Oxide Semiconductor (CMOS) techniques with an added lift-off step to give the final Pt layer for the working electrodes. The die size fits onto the stage of an upright microscope so that optical and electrochemical images can be obtained simultaneously. Images were obtained for

norepinephrine gradients formed *via* either diffusion or hydrodynamic flow directed using a microfluidic device.

Experimental

Materials and Instrumentation

All chemicals were at least of ACS grade and used as received without additional purification. SU-8 2075 photoresist was obtained from MicroChem (Westborough, MA, US). Hexamethyldisilazane (HMDS) and (\pm)-norepinephrine (+)-bitartrate salt were purchased from Sigma-Aldrich (St. Louis, MO, US). Sylgard 184 poly(dimethylsiloxane) (PDMS) oligomer and cross-linker were obtained from Dow Corning (Midland, MI, US). Neurobasal-A media without phenol red was purchased from Life Technologies Corporation (Carlsbad, CA, US) and was used in all electrochemical experiments to demonstrate compatibility with solutions required for sustaining *in vitro* cell and tissue culture. Dyes (FD&C Red #40 and Blue #1) used for solution visualization were purchased from Kroger (Cincinnati, OH, US). External power supplies (HP E3630A and E3631A Triple Output DC Power Supplies, Hewlett Packard, Palo Alto, CA, US) were used to power the system containing the electrode array chip. Optical images and videos were collected using a commercial smartphone (Apple Inc., Cupertino, CA, US) and a fluorescent magnifier light (LumaPro, W. W. Grainger, Lake Forest, IL, US). Chip control and data collection were achieved using ADLINK DAQe-2200 data acquisition boards. Data post-processing including electrochemical heat map generation was performed using a suite of MATLAB functions (32 bit and 64 bit, Mathworks, Inc., Natick, MA, US). The electrode array was imaged using a ZeScope optical profilometer (Zygo, Middlefield, CT, US) and a JSM-6500F scanning electron microscope (JEOL USA Inc., Peabody, MA, US).

Electrode Array Design, Fabrication, and Operation

Chip Fabrication and Operation

Figure 6.1 shows optical profilometry and scanning electron microscopy (SEM) images of individual electrodes, a single subarray, and the entire array as well as a photograph of the system after mounting in its ceramic packaging. The electrode array chip was designed in a 0.5- μm 4-layer metal CMOS process. The top layer metal was used for patterning Pt electrodes. The metal layers 1-3 provided necessary routing for the chip.

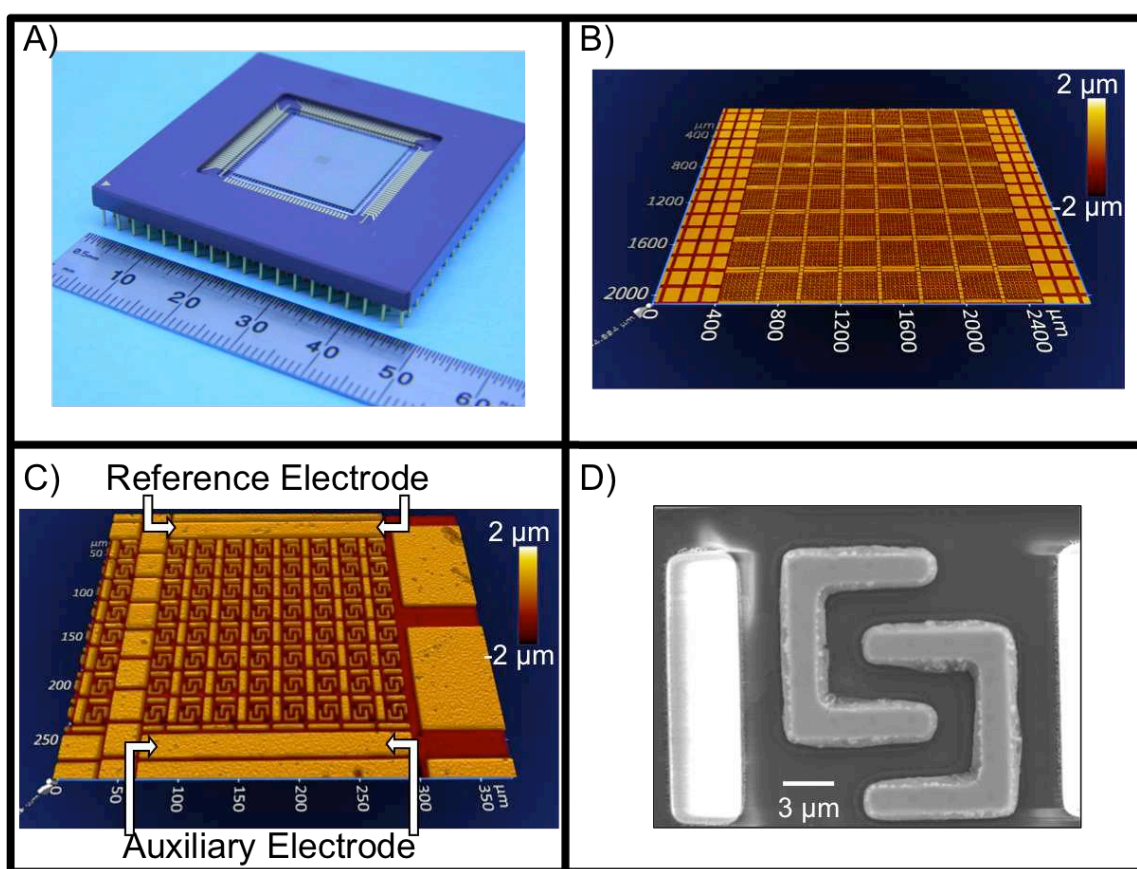


Figure 6.1: Images of the high-density electrode array. **A)** Photograph of CMOS chip containing electrodes and on-chip potentiostat. **B)** Optical profilometry image of entire array showing 64 subarrays. **C)** Optical profilometry image of a single subarray comprised of 128 working electrodes and shared auxiliary and pseudo-reference electrodes. **D)** SEM image of two interdigitated platinum working electrodes 12.5 μm long on the y-axis.

Manufacturing of the electrode array chip was performed by Avago Technologies on 8-inch wafers using Avago's fabrication facility in Fort Collins, Colorado, USA. The die size was $1.9 \times 1.9 \text{ cm}^2$. The process of forming the Pt electrode in the electrode array chip is as follows:

1. The process starts with a lightly doped p-type silicon substrate. (The CMOS process used for the chip is an n-well CMOS process);
2. All on-chip electronic components (logic gates, amplifiers, etc.), including metal routing patterns to connect electrodes on Metal 4 to the I/O pads, are manufactured up to Metal 3 using the standard CMOS manufacturing process;
3. Chemical and mechanical polishing (CMP) is performed to make the post-Metal-3 surface planar;
4. SiO_2 and Si_3N_4 layers are deposited on the surface of the chip. Si_3N_4 acts as the passivation layer;
5. Chemical and mechanical polishing (CMP) is performed to make the surface planar;
6. Etching is performed to allow the formation of contacts from the passivation layer surface to the Metal 3 routing pattern at the base of the electrodes formed in step 2;
7. A Ti/TiN barrier layer is deposited inside the contact well to provide a buffering layer for tungsten;
8. Tungsten is deposited to fill the contact well to form the vertical contact column to the raised electrode on the passivation layer surface;
9. The base of the electrodes at the passivation layer surface using a thin platinum diffusion barrier on the order of tens of nm. This diffusion layer makes electrical contact to the tungsten plug as well as acting as the base layer for Au/Pt tip of the electrodes;
10. The body of the electrode tips on the chip surface is formed using Au with Pt coating surrounding the tips. The height of the tips from the chip surface is $1.5 \mu\text{m}$. The electrodes were intentionally designed to rise above the surface to allow better contact between the electrode and tissue slices that will ultimately be studied.

Figure 6.2 shows the cross section of the electrodes manufactured using the steps described above (not to scale). Figure 6.3 shows the top view of one pair of working electrodes with dimensions clearly marked. The on-chip potentiostat has a voltage regulating error of no more than 8 mV in amperometry mode. In voltammetry mode, it is capable of providing up to 10 kV s^{-1} scan rate with the same voltage regulating error. The on-chip control logic also provides flexibility of connecting any electrodes in a subarray directly to the chip I/O pins to allow direct access of electrodes using external potentiostats.

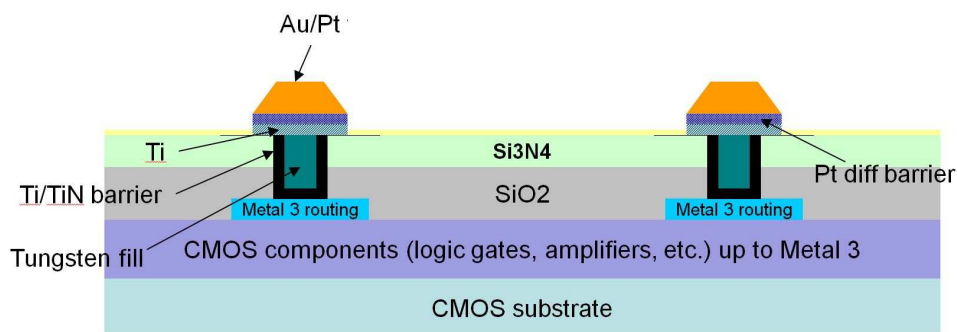


Figure 6.2: Cross section of the Pt electrodes (not to scale).

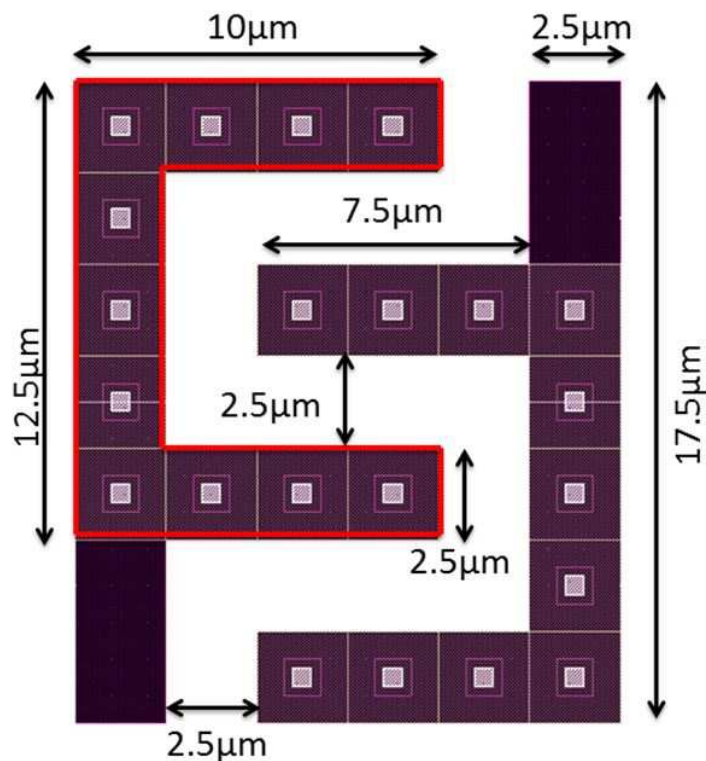


Figure 6.3: A pair of working electrodes designed with an “F” shape.

A 96-input data acquisition card (ADLINK DAQe-2200 series) was used, allowing cycling through 96 of the 128 electrodes on each of the 64 subarrays at set intervals to provide imaging results. In the experiments described here, the data were collected from the array by monitoring individual subarrays and cycling through each subarray vertically, starting in the upper-right corner of the array and ending in the bottom-left corner. The subarray switching parameters are definable by the user in custom-designed MATLAB functions through a windows-based graphical user interface. The current response at individual electrodes was converted to color intensity and plotted to generate electrochemical heat maps using a custom MATLAB program. Table 6.1 details the electrical specifications of the microchip.

Table 6.1: CMOS chip specifications.

Specification	Value
Electrode Pitch	30 μm
Subarray Dimensions	250 μm \times 250 μm (128 electrodes)
Array Dimensions	2 mm \times 2 mm (8192 electrodes)
Maximum Experimental Data Collection Rate (Single Subarray)	100 Hz
Maximum Experimental Data Collection Rate (Entire Array)	0.0156 Hz

Electrode Array Format

All 8,192 working electrodes are located at the center of the chip in a 2 mm \times 2 mm area. Electrodes were grouped in 64 subarrays each with 128 electrodes. Each subarray has its own Pt pseudo-reference electrode (RE) and counter electrode (CE). The design of the working electrodes was previously optimized and used for biomarker detection in a microfluidic manifold.^{40, 41} Figure 6.4 shows the arrangement of 128 working electrodes and RE and CE in each subarray. The electrode array chip is housed in a 280-pin ceramic cavity-up PGA package. There are 128 I/O pads on the ceramic PGA package dedicated to the electrodes in subarrays. All 128 electrodes in a given subarray can be selected and connected to the I/O pads through an on-chip 64-to-1 multiplexer. Finally, the electrodes were connected to on-board logic and a potentiostat circuit capable of addressing 128 electrodes in a subarray as well as switching between subarrays. The on-chip circuits consist of an 8,192-electrode array, electrode subarray selection logic, and a potentiostat circuit for the on-chip RE, CE, and WEs as shown in Figure 6.5. Each electrode in each subarray is connected to a switch that will be turned on or off by a 3:8 decoder. The switches are then connected out to one of the 128 transimpedance amplifiers (TIAs) in the on-board read-channels, as outlined in Figure 6.6. Each of the electrode pairs in the figure represents one 128-electrode subarray, of which there are 64 total. Although there are separate switches for each electrode in a pair, both the vertical and horizontal switches are

controlled by the same decoder so that all 128 electrodes of a single subarray will be on at the same time.

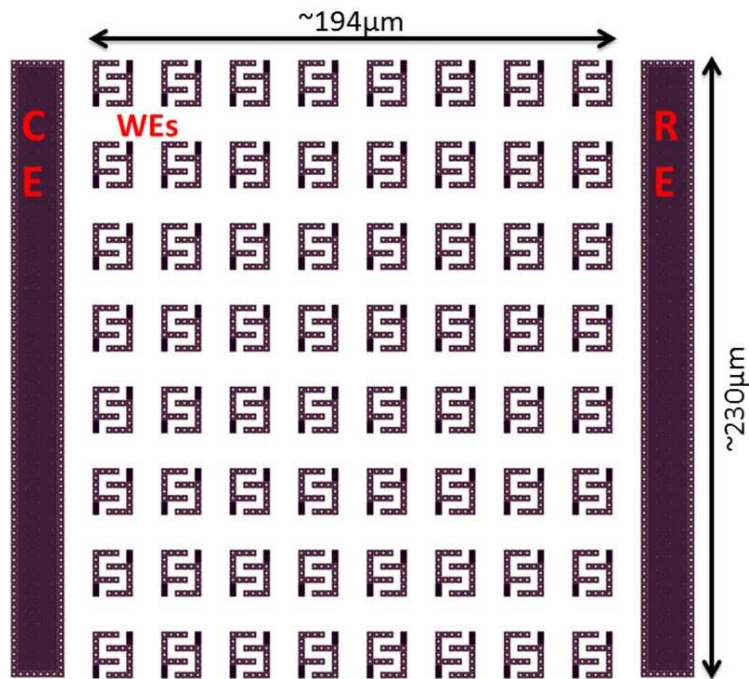


Figure 6.4: A single subarray of 128 working electrodes, one pseudo-reference electrode, and one auxiliary electrode.

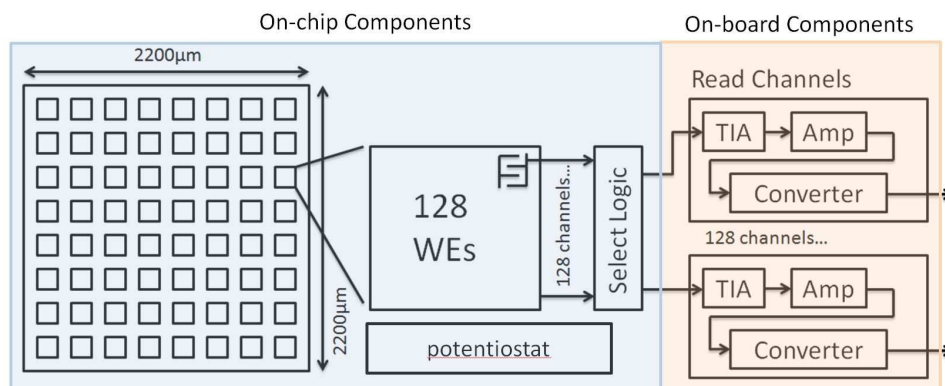


Figure 6.5: On-chip components and how they connect through select logic to 128 on-board read-channels.

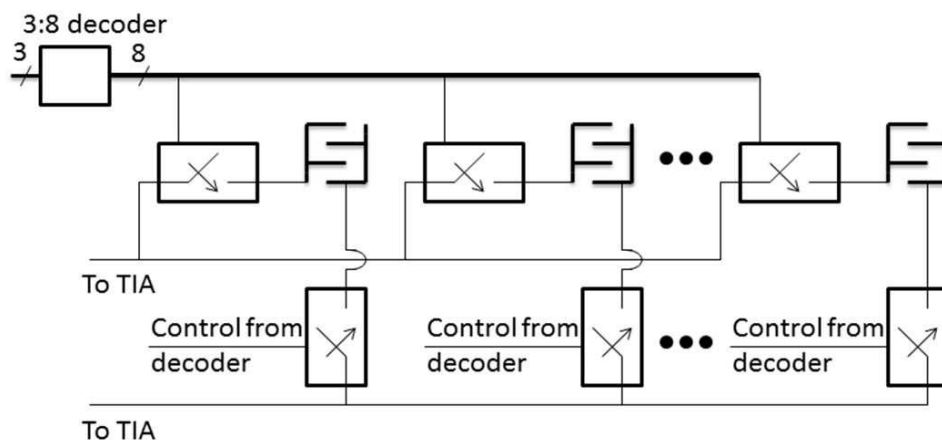


Figure 6.6: Control logic for the electrode subarrays.

Although each subarray has its own reference and auxiliary electrode, only one potentiostat was needed for the entire design. The main goal of the potentiostat is to maintain a constant potential between the working electrodes and a RE while supplying current to a CE. A bias voltage is applied to the RE and the corresponding induced current will describe the concentration of the chemical present at the working electrode. Each of the auxiliary and reference electrodes found in the subarrays is connected together so that only one potentiostat is required to control the entire array. The potentiostat is designed to operate up to $10,000 \text{ V s}^{-1}$ for cyclic voltammetry and in the range of -1 V to $+1 \text{ V}$ for amperometry. The single op-amp structure used for the potentiostat is based on our proposed self-biased inverter based design⁴² and is shown in Figure 6.7.

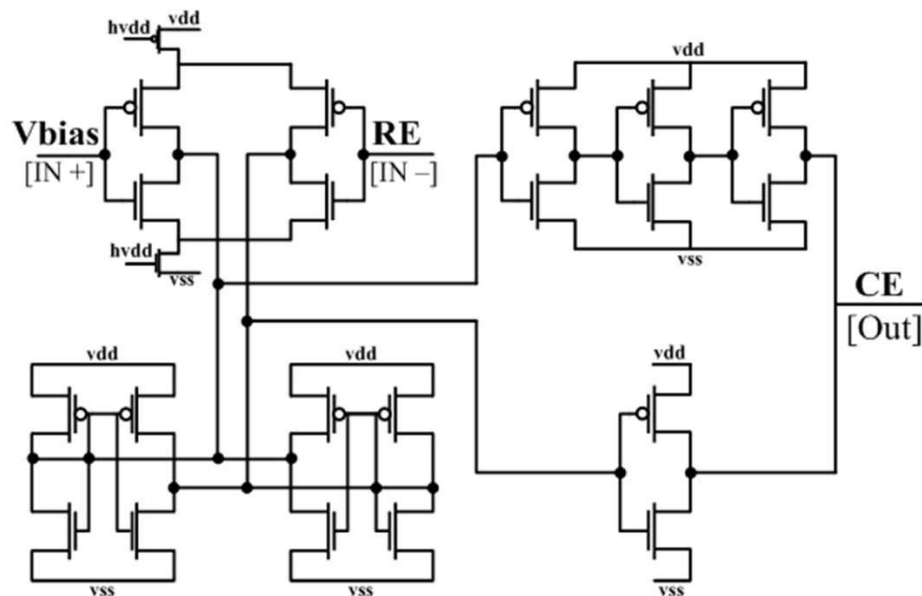


Figure 6.7: A self-biased inverter based potentiostat circuit.

The outputs from 128 selected electrodes are connected to 128 read-channels on a circuit board. Each read-channel on the circuit board consists of a transimpedance amplifier (TIA) and a main amplifier. The transimpedance amplifier has a gain of 10 MΩ. The purpose of the main amplifier is interfacing with the analog-digital converter used. The main amplifier has a gain of 2. Figure 6.8 shows the organization of the board-level components. The block in the middle is the custom electrode array chip. The read-channels receive the current and voltage signals from the 280-pin package on the board for amperometric and voltammetric operations, respectively.

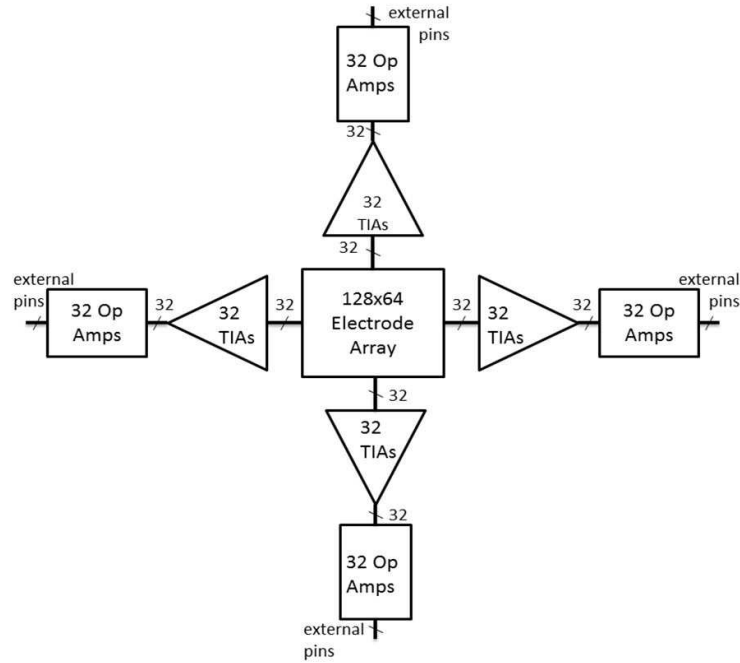


Figure 6.8: Main board-level components.

The circuit board is manufactured by Advanced Circuits Inc. with 4 layers of signals routing. In addition to 128 read-channels, the circuit board also contains voltage regulators, control logic for the custom electrode array chip and for the data acquisition board on the host computer. Figure 6.9 shows the circuit board for the 8,192-electrode array system. The 128-channel output from the circuit board is sampled by a data acquisition board through a host PC. The data acquisition board that works with the electrode array circuit board is an ADLink 2200 series 64-/96-CH high performance multi-function data acquisition card. Data acquisition from 128 data sources is triggered by the electrode array circuit board. A suite of MATLAB functions have been developed to provide interface between the electrode array chip, the on-board read-channels, and the data acquisition board inside the host PC. Custom signal processing functions were also developed in MATLAB and C++ for generating electrochemical images from the raw data acquired by the system.



Figure 6.9: Circuit board with the electrode array chip in the middle and other supporting circuits around it.

For all experiments described here, a 100 Hz data collection rate was used for an active subarray, and subarrays were cycled at a switching rate of 1 Hz when applicable. The on-chip potentiostat was used to apply an oxidation potential of +0.6 V (vs. Pt) for norepinephrine detection and a custom MATLAB script was used to generate electrochemical heat map images and videos for all experiments.

Fabrication of Microfluidic Devices

Microfluidics were interfaced with the chip using a combination of soft lithography^{43, 44} and laser cutting.^{45, 46} Wafers and molds were coated with HMDS and baked at 115 °C for 15 min for easy removal of the PDMS. All microfluidics were fabricated using two layers of PDMS. The bottom layer, which interfaces directly with the CMOS chip, was a 2-mm thick layer of a degassed 30:1 mixture of PDMS oligomer and cross-linker. This PDMS formulation gave higher adhesion to the CMOS chip, allowing for higher flow rates without leakage. After curing the first layer, a 3-mm thick layer of a degassed 10:1 mixture of PDMS oligomer and cross-linker was poured directly on top of the first layer and cured at 80 °C. This second layer was included to improve the structural integrity of the fluidics and to prevent adhesion to the poly(methyl methacrylate) (PMMA) compression plate described below. Wells used to contain samples over

the electrode array were fabricated by making these two layers on a pristine silicon wafer (Silicon Inc., Boise, ID, US). A biopsy punch (Robbins Instruments, Inc., Chatham, NJ, US) was used to create a 10-mm diameter well in the PDMS.

A Y-shaped microfluidic flow channel was fabricated using soft lithography.^{43, 44} SU-8 2075 was spin coated onto a 10-cm diameter silicon wafer to achieve a final feature height of $104 \pm 1 \mu\text{m}$ ($n = 7$) as measured by optical profilometry. A Y-shaped microfluidic channel 2.5 mm wide and 7 mm long, with entrance channels 1.75 mm wide and 4.5 mm long was used. PDMS was poured and cured as described above to make the device. A biopsy punch was used to create 1-mm diameter inlets and outlets to interface the device with vinyl PVC tubing (1/32" ID, 3/32" OD, Thermo Fisher Scientific, Waltham, MA, US), stainless steel connectors (Loctite, Henkel Corporation, Westlake, OH, US), and NE-1000 Single Syringe Pumps (New Era Pump Systems, Farmingdale, NY, US) for fluid control.

A second microfluidic device was fabricated to allow fluid transfer across the array *via* head pressure and consisted of two reservoirs connected by a straight channel. Standard photolithography was performed using SU-8 2075 to generate a mold for a microfluidic channel with dimensions $82 \mu\text{m} \times 2.5 \text{ mm} \times 6.0 \text{ mm}$. The mold was treated with HMDS, and two layers of PDMS were created as described above. A 5-mm diameter reservoir was punched at both channel ends using a biopsy punch.

A poly(methyl methacrylate) (PMMA) compression manifold was used to prevent fluid leaks from the Y-channel at high flow rates by applying additional pressure to the PDMS on the CMOS chip surface. The plate was cut from 1/8-in thick PMMA (Fort Collins Plastics, CO, US) using a CO₂ laser engraving system (30 W Epilog, Golden, CO, US). The plate contained 3-mm diameter holes for access to the inlets and outlet of the channel, a space for the arm of the socket used to interface the silicon chip with the printed circuit board (Textool™ Burn-In Grid ZIP Socket, 3M, Saint Paul, MN, US), and holes to attach the plate to the printed circuit board.

Nylon screws (1.5 in) and wing nuts were used to hold the plate in place and increase the amount of pressure applied to the PDMS. An image of the setup can be seen in Figure 6.10.

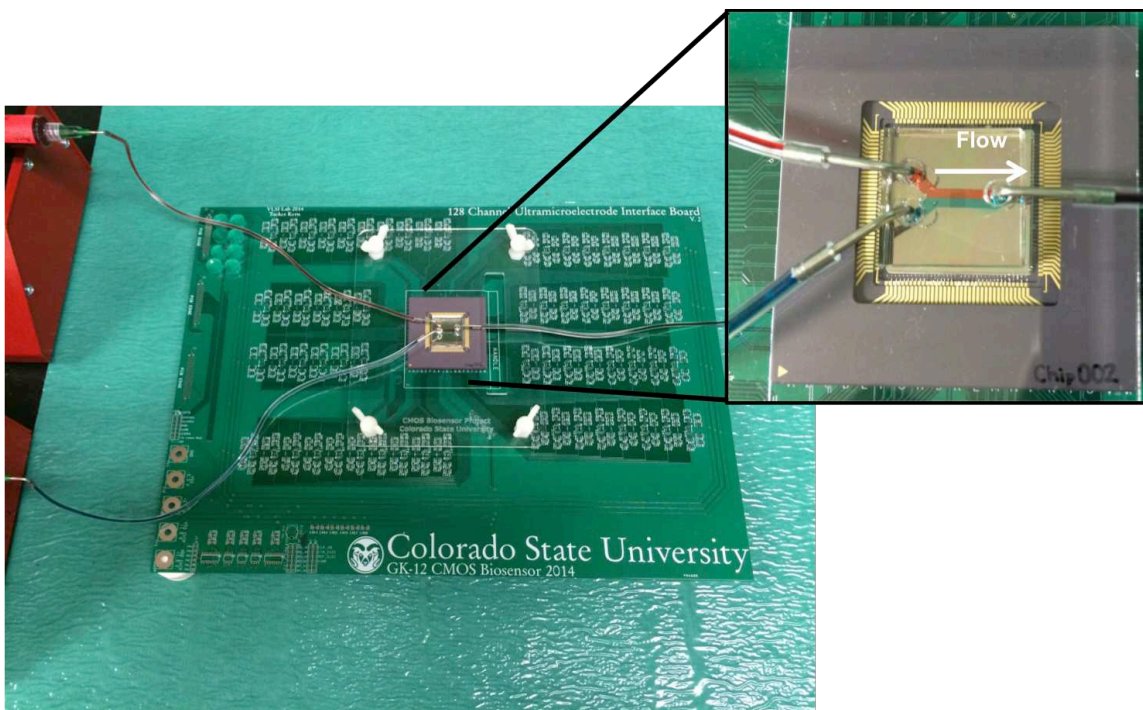


Figure 6.10: Setup for microfluidic experiments. The syringe pumps at the left pump two different fluids into the Y-shaped microfluidic channel positioned across the chip (inset image). The chip is connected to the PCB, and the microfluidics are compressed onto the chip using a custom-cut PMMA plate with nylon screws.

Diffusion of Norepinephrine Across a Subarray

Electrochemical detection of norepinephrine with spatial and temporal resolution was studied using a single subarray (96 of 128 electrodes). A 10-mm diameter well was placed on the CMOS chip with the array positioned in the lower right region of the well and 200 μL of media was added to well. MATLAB was used to monitor a single subarray throughout the entire experiment. A 10- μL drop of 100 mM norepinephrine in media was added to the top left region of the well, resulting in a final norepinephrine concentration of 4.8 mM after complete diffusion. The current resulting from the oxidation of norepinephrine was collected on the subarray as the solution travelled throughout the well.

Norepinephrine Diffusion Across Array

The spatial and temporal resolution of the array was next studied by monitoring slow fluid transport controlled by head pressure and diffusion. Media and a norepinephrine solution were prepared with dye for visualization. Blue media was used as a baseline and red media was used to indicate the presence of norepinephrine in the media. The flow of media containing norepinephrine was controlled by the relative head pressure in each reservoir. First, 20 μL of media was added to one reservoir to fill the flow channel with media and establish a baseline. Next, 19 μL of 10 mM norepinephrine was added to the second reservoir, and additional 0.5- μL aliquots of 10 mM norepinephrine were added to the second reservoir until the head pressure increased enough to begin to push the norepinephrine into the connecting channel. Head pressure and diffusion then slowly drove norepinephrine across the array and the resulting current was monitored across the array.

Bimodal Distribution of Norepinephrine Across the Array

Electrochemical images of controlled chemical distributions were generated by using a Y-shaped microfluidic channel on the CMOS chip to produce a bimodal gradient of norepinephrine across the array. Media and a norepinephrine solution were prepared with dyes as described above. Fluid control was achieved using two syringe pumps. Baseline signals were collected by flowing media across the array at 100 $\mu\text{L min}^{-1}$. The syringe pump containing the 10 mM norepinephrine solution was then started at 50 $\mu\text{L min}^{-1}$ while the media was simultaneously decreased to a flow rate of 50 $\mu\text{L min}^{-1}$ to maintain a total flow rate of 100 $\mu\text{L min}^{-1}$ generating a bimodal norepinephrine gradient across the array.

A similar experiment was carried out to position the bimodal gradient over different portions of the array. After flowing media at 100 $\mu\text{L min}^{-1}$ to establish a baseline, the flow rates were adjusted to have the 10 mM norepinephrine solution sequentially contribute to 25, 50, 75, and 100% of the total 100 $\mu\text{L min}^{-1}$ flow rate, cycling through the entire array at least once

between each change in flow rate. Video of the flow was taken using a commercial smartphone to compare to the electrochemical heat maps.

Results and Discussion

The high-density Pt microelectrode array described here was designed as a platform for imaging chemical distributions with high spatiotemporal resolution. Unlike previous examples of electrode-based imaging arrays, amperometric current was measured (as opposed to impedance) using an on-chip potentiostat. Electrode spacing in a high-density array determines the spatial resolution of the system and on-board electronics control the temporal resolution. Chemical distributions were controlled across the array using simple microfluidics to generate electrochemical images for demonstration of the spatiotemporal capabilities of the array. Variability among electrodes has been observed, and experiments are underway to understand the cause of variation in sensitivity. Slight differences in the electrodes, such as raised edges or small changes in surface area may be resulting in significant differences in signal. The short-term solution employed here is the use of standards, and a thorough investigation of electrode variability will be performed prior to using this platform for quantitative spatiotemporal imaging of chemical release from live tissue.

Diffusion of Norepinephrine Across a Subarray

A norepinephrine gradient was generated by diffusion across the CMOS array to study the temporal resolution of a single subarray. Current was monitored at 96 electrodes on the subarray and was plotted as a function of time for three representative electrodes in different locations on the subarray (Figure 6.11A). Still images from the resulting electrochemical video are shown in Figure 6.11B, demonstrating the progression of norepinephrine transport across the subarray.

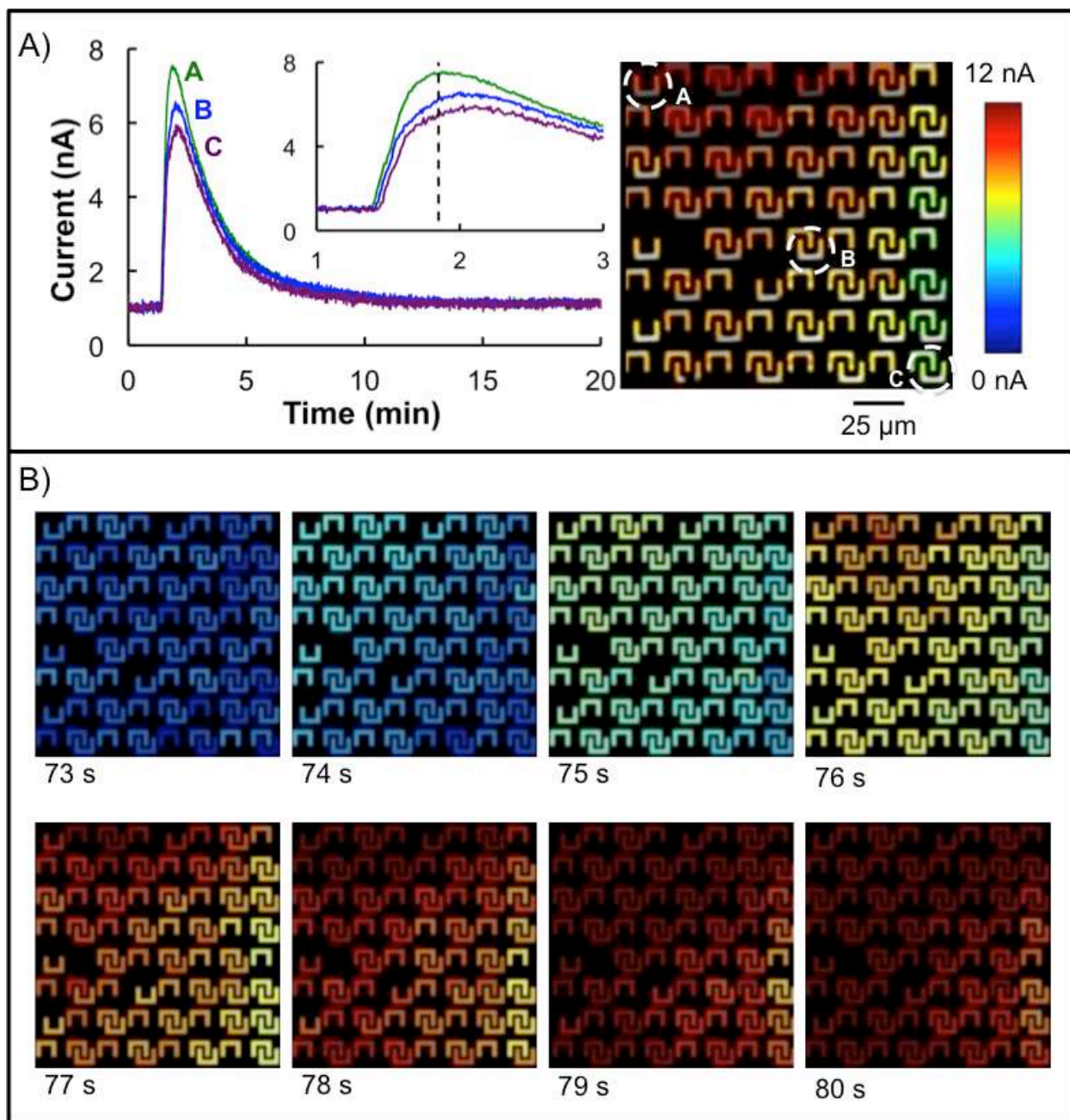


Figure 6.11: A) Diffusion of norepinephrine across a subarray. **Left)** Amperograms correspond to electrodes indicated on the heat map on the right. Electrodes closest to the source of the norepinephrine reach the highest signal, and all electrodes end at the same signal after the norepinephrine has completely diffused. The closest electrodes also detect an increase in signal prior to those located across the subarray. Inset is an expanded view of the peak region showing the difference in both current and timing of the maximum. **Right)** A still image of the heat map was taken at the time indicated by the vertical dashed line on the inset plot. Oxidation potential of +0.6 V (vs. Pt). Data collection rate 100 Hz for all electrodes on subarray. **B)** Still frames of electrochemical heat maps taken in 1 s increments from the electrochemical video.

Due to the limitation of I/Os on the data acquisition system connected to the host computer, a maximum of 96 channels are available, allowing 96 out of 128 to be monitored at any given time. The next generation of the chip will have the ability to read all 128 electrodes through the expanded I/Os on a new data acquisition system on the host computer, eliminating this limitation. A current increase was observed as norepinephrine reached each electrode, with a 6.5, 5.6, and 4.9 nA increase relative to the baseline current occurring at the first exposed electrode, the electrode in the center of the subarray, and the last exposed electrode, respectively. The sequential decrease in signal across the array was a result of norepinephrine dilution throughout the diffusion process. After the 10- μ L drop of 100 mM norepinephrine completely diffused into the media contained in the well, the norepinephrine reached a homogenous concentration of 4.8 mM, and the current of all electrodes equalized at 0.15 ± 0.08 nA ($n = 96$) greater than the media baseline. With a 10-ms time resolution for sampling, capture of the diffusion process is straightforward. The norepinephrine travelled across the diagonal of the subarray in 12 s, which is faster than pure diffusion (predicted to be 113 s),⁴⁷ likely due to advective flow caused by the addition of the norepinephrine solution with a pipette. Monitoring the norepinephrine transport across a $250 \mu\text{m} \times 250 \mu\text{m}$ subarray demonstrates that the spatial resolution of $30 \mu\text{m}$, dictated by the electrode spacing, and the 10-ms time resolution, determined by the data collection frequency, allow the system to be used for imaging. Methods utilizing thorough mixing or microfluidic devices are currently being investigated to provide standardized calibration strategies that are independent of diffusion time or the technique of solution addition *via* pipette.

Norepinephrine Diffusion Across the Array

The spatiotemporal resolution of the full array was studied by monitoring fluid transport controlled by combined head pressure and diffusion. A norepinephrine solution containing dye was used to correlate electrochemical images of norepinephrine with optical images of dye

during transport across the array. Representative still images from the electrochemical video can be seen in Figure 6.12. A baseline signal ($t = 64$ s) was collected for approximately one minute before the norepinephrine reached the array. By $t = 192$ s, the difference in head pressure between the reservoirs drove the norepinephrine over approximately the first half of the array, with diffusion generating a concentration gradient observed in both the electrochemical heat map and the optical images. Averaging the signal from all electrodes resulted in 1.3 nA distributed across the array as shown in the electrochemical heat map. After additional fluid transport across the array ($t = 384$ s), the average signal increased to 5.3 nA with the spatial distribution displayed in the electrochemical heat map. These results demonstrate that the array, which is of suitable size for chemically imaging cells in tissue slices, is capable of achieving high spatiotemporal resolution for the detection of electrochemically active species.

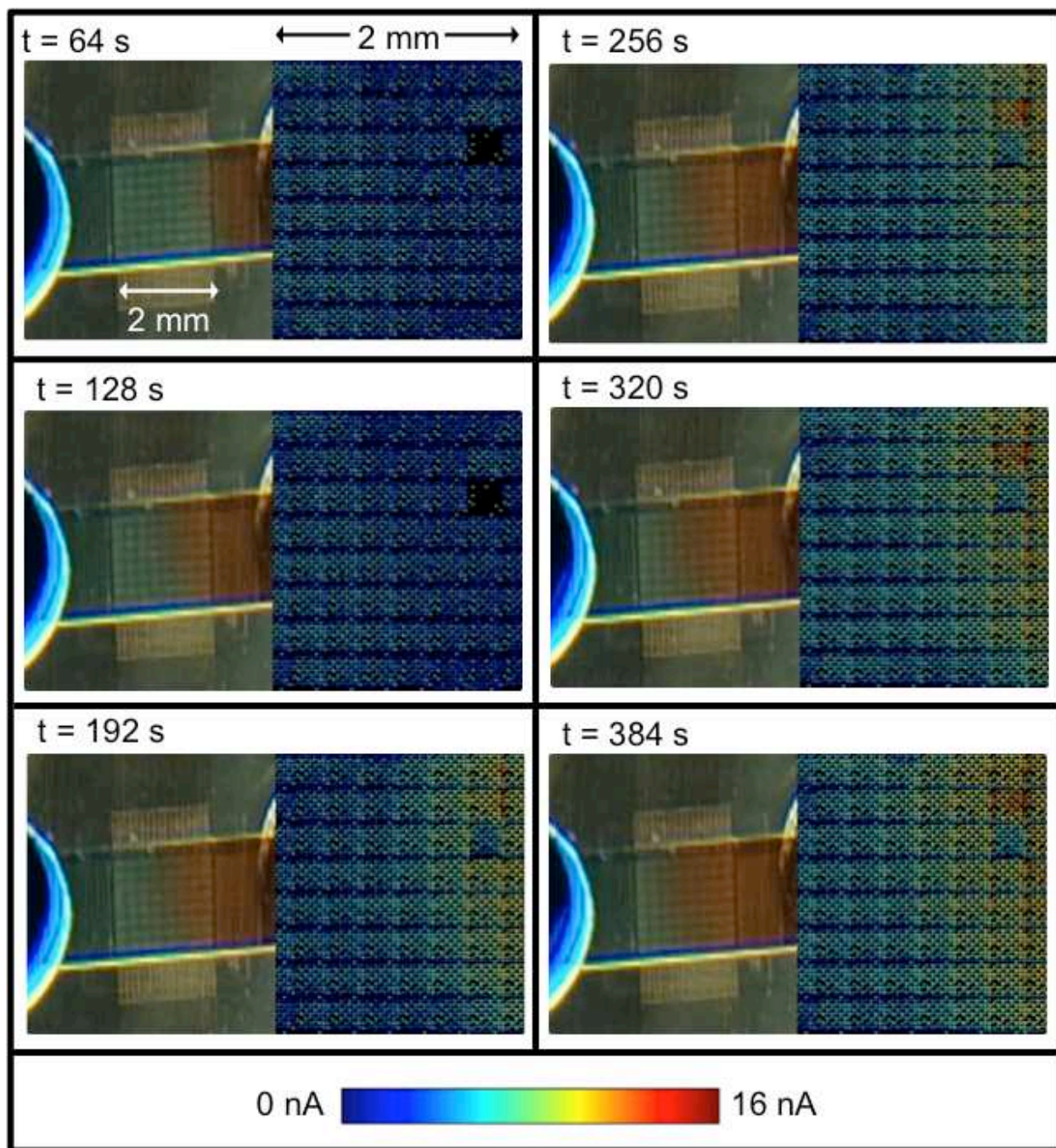


Figure 6.12: Diffusion of norepinephrine across the array. Optical images and electrochemical heat maps were recorded at the times indicated. Solutions contain dye for visualization. Red solution contains norepinephrine dissolved in neurobasal media, and blue solution is only neurobasal media. Oxidation potential of +0.6 V (vs. Pt). Data collection rate 100 Hz for all electrodes on active subarray. Switching rate between subarrays 1 Hz.

Bimodal Distribution of Norepinephrine

A bimodal gradient of norepinephrine was generated to electrochemically image a controlled chemical distribution over the electrode array. A Y-shaped microfluidic channel was used to direct 10 mM norepinephrine over approximately half of the array while the remaining portion of the array was exposed to media without norepinephrine. A representative electrochemical heat map and corresponding video frame is shown in Figure 6.13. A signal gradient was observed across each individual subarray, with the highest signal (44 ± 4 nA) on the left-most column, and lowest signal (23 ± 7 nA) to the right. The current decrease is the result of analyte depletion from upstream electrodes as the norepinephrine flowed from left to right. This phenomenon was not observed across the array as a whole because the on-chip potentiostat cycled through each subarray at a rate of 1 Hz and the linear flow velocity (6.4 mm s^{-1}) was great enough that the solution was refreshed prior to cycling neighboring horizontal subarrays. The vertical position of the interface between the media and the norepinephrine was observed in the heat map to fluctuate by $<250 \text{ }\mu\text{m}$ with each column of subarrays. The position changed in the 8 s required to cycle to neighboring subarrays due to imperfect fluid control by the syringe pumps.

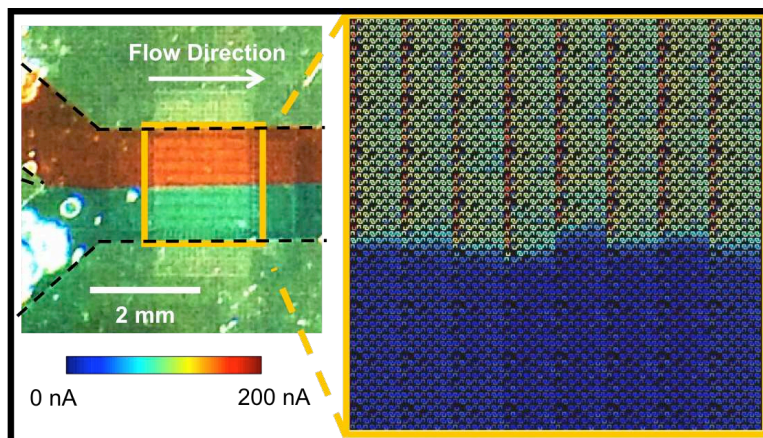


Figure 6.13: Optical image of bimodal gradient over the 2 mm × 2 mm microelectrode array and corresponding electrochemical heat map. Solutions contain dye for visualization. Red solution contains norepinephrine dissolved in neurobasal media, and blue solution is only neurobasal media. Dashed black lines indicate walls of microfluidic channel. Signal gradient across individual subarrays is due to analyte depletion by upstream electrodes. Oxidation potential of +0.6 V (vs. Pt). Data collection rate 100 Hz for all electrodes on active subarray. Switching rate between subarrays 1 Hz.

Control of the interface position was achieved by adjusting volumetric flow rates on the corresponding syringe pumps to demonstrate the spatiotemporal resolution capabilities of the system. Representative heat maps from still images of the electrochemical video at each interface position can be in Figure 6.14A.

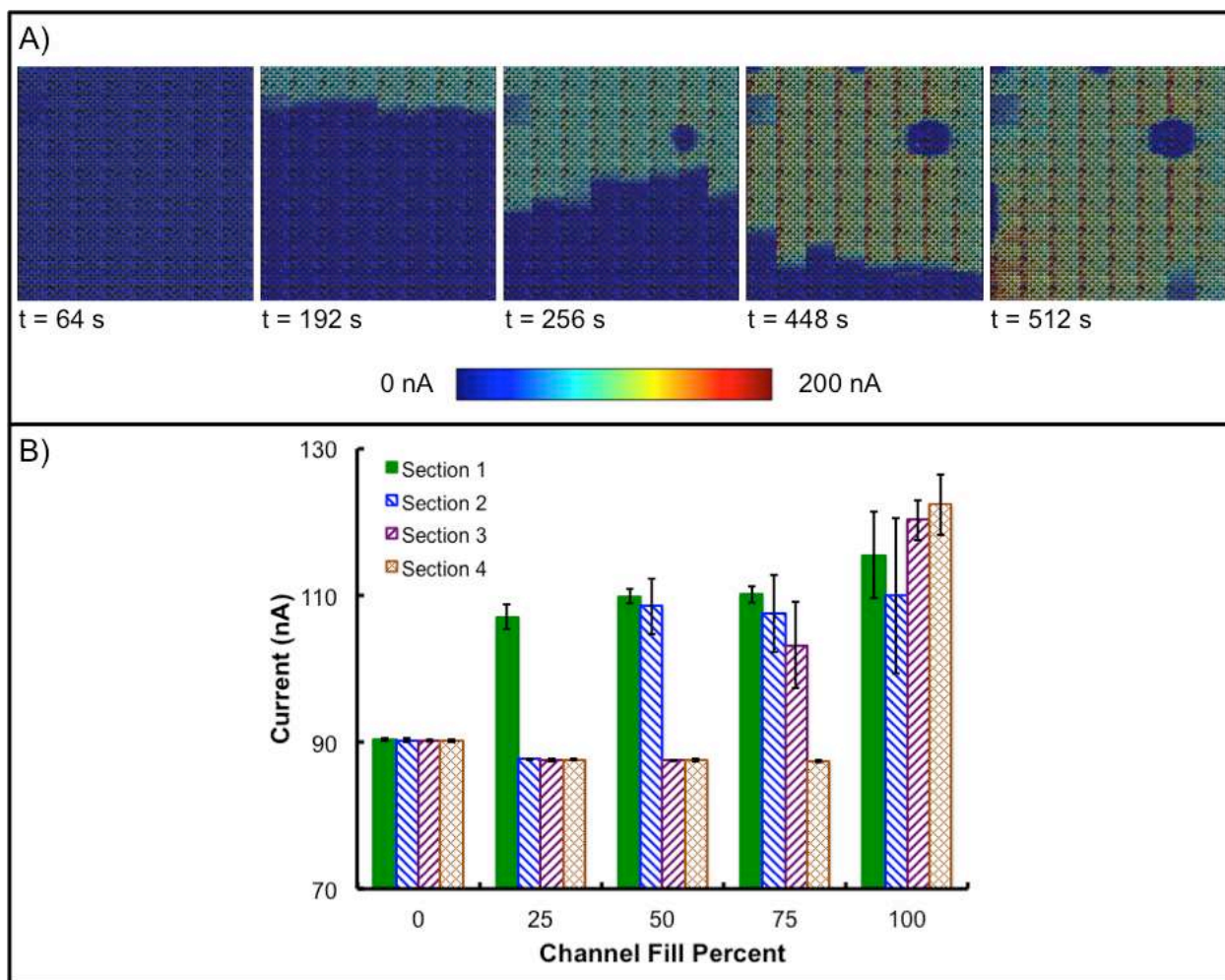


Figure 6.14: A) Still frames from electrochemical heat map video corresponding to each position of the bimodal gradient across the electrode array. **B)** Average signal for rows of subarrays when a bimodal gradient of norepinephrine is generated over different sections of the array. Error bars represent signal standard deviation across the row of subarrays ($n = 8$). For simplicity, all signals were normalized to the maximum signal detected during the experiment. Signals plotted correspond to the frames shown in A. In each x-axis category, the position of the data bar corresponds to the row of subarrays analyzed. Oxidation potential of +0.6 V (vs. Pt). Data collection rate 100 Hz for all electrodes on active subarray. Switching rate between subarrays 1 Hz.

For quantitative visualization, the signals were plotted as the average current from all electrodes in a horizontal row of eight subarrays representative of each of four sections of the array, with the error bars representing the standard deviation between the subarrays in the row. Each section of the array consists of two rows of subarrays, with Sections 1-4 ordered sequentially from the top of the array to the bottom. The plotted signals were taken after cycling

through all 64 subarrays prior to starting the following cycle. A current increase of 23 ± 6 nA was observed to occur on the sections of the array exposed to norepinephrine and the timing correlated with the video. A bubble can be seen in Section 2 in the heat maps in Figure 6.14 when norepinephrine fills at least 50% of the channel, which can be correlated with the electrochemical video. The bubble prevented norepinephrine from reaching the surface of the electrodes, decreasing the average signal (110 nA compared to 120 nA) and resulting in a high standard deviation in signal (5-10% RSD) for the row of subarrays. Bubbles would be problematic when imaging live tissue with this platform, so the design of the microfluidic device will be modified to control bubble formation and provide a method to interface live tissue slices with the electrode array. Monitoring the controlled distributions of norepinephrine and media in space and time demonstrates the ability of the electrode array to generate electrochemical images of gradients and correlate them to optical images with high spatiotemporal resolution, which could provide the ability to image neurotransmitter release from a tissue slice with cellular resolution, elucidating the effects of molecular gradients on cell-to-cell communication and other biological processes.

Conclusions

High-density electrode arrays containing large numbers of electrodes have primarily been used for impedance or voltage-based sensing with limited utilization of amperometric detection. The system described here was designed to augment traditional microscopy methods, offers an additional tool for imaging chemical distributions in biological systems, and has been used to electrochemically image distributions of norepinephrine standard solutions as a model neurotransmitter. The microelectrode array described is composed of 8,192 platinum working electrodes in a 2 mm \times 2 mm area. PDMS microfluidics provided fluid control over the array to image distributions of norepinephrine. The density of the electrode array provided 30- μ m spatial resolution, while the on-chip potentiostat and on-board electronics allowed

norepinephrine detection with a maximum temporal resolution of 10 ms, as demonstrated by monitoring diffusion of norepinephrine across a single subarray. A larger area of 2 mm × 2 mm could be monitored by switching through subarrays at a rate of 1 Hz. This electrochemical imaging system will be implemented in the future for monitoring chemicals released from live tissue slices with 30 μm spatial resolution. This system has the potential to elucidate the effects of chemical gradients on biological processes such as chemotaxis, cancer metastasis, and directed cell migration.

This work is supported in part by National Science Foundation Grant No. GDE-0841259. The silicon-based microelectrode chip was manufactured by Avago Technologies. Their technical assistance and generous support for this project are greatly appreciated.

REFERENCES

1. J. B. Wydallis, R. M. Feeny, W. Wilson, T. Kern, T. Chen, S. Tobet, M. M. Reynolds and C. S. Henry, *Lab on a Chip*, 2015, **15**, 4075-4082.
2. B. J. Kim and M. M. Wu, *Annals of Biomedical Engineering*, 2012, **40**, 1316-1327.
3. R. A. Firtel and C. Y. Chung, *Bioessays*, 2000, **22**, 603-615.
4. W. J. Rosoff, J. S. Urbach, M. A. Esrick, R. G. McAllister, L. J. Richards and G. J. Goodhill, *Nature Neuroscience*, 2004, **7**, 678-682.
5. S. D. Nathanson, *Cancer*, 2003, **98**, 413-423.
6. B. Brucher and I. S. Jamall, *Cellular Physiology and Biochemistry*, 2014, **34**, 213-243.
7. N. C. Guerineau and M. G. Desarmenien, *Cellular and Molecular Neurobiology*, 2010, **30**, 1425-1431.
8. S. C. Ge, S. Koseoglu and C. L. Haynes, *Analytical and Bioanalytical Chemistry*, 2010, **397**, 3281-3304.
9. K. T. Schomacker, J. K. Frisoli, C. C. Compton, T. J. Flotte, J. M. Richter, N. S. Nishioka and T. F. Deutsch, *Lasers in Surgery and Medicine*, 1992, **12**, 63-78.
10. W. R. Zipfel, R. M. Williams, R. Christie, A. Y. Nikitin, B. T. Hyman and W. W. Webb, *Proceedings of the National Academy of Sciences of the United States of America*, 2003, **100**, 7075-7080.
11. Y. Amoh, K. Katsuoka and R. M. Hoffman, *Current Pharmaceutical Design*, 2008, **14**, 3810-3819.
12. C. Kobbert, R. Apps, I. Bechmann, J. L. Lanciego, J. Mey and S. Thanos, *Progress in Neurobiology*, 2000, **62**, 327-351.
13. L. J. Kricka and P. Fortina, *Clinical Chemistry*, 2009, **55**, 670-683.
14. R. M. Caprioli, T. B. Farmer and J. Gile, *Analytical Chemistry*, 1997, **69**, 4751-4760.
15. A. C. Grey, A. K. Gelasco, J. Section, R. A. Moreno-Rodriguez, E. L. Krug and K. L. Schey, *Anatomical Record-Advances in Integrative Anatomy and Evolutionary Biology*, 2010, **293**, 821-828.
16. A. J. Wain, *Electrochemistry Communications*, 2014, **46**, 9-12.
17. S. Amemiya, J. D. Guo, H. Xiong and D. A. Gross, *Analytical and Bioanalytical Chemistry*, 2006, **386**, 458-471.
18. S. Bergner, P. Vatsyayan and F. M. Matysik, *Analytica Chimica Acta*, 2013, **775**, 1-13.
19. A. Selimovic, J. L. Erkal, D. M. Spence and R. S. Martin, *Analyst*, 2014, **139**, 5686-5694.

20. M. M. Mensack, J. B. Wydallis, N. S. Lynn, D. S. Dandy and C. S. Henry, *Lab on a Chip*, 2013, **13**, 208-211.
21. B. N. Kim, A. D. Herbst, S. J. Kim, B. A. Minch and M. Lindau, *Biosensors & Bioelectronics*, 2013, **41**, 736-744.
22. B. Zhang, M. Heien, M. F. Santillo, L. Mellander and A. G. Ewing, *Analytical Chemistry*, 2011, **83**, 571-577.
23. J. Wang, R. Trouillon, J. Dunevall and A. G. Ewing, *Analytical Chemistry*, 2014, **86**, 4515-4520.
24. D. J. Bakkum, U. Frey, M. Radivojevic, T. L. Russell, J. Muller, M. Fiscella, H. Takahashi and A. Hierlemann, *Nature Communications*, 2013, **4**, 12.
25. M. Sen, K. Ino, K. Y. Inoue, T. Arai, T. Nishijo, A. Suda, R. Kunikata, H. Shiku and T. Matsue, *Biosensors & Bioelectronics*, 2013, **48**, 12-18.
26. F. Heer, W. Franks, A. Blau, S. Taschini, C. Ziegler, A. Hierlemann and H. Baltes, *Biosensors & Bioelectronics*, 2004, **20**, 358-366.
27. S. Hafizovic, F. Heer, T. Ugniwenko, U. Frey, A. Blau, C. Ziegler and A. Hierlemann, *Journal of Neuroscience Methods*, 2007, **164**, 93-106.
28. U. Frey, U. Egert, F. Heer, S. Hafizovic and A. Hierlemann, *Biosensors & Bioelectronics*, 2009, **24**, 2191-2198.
29. K. Ino, W. Saito, M. Koide, T. Umemura, H. Shiku and T. Matsue, *Lab on a Chip*, 2011, **11**, 385-388.
30. T. Matsue, *Analytical Sciences*, 2013, **29**, 171-179.
31. J. Rothe, O. Frey, A. Stettler, Y. H. Chen and A. Hierlemann, *Analytical Chemistry*, 2014, **86**, 6425-6432.
32. I. A. Ges, R. L. Brindley, K. P. M. Currie and F. J. Baudenbacher, *Lab on a Chip*, 2013, **13**, 4663-4673.
33. J. Wang, R. Trouillon, Y. Q. Lin, M. I. Svensson and A. G. Ewing, *Analytical Chemistry*, 2013, **85**, 5600-5608.
34. M. K. Zhao, H. Wi, E. J. Lee, E. J. Woo and T. I. Oh, *Physics in Medicine and Biology*, 2014, **59**, 5831-5847.
35. W. Cunningham, K. Mathieson, F. A. McEwan, A. Blue, R. McGeachy, J. A. McLeod, C. Morris-Ellis, V. O'Shea, K. M. Smith, A. Litke and M. Rahman, *Journal of Physics D-Applied Physics*, 2001, **34**, 2804-2809.
36. E. Ferrea, A. Maccione, L. Medrihan, T. Nieuw, D. Ghezzi, P. Baldelli, F. Benfenati and L. Berdondini, *Frontiers in Neural Circuits*, 2012, **6**, 14.
37. S. R. I. Gabran, M. T. Salam, J. Dian, Y. El-Hayek, J. L. P. Velazquez, R. Genov, P. L. Carlen, M. M. A. Salama and R. R. Mansour, *Ieee Transactions on Neural Systems and Rehabilitation Engineering*, 2014, **22**, 1072-1082.

38. L. J. Johnson, E. Cohen, D. Ilg, R. Klein, P. Skeath and D. A. Scribner, *Journal of Neuroscience Methods*, 2012, **205**, 223-232.
39. D. Jackel, U. Frey, M. Fiscella, F. Franke and A. Hierlemann, *Journal of Neurophysiology*, 2012, **108**, 334-348.
40. W. Pettine, M. Jibson, T. Chen, S. Tobet, P. Nikkel and C. S. Henry, *Ieee Sensors Journal*, 2012, **12**, 1187-1192.
41. R. M. Feeny, J. B. Wydallis, T. Chen, S. Tobet, M. M. Reynolds and C. S. Henry, *Electroanalysis*, 2014, **26**.
42. M. Duwe, T. Chen and Ieee, Seoul, SOUTH KOREA, 2011.
43. D. C. Duffy, J. C. McDonald, O. J. A. Schueller and G. M. Whitesides, *Analytical Chemistry*, 1998, **70**, 4974-4984.
44. Y. Sameenoi, M. M. Mensack, K. Boonsong, R. Ewing, W. Dungchai, O. Chailapakul, D. M. Crokek and C. S. Henry, *Analyst*, 2011, **136**, 3177-3184.
45. J. P. Davim, C. Oliveira, N. Barricas and M. Conceicao, *International Journal of Advanced Manufacturing Technology*, 2008, **35**, 875-879.
46. I. A. Choudhury and S. Shirley, *Optics and Laser Technology*, 2010, **42**, 503-508.
47. M. Ansari, S. Kazemi, M. A. Khalilzadeh, H. Karimi-Maleh and M. B. P. Zanousi, *International Journal of Electrochemical Science*, 2013, **8**, 1938-1948.

CHAPTER 7. ELECTROCHEMICAL SPATIOTEMPORAL IMAGING OF NEUROTRANSMITTER RELEASE FROM LIVE ADRENAL TISSUE USING A HIGH-DENSITY ELECTRODE ARRAY WITH AMPEROMETRIC DETECTION

A high-density platinum electrode array designed for amperometric imaging of biomarker release from live tissue slices with spatiotemporal resolution is reported. The spatial resolution, dictated by electrode spacing, was 30 μm , and the temporal resolution, limited by the time required to collect a full image of the electrode array, was 32 s. Live murine adrenal slices were interfaced directly with the 2 mm \times 2 mm array, which was of adequate size to generate electrochemical images of the entire tissue slice. Custom microfluidic devices were designed to provide controlled stimulant delivery to the adrenal tissue and contain fluid on the electrode array. Amperometric detection was accomplished using an on-chip potentiostat, which allowed monitoring of 64 pairs (of the 8,192 total number of electrodes) of shorted electrodes simultaneously. Cycling between 64 subarrays of these electrode pairs allowed the entire electrode array area to be imaged in 32 s, where each image contained 4,096 “pixels”. The electrochemical imaging platform was specifically designed to be interfaced with an upright microscope to provide simultaneous electrochemical and optical imaging capabilities, which provided simple spatiotemporal correlation of stimulant delivery with the physical location of the tissue on the electrode array, and could greatly expand the library of accessible biomarkers when imaging live tissue slices. Information gained from the electrochemical imaging platform described here can elucidate mechanisms of cellular communication on the organ scale, providing better understanding of disease progression, such as cancer metastasis and Alzheimer’s development. This work is unpublished, and will be submitted for publication after completion of further experiments. The data reported here represent the culmination of the electrochemical imaging project based on the device development presented in preceding chapters. Microfluidic design and fabrication, electrochemical experimentation, and data interpretation were primarily accomplished by Rachel Feeny. William Tedjo and Jasmine Nejad

developed the MATLAB scripts used for data collection and analysis, developed the supporting electronics, and aided in experimental design and execution. A manuscript describing this work is in preparation and will be submitted to *Lab on a Chip*.

Introduction

Chemical gradients have been theorized and shown to drive a multitude of biological processes including cellular communication and movement.¹⁻³ The ability to image chemical gradients and correlate them to their respective biological phenomena is critical for elucidating the driving forces behind disease progression, such as Alzheimer's development and cancer metastasis.^{4, 5} To understand how chemical gradients drive biological processes, an imaging platform must be developed capable of achieving high spatiotemporal resolution with sensitivity and selectivity for the biomarkers of interest. The most common method used for this type of imaging is fluorescence microscopy, which is a sensitive and selective technique capable of generating images with spatiotemporal resolution.⁶⁻¹⁰ Fluorescence microscopy, however, is limited to a target library of natively fluorescent species and those modified with fluorescent probes. The ability to expand this library to a wider range of biomarkers *via* electrochemical methods would enhance understanding of the role of chemical gradients in biological systems.

Mass spectrometry has been developed as an imaging method capable of achieving high selectivity for a large library of molecules.¹¹⁻¹³ Despite having excellent spatial resolution (~20 μm), this technique suffers from poor temporal resolution and is frequently limited to *ex vivo* tissue samples that are no longer viable at the time of analysis.^{14, 15} Though recent work has been reported using mass spectrometry to image live cells,¹⁶ the temporal resolution is inadequate when generating images on the scale of a tissue slice develop a model of changes in chemical gradients over time.

Electrochemistry offers an alternative imaging platform capable of detecting biomarkers inaccessible by traditional optical methods and provides spatiotemporal resolution with

quantitative information. Electrode arrays have been developed to generate electrochemical “heat maps” where each electrode represents a “pixel” in the image, and electrode spacing dictates the spatial resolution, while temporal resolution is controlled by the sampling rate. Large arrays (up to 81,920 electrodes)¹⁷ have been reported for imaging action potential across neuronal networks with high spatiotemporal resolution,¹⁷⁻²⁰ though they lack chemical selectivity. Other arrays use amperometric or voltammetric techniques to image systems with chemical selectivity at the scale of a single cell or cell-to-cell junction, but there have been few reports of systems capable of imaging chemical gradients from *ex vivo* murine tissue slices with spatiotemporal resolution.²¹⁻²³

Murine adrenal tissue slices present an ideal model system to demonstrate the function of an electrode array as an electrochemical imaging platform. Adrenal tissue has been extensively studied²⁴⁻²⁶ and has been reported to exhibit localized release of catecholamines from the medulla (center) of the slice upon stimulation with caffeine, while the cortex (edge) of the tissue shows no release.²⁷⁻³⁰ This release profile allows demonstration of the spatiotemporal resolution capabilities of the imaging platform with direct detection of neurotransmitters, avoiding the need for added complexity of chemical modification of the electrode array. Murine adrenal tissue is of adequate size to fit onto the electrode array and be contained within a microfluidic device.

The system described here was previously used to image norepinephrine distributions in microfluidic devices as a demonstration of its spatiotemporal resolution capabilities.³¹ The electrode array consisted of 8,192 individually addressable working electrodes in 2 mm × 2 mm and used amperometry to generate qualitative and quantitative electrochemical images with spatiotemporal resolution on the scale of an *ex vivo* murine tissue slice. Microfluidic devices were interfaced with the Si chip to achieve precise fluid delivery to the tissue. The entire system was designed to interface with an upright microscope to provide an imaging method complementary to optical microscopy, further expanding the library of accessible biomarkers to

elucidate the role of chemical gradients in biological systems. Simultaneous optical and electrochemical imaging of stimulated biomarker release from live adrenal slices was accomplished with high spatiotemporal resolution.

Experimental

Materials and Instrumentation

All reagents were of at least ACS grade and were used as received without further purification. All electrochemical experiments were performed in cell culture media (Neurobasal-A media without phenol red, Life Technologies Corporation, Carlsbad, CA, US). To maintain the media pH at 7.4, 4-(2-hydroxyethyl)-1-piperazineethanesulfonic acid (HEPES) was added to the cell culture media at a 20:1 ratio of media to HEPES. Caffeine (Mallinckrodt Pharmaceuticals, Dublin, Ireland) was used to stimulant catecholamine release from adrenal tissue slices at a concentration of 55 mM for all experiments. A small amount of food dye (Great Value, Bentonville, AR, US) was added to the media used to make the caffeine solutions to provide simultaneous optical imaging of stimulant delivery to the tissue slice. The electrode array and microfluidic devices were thoroughly rinsed between experiments with 18.2 M Ω •cm water from a MilliPore Milli-Q system (Billerica, MA, US).

Electrode Array and Supporting Electronics

The electrode array used in this work has been previously described.^{31, 32} Briefly, the array consisted of 64 subarrays, each containing 128 individual Pt working electrodes, with a shared Pt pseudo-reference electrode and auxiliary electrode. In total, the array contained 8,192 working electrodes in a 2 mm \times 2 mm area. An on-chip integrated potentiostat provided amperometric control. The silicon-based microchip was fabricated using complementary metal

oxide semiconductor (CMOS) methods standard to the microfabrication industry. The Pt-capped microelectrodes protruded 1.5 μm from the surface of the microchip.

Supporting electronics for the electrode array were incorporated using a printed circuit board. Current outputs from each of the 128 read channels from the microchip were converted using trans-impedance amplifiers. Additional electronics incorporated on the printed circuit board included single-ended operational amplifiers, high precision 50 M Ω thin-film resistors, and 1 nF stabilization feedback capacitors. Output from the read channels was shorted together for electrode pairs, which served to increase the electrode area and therefore increase electrochemical signal. This alteration also allows simultaneous use of all electrodes on each subarray as it circumvents the limitation of I/Os on the data acquisition system connected to the host computer, which provided a maximum of 96 available channels. While this change decreased the spatial resolution capabilities of the electrode array by a factor of two, the increase in signal and ability to image the entire array area were determined to be a beneficial tradeoff. The supporting electronics used in this platform allowed for theoretical sub-pA current detection limits.

Adrenal Tissue Slice Preparation

Adrenal tissue used for this work was collected from Thy-1 YFP transgenic mice of the C57 BL/6 background. The mice were deeply anesthetized and killed by cervical dislocation. Laparotomy was performed, and both adrenal glands were dissected free of surrounding fascia and removed from the mice. After dissection, the adrenal glands were immediately placed in ice-cold Krebs buffer and cleaned of any adherent fat. Adrenal glands were then submerged in low melting point agarose and placed in a 4 $^{\circ}\text{C}$ refrigerator for 4 min for agarose polymerization. A biopsy punch was used to cut the agarose surrounding the tissue to a diameter of 3 mm for convenient interfacing with the electrode array and microfluidic devices. The tissue was then sliced to 250 μm thick using a vibrating microtome and collected into hibernate media with

penicillin-streptomycin (PS), where it remained at 4 °C for 15 min. Finally, the hibernate media was replaced with adult neurobasal medium containing PS, B-27 supplement, and HEPES in a 37 °C, 5% CO₂ incubator overnight prior to electrochemical imaging experiments. This tissue slices were interfaced directly with the electrode array for electrochemical detection (Figure 7.1)

All experiments were carried out in accordance with the NIH Guide for the Care and Use of Laboratory Animals and approval of the Colorado State University Institutional Animal Care and Use Committee.

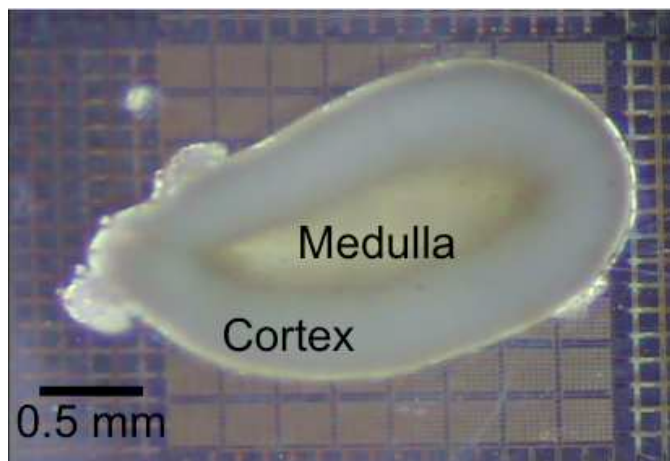


Figure 7.1: Photograph of live murine adrenal tissue slice on the high-density electrode array. Electrochemical images generated using the electrode array were correlated with optical images to determine location of biomarker release from the tissue.

Microfluidic Device Fabrication

Two types of devices were developed to accomplish fluid delivery to the tissue slice. Both were primarily fabricated from poly(dimethylsiloxane) (PDMS) (Sylgard 184, Dow Corning, Midland, MI, US). In both systems, two layers of PDMS were used, as previously reported.³¹ The bottom layer, which directly contacted the Si chip, was composed of degassed PDMS in a 30:1 ratio of oligomer to cross-linker to provide improved adhesion between the PDMS and the Si and prevent leaks. The upper layer was made of a degassed 10:1 mixture of PDMS oligomer and cross-linker, resulting in a more rigid polymer to provide structural integrity. Each PDMS

layer was poured onto a mold or Si wafer, as specified below, curing at 80 °C after pouring each layer.

The first device used in conjunction with the electrode array was a PDMS well designed to contain the live tissue slice and neurobasal media. The well contained a layer of nylon mesh to secure the tissue slice on the array and prevent movement during the experiment. To fabricate the well, the two layers of PDMS described above were poured onto a Si wafer (Silicon Inc., Boise, ID, US). A 15 mm × 15 mm square was cut from the PDMS, and the interior 8-mm-diameter reservoir and perpendicular 0.3-mm-diameter port in the wall of the PDMS well were punched using biopsy punches (Robbins Instruments, Inc., Chatham, NJ, US). To perform experiments, polyether ether ketone (PEEK) tubing (360 μm OD, 50 μm ID, IDEX Health and Science, Lake Forest, IL, US) was inserted into the port in the wall of the PDMS well as a method of stimulant delivery. A 3D schematic and photograph of the device is shown in Figure 7.2A.

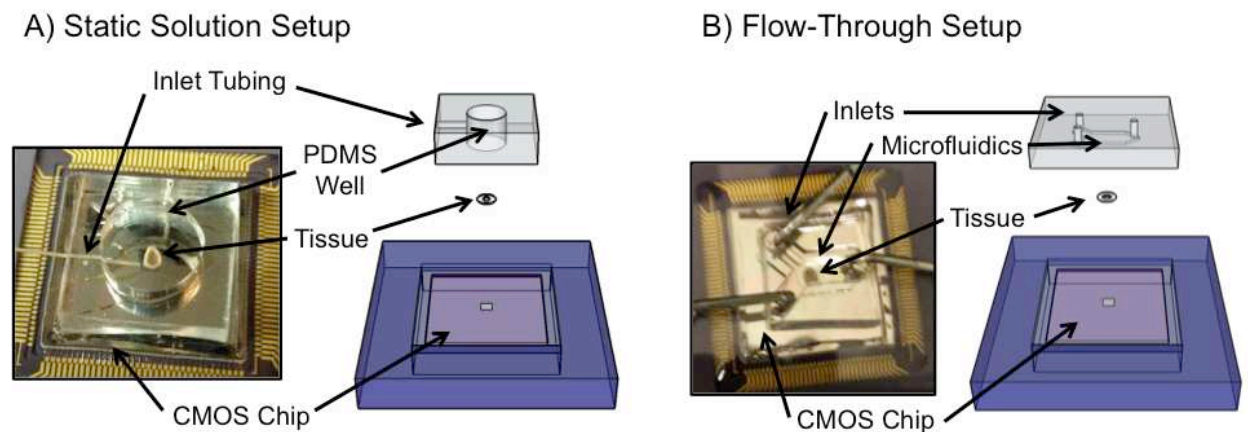


Figure 7.2: Images and schematics of PDMS devices and tissue slices interfaced with the CMOS chip. **A)** Static solution setup with a PDMS well and PEEK tubing. **B)** Y-shaped microfluidic channel for flow-through system.

To provide control of fluid delivery to the tissue slice on the electrode array, a microfluidic device was fabricated using the two layers of PDMS described above poured onto custom molds. The mold was fabricated using standard photolithography techniques. A silicon

wafer (Silicon, Inc., Boise, ID) was coated with SU-8 2150 (MicroChem, Westborough, MA, US) using a spin coater (WS-650MZ-23NPP/LITE, Laurell Technologies Corporation, North Wales, PA, US) to achieve a final feature height of 412 μm , as measured using a ZeScope optical profilometer (Zygo, Middlefield, CT). UV exposure with a UV lamp (OmniCure Series 2000, Lumen Dynamics, Mississauga, Ontario, Canada) was performed using a custom photomask (CAD/Art Services, Inc., Bandon, OR) to generate a mold for a Y-shaped channel with two inlets and one outlet. The main chamber of the channel was 4 mm wide and 6 mm long to accommodate the tissue slice and the electrode array. After generating the microfluidic device by soft lithography using the two layers of PDMS described above, the exterior PDMS was cut to 18 mm \times 18 mm to fit on the silicon microchip. A biopsy punch was used to create 1.5-mm-diameter inlet and outlet ports, which were interfaced with stainless steel connectors (Loctite, Henkel Corporation, Westlake, OH) and vinyl PVC tubing (1/32" ID, 3/32" OD, Thermo Fisher Scientific, Waltham, MA) to connect to syringes (10 mL, Benton, Dickinson and Company, Franklin Lakes, NJ, US) in NE-1000 Single Syringe Pumps (New Era Pump Systems, Farmingdale, NY) for fluid control. Figure 7.2B shows a 3D schematic and photograph of the microfluidic setup.

After experimentation with the PDMS well and microfluidic device described above, further improvements were implemented in the designs to more effectively secure the adrenal tissue in place throughout the course of the experiments. A layer of nylon mesh was added to the PDMS well to secure the tissue slice on the array and prevent movement during the experiment. A 200- μm -thick layer of 30:1 PDMS was cured on a Si wafer at 80 $^{\circ}\text{C}$. Once cured, a 6-mm-diameter biopsy punch was used to remove PDMS from the region that would become the well. Nylon mesh (Nitex, Genesee Scientific Corporation, San Diego, CA, US) was cut to 15 mm \times 15 mm using a laser engraving system (30 W Epilog, Golden, CO, US), was placed over the hole in the 200- μm -thick PDMS, and secured in place using a small amount of uncured

30:1 PDMS. The PDMS well composed of two layers described above was aligned on top of the nylon mesh. Curing the 30:1 PDMS at 80 °C resulted in a secure seal between layers. The 200- μm -thick PDMS was cut at the edges of the well and removed from the Si wafer. The perpendicular port in the wall of the PDMS well was punched to be 2 mm diameter to accommodate larger vinyl PVC tubing (1/32" ID, 3/32" OD, Thermo Fisher Scientific, Waltham, MA) for more straightforward stimulant delivery.

Securing the tissue in place in the flow-through microfluidic device was accomplished using a microfluidic channel with multiple heights. The lower regions of the channel held the agarose surrounding the tissue in place, while fluid flow was allowed through the taller regions of the channel. Due to requirements for the channel to be deep enough to contain the tissue slice while allowing fluid flow ($>250\ \mu\text{m}$), and complexity added to the fabrication process by multiple channel heights, the mold for the microfluidic device was constructed from layers of custom-cut plastic structures assembled on a plastic plate rather than by using standard photolithography techniques. The plastic structures were composed of pressure sensitive adhesive (PSA) (3M 468MP, 130 μm , Maplewood, MN, US) on overhead transparency film (100 μm thick, PP2200, 3M, Maplewood, MN, US) where each layer had a total thickness of 230 μm . The desired channel geometries were cut into the transparency/PSA using a laser engraving system. A 3.18 mm \times 25 mm \times 25 mm poly(methyl methacrylate) (PMMA) (Fort Collins Plastics, CO, US) plate was used as the base of the mold, and layers of the cut transparency/PSA were stacked in the center, using the PSA to secure each layer. Two layers were used to generate the mold; the first layer defined the total geometry of the channel and the second defined the deeper regions of the channel where fluid would flow, with the remaining areas shallower to secure the tissue. Molds for microfluidic devices were fabricated with two different geometries to fulfill two different purposes. The first provided stimulation of the entire adrenal slice by containing a 460- μm -deep, 2-mm-diameter region for fluid flow. The second allowed spatial control of fluid delivery to the tissue for precision in stimulation by limiting fluid

flow to a 1-mm-wide region of the channel. For both devices described, the channel length and width were 6 mm and 4 mm, respectively, to accommodate the tissue slice and fit on the surface of the Si chip. Two inlets were used for each device, one for media and the other for stimulant. After pouring and curing the two layers of PDMS as described above, a 1.5-mm-diameter biopsy punch was used to create inlet and outlet ports. Fluid control was again accomplished using syringe pumps and vinyl PVC tubing.

For all devices described, a custom PMMA compression plate was used to reversibly seal the PDMS to the surface of the Si chip to prevent fluid leaks, as previously reported.³¹ The plate was cut from 0.125-in-thick PMMA, and contained holes for access to the inlets and outlets of the microfluidic device and holes for nylon screws to secure the plate to the printed circuit board containing supporting electronics.

Interfacing with Upright Microscope

The electrode array and microfluidic system was interfaced with an upright microscope to provide simultaneous optical and electrochemical imaging of the adrenal tissue slices. The setup is shown in Figure 7.3. A custom stage was generated from laser-cut PMMA to support the printed circuit board and prevent flexing of the supporting electronics. The electrode array and microfluidic setup were positioned directly under the objective on an Olympus BX61WI microscope in a BX51/61WI enclosure (Olympus Corporation, Tokyo, Japan) for environmental control. Cables were fed from the printed circuit board through the environmental chamber to external power supplies and the computer for chip operation and data collection. All fluid control was accomplished from the exterior of the environmental chamber using syringes and tubing that reached the PDMS devices on the electrode array. Syringe pumps were placed outside of the chamber with tubing feeding into the chamber to deliver solutions to the tissue. During experiments, the temperature in the environmental chamber was held at 37 °C.

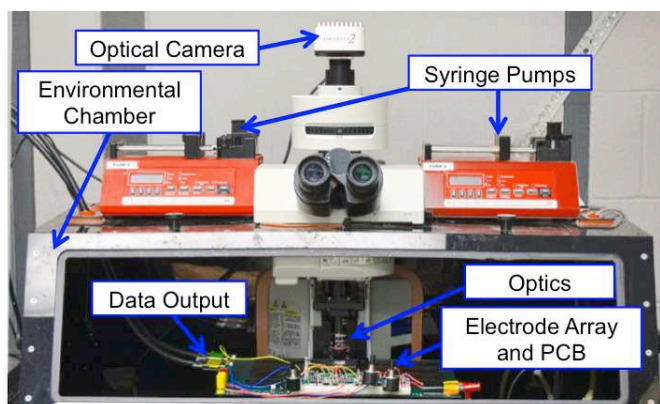


Figure 7.3: Photograph of the electrode array and supporting electronics interfacing with the upright microscope in the environmental chamber. Syringe pumps were placed outside of the chamber to allow fluid control without opening the chamber and disrupting temperature control.

Stimulation Procedures

Stimulation in Static Solution

The open PDMS well was used to deliver stimulant to live adrenal tissue slices in a static solution environment. One adrenal slice embedded in agarose was removed from the petri dish and carefully placed on the surface of the electrode array. The PDMS well was positioned around the tissue and secured in place using the PMMA compression plate. Next, 200 μL of neurobasal media was added to the tissue in the well. A syringe filled with 55 mM caffeine was connected to the side port of the PDMS well *via* PEEK tubing. The baseline signal from the adrenal slice in a static solution was collected for approximately 5 min. Caffeine was then added to the well using a syringe pump flowing at $10 \mu\text{L min}^{-1}$. Neurotransmitter release from the adrenal slice in response to stimulation with caffeine was recorded for an additional 10 min.

Stimulation in Flow-Through System

Microfluidic devices were used to control stimulant delivery in a flow-through system. The single-height microfluidic was used to stimulate the entire tissue slice simultaneously. One adrenal slice was placed on the electrode array and the microfluidic device was carefully positioned on top of the slice, ensuring that the agarose was completely enclosed in the PDMS channel. To prevent leaking, the PMMA compression plate was secured, and inlet and outlet

vinyl PVC tubing was connected to the device. The microfluidic channel was then filled with neurobasal media using a syringe pump flowing at $10 \mu\text{L min}^{-1}$. Baseline signal from the adrenal slice in flowing media was recorded for 3 min. Media flow was then stopped and flow of 55 mM caffeine was started simultaneously at $10 \mu\text{L min}^{-1}$ to administer stimulant to the entire tissue slice. The caffeine reached the tissue in approximately 2 min after starting flow. Neurotransmitter release from the tissue slice resulting from caffeine stimulation was recorded for an additional 5 min. Correlation of the spatiotemporal electrochemical imaging with the position of the tissue and time of stimulation was achieved through simultaneous optical imaging using the upright microscope.

Stimulation in Static Solution with Secured Tissue

The PDMS well containing nylon mesh was used to deliver stimulant to live adrenal tissue slices in a static solution environment while securing the tissue in place. The procedure followed was similar to what was described above for static solution experiments. After placing the adrenal slice on the electrode array, the PDMS well containing nylon mesh was positioned around the tissue and secured in place using the PMMA compression plate. Next, $30 \mu\text{L}$ of neurobasal media was added to the tissue in the well. A syringe was loaded with $30 \mu\text{L}$ of 55 mM caffeine in media and connected to the perpendicular port in the PDMS well using vinyl PVC tubing and a stainless steel connector. The baseline signal from the adrenal slice in a static solution was collected for 5 min. Caffeine was then added to the well by hand using the syringe. All $30 \mu\text{L}$ of caffeine was added by pushing the solution through the tubing with air in the syringe. Neurotransmitter release from the adrenal slice in response to stimulation with caffeine was recorded for an additional 5 min. Optical images of the tissue slice in the PDMS well were acquired at the beginning and the end of the experiment to correlate the position of the tissue on the array with the resulting biomarker release, and to confirm that the tissue did not move throughout the course of the experiment.

Stimulation in Flow-Through System with Secured Tissue

The multi-height microfluidic channels were used to hold the tissue in place in a flow-through system during stimulation experiments. The device containing a 2-mm-diameter region for fluid flow was used to stimulate the entire tissue slice while securing the surrounding agarose. Microfluidics, the adrenal slice, and the PMMA compression plate were set up as described for the previous flow-through experiments, ensuring that the entire slice resided in the deep portion of the channel. The microfluidic channel was then filled with neurobasal media using a syringe pump flowing at $20 \mu\text{L min}^{-1}$. Baseline signal from the adrenal slice in flowing media was recorded for 4 min. Media flow was then stopped and flow of 55 mM caffeine was started simultaneously at $20 \mu\text{L min}^{-1}$ to administer stimulant to the entire tissue slice. Neurotransmitter release from the tissue slice resulting from caffeine stimulation was recorded for an additional 10 min. Optical images of the tissue slice in the microfluidic device were acquired at the beginning and the end of the experiment to correlate the position of the tissue on the array with the resulting biomarker release, and to confirm that the tissue did not move throughout the course of the experiment.

Data Collection and Analysis

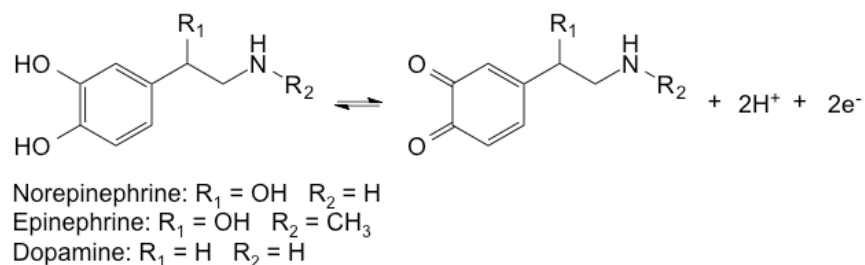
Data collection and microchip control were accomplished using a custom MATLAB graphical user interface. For all experiments described here, amperometric detection was achieved using an applied potential of +0.4 V (vs. Pt pseudo-reference electrode). Electrochemical detection across the array was accomplished by cycling through each subarray at a rate of 2 Hz, generating a complete electrochemical image every 32 s.

A second custom MATLAB script was used for offline data processing and electrochemical heat map video generation. This script provided a series of functions for data workup and analysis prior to generating the corresponding heat map video. The first function performed was a regression analysis, which corrected for electrode signal drift over the course

of the experiment and baseline offsets for each electrode. Next, gain calibration was applied based on a previously generated sensitivity curve to minimize gain variation between read channels. A Savitzky-Golay filter was applied to the data, which served to smooth high frequency and digital-to-analog quantization noise. Finally, spatial mean filtering and motion smoothing were employed to provide higher quality electrochemical heat map videos by filtering signal collected at individual electrodes relative to surrounding electrodes, and performing frame-to-frame interpolation between images. Although data collection and video generation were performed separately for this work, a future improvement that could be implemented would involve generating the electrochemical heat map in real time for observation during experimentation with live tissue.

Results and Discussion

Stimulation of live adrenal slices with caffeine resulted in localized catecholamine release, which was imaged using the high-density electrode array. Biomarker detection was accomplished using amperometry to monitor the two-electron oxidation of catecholamines including norepinephrine, epinephrine, and dopamine following the Scheme 7.1, though norepinephrine was expected to be the most prevalent species released upon stimulation with caffeine.²⁹ Control experiments in which caffeine was added to a media solution without tissue present and additional media was added to tissue in a well to disrupt the stationary solution generated no statistical change in electrochemical signal (data not shown), indicating that changes in electrochemical response upon caffeine stimulation of live tissue resulted from biomarker release from the tissue slice.



Scheme 7.1: Two-electron oxidation reaction of catecholamines released from live adrenal slices upon stimulation with caffeine.

Time-lapse heat map images of stimulated catecholamine release in a static solution environment are shown in Figure 7.4. Each pixel corresponds to a pair of electrodes, with a total of 4,096 pixels composing the entire electrochemical image. Blue pixels indicate regions of low or baseline signal, and red pixels correspond to regions of high current, indicating catecholamine release from the tissue. The first panel represents the first cycle through the 64 subarrays after placing the tissue on the electrode array. The region of high signal corresponds to the physical location of the tissue on the array at the start of the experiment. High signal observed was likely due to biomarker accumulation at the surface of the tissue upon release from the tissue slice while it was transferred from the petri dish to the electrode array. A baseline signal was established by 5 min, at which time caffeine addition was started. By 10 min, a noticeable increase in signal occurred, as seen in the third panel in Figure 7.4, indicating catecholamine release from the tissue. The signal continued to increase until 15 min, at which time the experiment was terminated.

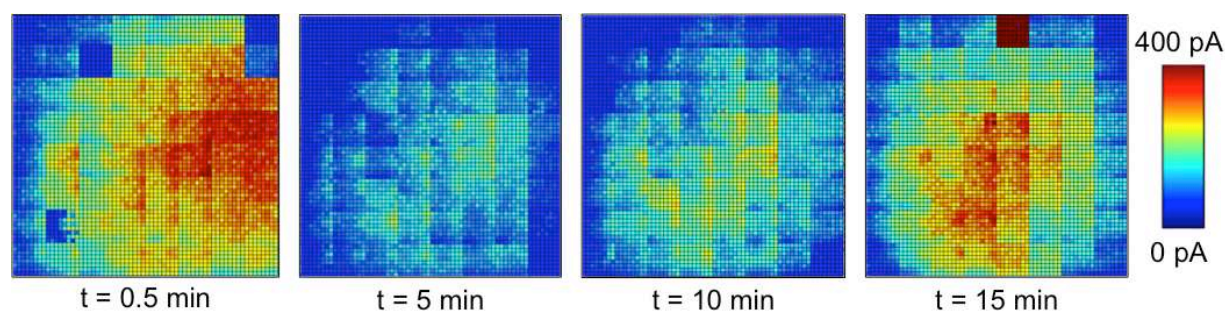


Figure 7.4: Time-lapse heat map images of catecholamine release from live adrenal tissue in a PDMS well. Red pixels correspond to regions of high current, indicating biomarker release from the tissue, while blue pixels indicate regions of low or baseline signal. Caffeine was added as a stimulant at approximately 5 min. The tissue shifted position upon addition of caffeine. An oxidation potential of +0.4 V (vs. Pt) was used, and the switching rate between subarrays was 2 Hz.

It was observed in the electrochemical images that the location of biomarker release after caffeine stimulation was inconsistent with the location of the tissue at the start of the experiment. Caffeine addition occurred from the right hand side of the images, likely pushing the tissue to the left due to disturbance of the stationary solution in the PDMS well. The change in tissue position was confirmed by visual observation upon disassembly of the setup at the conclusion of the experiment. The instability of tissue position upon stimulant addition necessitated a method of securing the tissue in place for the experiment, which was investigated below.

A live adrenal slice was then stimulated with caffeine in a flow-through system using a microfluidic device. Simultaneous optical imaging using the upright microscope was used for this experiment to correlate the time and location of catecholamine release with the time of caffeine addition and the physical location of the tissue slice on the electrode array. The results in Figure 7.5 show time-lapse images of the optical and electrochemical data collected. Additionally, these two videos were overlaid for direct correlation between the location of catecholamine release and the position of the tissue on the electrode array. At the beginning of the experiment, an initial signal was again observed at the position of the tissue, likely due to

biomarker accumulation before starting electrochemical detection. After the caffeine solution, which was dyed red for visualization, reached the tissue slice, biomarker release from the adrenal tissue increased, as seen in the second panel in Figure 7.5. The signal continued to increase, localized to the location of the tissue, throughout the remainder of the experiment, which was terminated at 7 min. These results indicate that adrenal tissue stimulation with 55 mM caffeine in a flow-through system resulted in localized catecholamine release from the tissue slice.

For an ideal electrochemical imaging setup, the entire tissue slice should be contained within the area of the electrode array to obtain a complete picture of the chemistry occurring at the surface of the live tissue. In the microfluidic experiment described above, however, it can be observed that the tissue slice was offset towards the right edge of the electrode array. This non-ideal tissue position was a result of solution introduction into the microfluidic device. Despite centering the tissue on the array during the initial setup, when media first entered the microfluidic channel flowing from left to right, the tissue was pushed downstream slightly, as the channel depth (412 μm) was greater than the thickness of the tissue slice (250 μm) allowing tissue movement. To prevent the tissue from moving in subsequent experiments, the multi-height microfluidic channel described above was developed to secure the agarose during the experiment while allowing solution delivery to the tissue.

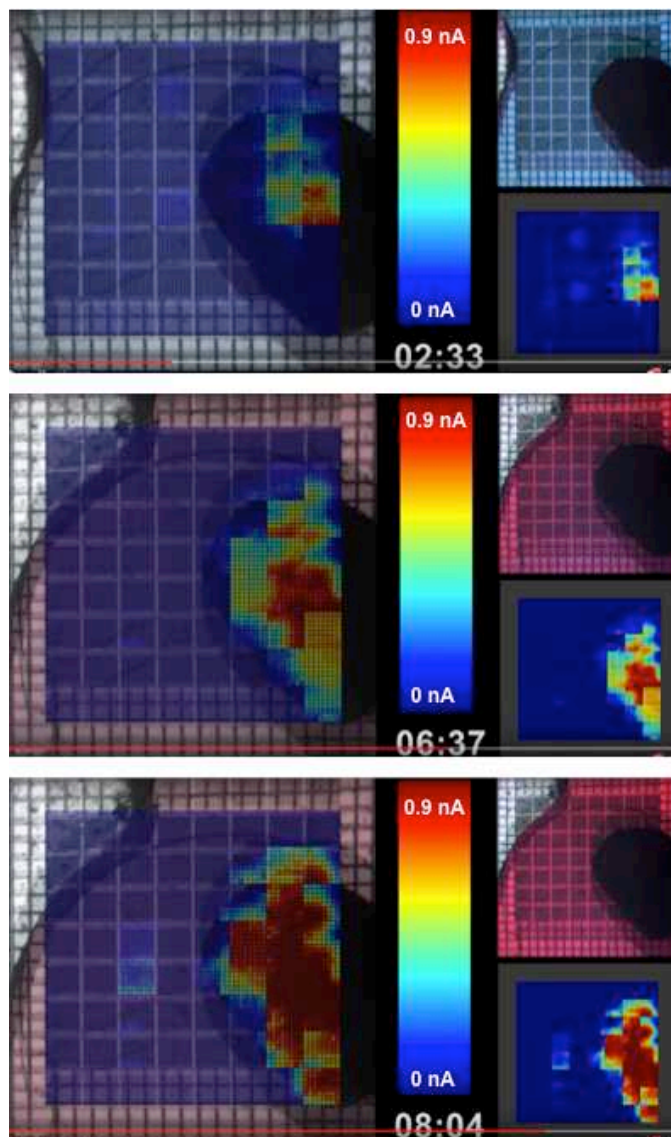


Figure 7.5: Time-lapse heat map images of catecholamine release from live adrenal tissue in a PDMS well. Red pixels correspond to regions of high current, indicating biomarker release from the tissue, while blue pixels indicate regions of low or baseline signal. Caffeine was added as a stimulant at approximately 5 min. The tissue shifted position upon addition of caffeine solution. An oxidation potential of +0.4 V (vs. Pt) was used, and the switching rate between subarrays was 2 Hz.

PDMS devices were then implemented to secure the position of the tissue slice throughout the course of the stimulation experiments. The first utilized nylon mesh in a PDMS well to hold the tissue against the electrode array while allowing stimulant delivery from above for static solution experiments (Figure 7.6A). To secure the tissue in a flow-through setup, multi-

height microfluidic channels were used, where the agarose surrounding the tissue was held in place by the shallower regions of the channel while solution was allowed to flow over the tissue through the deeper portion of the channel, as shown in Figure 7.6B. Upon replicate experiments ($n>3$), both of these devices were demonstrated to be effective at securing the tissue in place throughout the stimulation experiments. Addition of solution to the PDMS well did not result in tissue movement, evidenced by comparison of optical images acquired at the start and end of the experiment, and similarly, solution flow down the microfluidic channel did not affect the position of the tissue when secured by the multi-height channel.

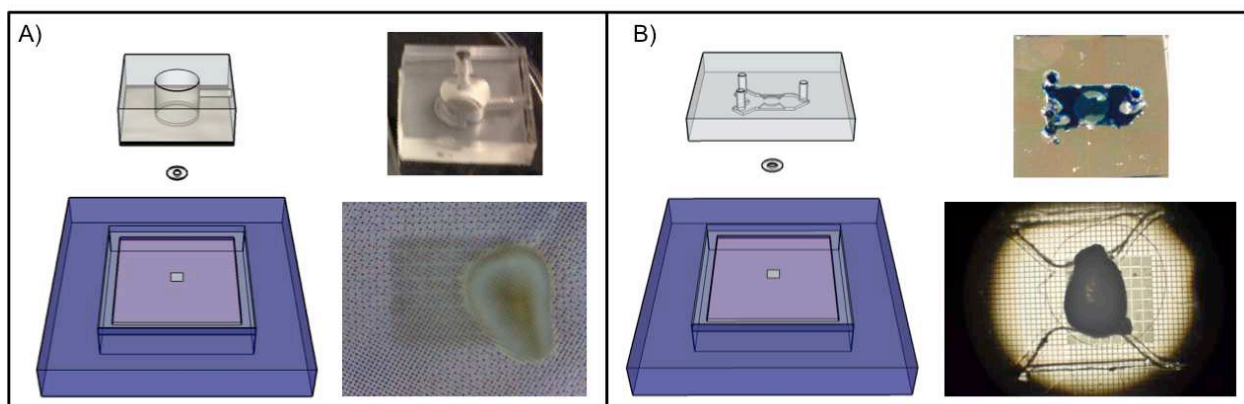


Figure 7.6: A) Schematic of a PDMS well containing nylon mesh interfacing with a tissue slice and the electrode array. The image in the top right corner shows a PDMS well with nylon mesh. A tissue slice secured between nylon mesh and the electrode array is shown in the bottom right corner. **B)** Schematic of a multi-height PDMS microfluidic channel interfacing with a tissue slice and the electrode array. In the top right corner, the image shows a dye solution in the microfluidic channel passing over a 3-mm-diameter agarose slice. The image in the bottom right corner shows a live adrenal slice embedded in agarose in the multi-height microfluidic channel.

Preliminary results of caffeine-stimulated catecholamine release from live tissue using the PDMS well containing nylon mesh were acquired and are shown in Figure 7.7. Optical images of the tissue slice in the well at the start and end of the experiment are shown, demonstrating that the tissue maintained its position upon addition of the caffeine solution. Prior to caffeine addition, a baseline signal was observed across the electrode array. After the tissue was stimulated with caffeine, catecholamine release localized to the position of the tissue was

observed. These results indicate that the nylon mesh is effective at securing the tissue in place while allowing stimulation in a static solution to generate biomarker release from a live tissue slice.

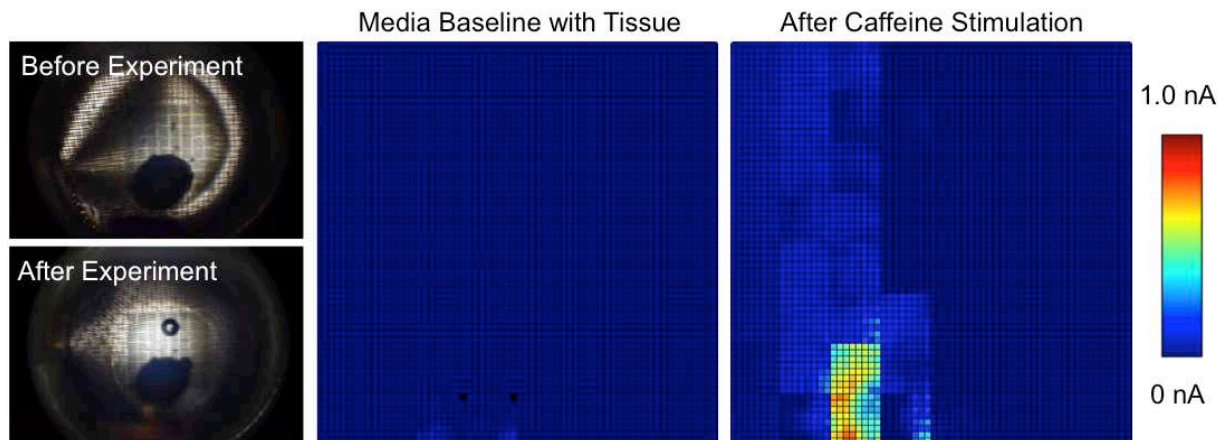


Figure 7.7: Optical images of tissue on the electrode array and time-lapse heat map images of catecholamine release from live adrenal tissue in a PDMS well with nylon mesh. Red pixels correspond to regions of high current, indicating biomarker release from the tissue, while blue pixels indicate regions of low or baseline signal. The nylon mesh prevented the tissue from moving during the experiment. An oxidation potential of +0.4 V (vs. Pt) was used, and the switching rate between subarrays was 2 Hz.

The multi-height microfluidic device was used to demonstrate caffeine-stimulated catecholamine release from a live adrenal slice in a flow-through system while maintaining the position of the tissue. Optical images of the tissue in the channel and still frames from the electrochemical heat map video are shown in Figure 7.8. The optical images demonstrated that the multi-height channel prevented tissue movement resulting from solution flow. The caffeine solution was dyed blue to verify that the stimulant reached the tissue during the experiment. As shown in the electrochemical heat maps, the electrode array showed a baseline signal prior to stimulation.

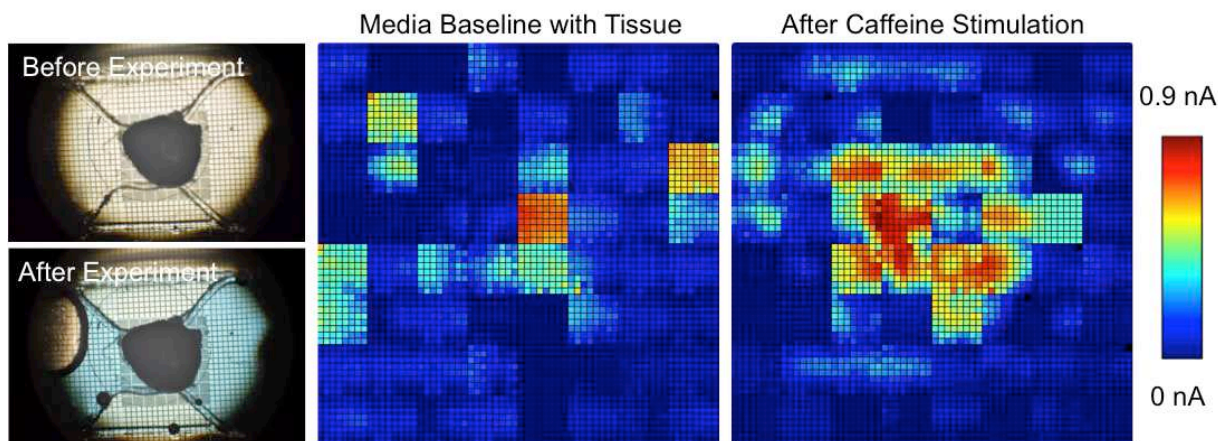


Figure 7.8: Optical images of tissue on the electrode array and time-lapse heat map images of catecholamine release from live adrenal tissue in a multi-height PDMS channel. Red pixels correspond to regions of high current, indicating biomarker release from the tissue, while blue pixels indicate regions of low or baseline signal. The caffeine solution was dyed blue for easier visualization. The multi-height microfluidic channel prevented the tissue from moving during the experiment. An oxidation potential of +0.4 V (vs. Pt) was used, and the switching rate between subarrays was 2 Hz.

As this work moves forward, the goal is to use electrochemical imaging to investigate how cells communicate. This will be accomplished by applying stimulant to a localized area of a tissue slice and image biomarker release across the entire tissue slice in response to the stimulation. A multi-height PDMS microfluidic channel has been designed for localized stimulant delivery to a live tissue slice on the electrode array. A 3D schematic and photograph of the microfluidic device are shown in Figure 7.9. The microfluidic channel uses multiple channel heights as described above to secure the tissue in place while solution is flowing. The shallower regions of the channel also aim to direct fluid over localized regions of the tissue by coming into conformal contact with the tissue and surrounding agarose, causing the path of least resistance for fluid flow to be the narrow, deep region of the channel intended for localized stimulant delivery. The dye solution in the photograph in Figure 7.9 demonstrates localized fluid flow in a 1-mm-wide region of the channel, which can be decreased in size for future designs to localize stimulant delivery to a smaller region of the tissue slice. Observation of which regions of the tissue release biomarkers at different times after stimulation of a small area of the tissue will

provide information on how cells communicate across a tissue slice, which can be translated to cellular communication at an organ scale. Interfacing the device with an upright microscope for these experiments will allow direct correlation of location of stimulant delivery and resulting electrochemical signals.

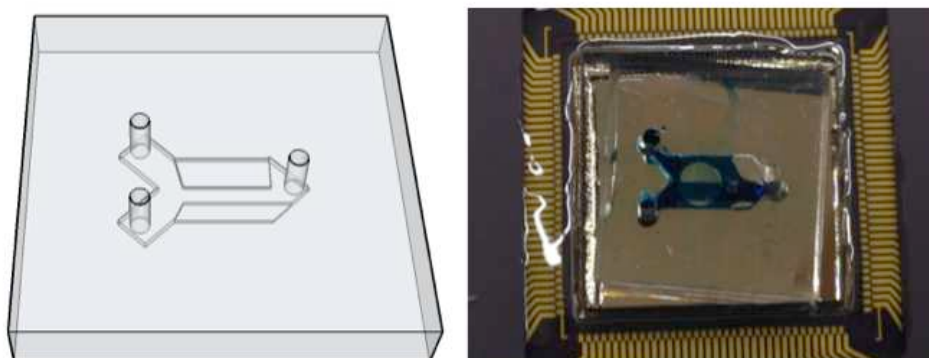


Figure 7.9: 3D schematic and photograph of multi-height microfluidic channel for localized fluid delivery to a live tissue slice. The upper and lower edges of the microfluidic channel are shallower than the rest of the channel to secure the tissue in place and direct fluid to a localized region of the tissue slice. The image on the right shows the channel containing a blue dye solution flowing through a localized 1-mm-wide channel over a 3-mm-diameter slice of agarose.

Conclusions

Electrochemical imaging techniques are complementary to existing optical imaging methods and expand the accessible library of target biomarkers while providing spatiotemporal resolution at the scale of an *ex vivo* tissue slice. The electrode array described here was successfully interfaced with live tissue slices and microfluidic devices, and provided electrochemical detection of caffeine-stimulated catecholamine release from live adrenal slices with spatiotemporal resolution. Biomarker release was localized to the position of the tissue on the electrode array, which was confirmed with optical imaging. Microfluidic devices were successfully implemented to secure the tissue in place at the surface of the electrode array during static solution and flow-through experiments. Iterative device development generated a microfluidic channel that delivered stimulant to localized regions of live tissue slices on the array

to study cellular communication across a tissue slice. Further work will improve the experimental setup to provide simultaneous optical and electrochemical imaging for all experiments. Cellular communication will be investigated using the microfluidic devices described in this work, and the system will be adapted to monitor other types of murine tissue slices, such as brain and intestine. The electrode array will also be improved, increasing the number of electrodes in the array, thus improving spatial resolution and field of view. Other electronic improvements will include simultaneous detection from a larger number of electrodes to improve the data collection rate, therefore improving temporal resolution.

This work is supported in part by National Science Foundation (Grant No. DGE-1450032). The silicon-based microelectrode chip was manufactured by Avago Technologies. Their technical assistance and generous support for this project are greatly appreciated.

REFERENCES

1. V. Sourjik and N. S. Wingreen, *Current opinion in cell biology*, 2012, **24**, 262-268.
2. S. H. Zigmond, *The Journal of cell biology*, 1977, **75**, 606-616.
3. J. Diao, L. Young, S. Kim, E. A. Fogarty, S. M. Heilman, P. Zhou, M. L. Shuler, M. Wu and M. P. DeLisa, *Lab on a Chip*, 2006, **6**, 381-388.
4. S. D. Nathanson, *Cancer*, 2003, **98**, 413-423.
5. K. Hensley, M. L. Mardt, Z. Yu, H. Sang, W. R. Markesbery and R. A. Floyd, *The Journal of neuroscience*, 1998, **18**, 8126-8132.
6. Y. Yi, L. Sanchez, Y. Gao and Y. Yu, *Analyst*, 2016.
7. K. T. Schomacker, J. K. Frisoli, C. C. Compton, T. J. Flotte, J. M. Richter, N. S. Nishioka and T. F. Deutsch, *Lasers in Surgery and Medicine*, 1992, **12**, 63-78.
8. Y. Amoh, K. Katsuoka and R. M. Hoffman, *Current Pharmaceutical Design*, 2008, **14**, 3810-3819.
9. H. Y. Peng, H. Tang and J. H. Jiang, *Science China-Chemistry*, 2016, **59**, 783-793.
10. B. N. G. Giepmans, S. R. Adams, M. H. Ellisman and R. Y. Tsien, *Science*, 2006, **312**, 217-224.
11. A. Cassese, S. R. Ellis, N. O. Potocnik, E. Burgermeister, M. Eber, A. Walch, A. van den Maagdenberg, L. A. McDonnell, R. M. A. Heeren and B. Balluff, *Analytical Chemistry*, 2016, **88**, 5871-5878.
12. S. R. Ellis, J. Cappell, N. O. Potočnik, B. Balluff, J. Hamaide, A. Van der Linden and R. M. Heeren, *Analyst*, 2016, **141**, 3832-3841.
13. H.-M. Bergman, E. Lundin, M. Andersson and I. Lanekoff, *Analyst*, 2016, **141**, 3686-3695.
14. R. M. Caprioli, T. B. Farmer and J. Gile, *Analytical Chemistry*, 1997, **69**, 4751-4760.
15. A. C. Grey, A. K. Gelasco, J. Section, R. A. Moreno-Rodriguez, E. L. Krug and K. L. Schey, *Anatomical Record-Advances in Integrative Anatomy and Evolutionary Biology*, 2010, **293**, 821-828.
16. J. K. Lee, E. T. Jansson, H. G. Nam and R. N. Zare, *Analytical chemistry*, 2016, **88**, 5453-5461.
17. L. J. Johnson, E. Cohen, D. Ilg, R. Klein, P. Skeath and D. A. Scribner, *Journal of Neuroscience Methods*, 2012, **205**, 223-232.
18. E. Ferrea, A. Maccione, L. Medrihan, T. Nieuw, D. Ghezzi, P. Baldelli, F. Benfenati and L. Berdondini, *Frontiers in Neural Circuits*, 2012, **6**, 14.

19. D. J. Bakkum, U. Frey, M. Radivojevic, T. L. Russell, J. Muller, M. Fiscella, H. Takahashi and A. Hierlemann, *Nature Communications*, 2013, **4**, 12.
20. L. Berdondini, P. D. van der Wal, O. Guenat, N. F. de Rooij, M. Koudelka-Hep, P. Seitz, R. Kaufmann, P. Metzler, N. Blanc and S. Rohr, *Biosensors & Bioelectronics*, 2005, **21**, 167-174.
21. B. N. Kim, A. D. Herbst, S. J. Kim, B. A. Minch and M. Lindau, *Biosensors & Bioelectronics*, 2013, **41**, 736-744.
22. J. Rothe, O. Frey, A. Stettler, Y. H. Chen and A. Hierlemann, *Analytical Chemistry*, 2014, **86**, 6425-6432.
23. A. Kara, A. Reitz, J. Mathault, S. Mehrou-Loko, M. A. Amirdehi, A. Miled and J. Greener, *Lab on a Chip*, 2016, **16**, 1081-1087.
24. J. Petrovic, P. L. Walsh, K. T. Thornley, C. E. Miller and R. M. Wightman, *Endocrinology*, 2010, **151**, 1773-1783.
25. H. D. Xu, P. L. Zuo, S. R. Wang, L. Zhou, X. X. Sun, M. Q. Hu, B. Liu, Q. H. Wu, H. Q. Dou, F. P. Zhu, S. S. Teng, X. Y. Zhang, L. Wang, Q. Li, M. Jin, X. J. Kang, W. Xiong, C. H. Wang and Z. A. Zhou, *Analyst*, 2015, **140**, 3840-3845.
26. A. O. Martin, M. N. Mathieu, C. Chevillard and N. C. Guerineau, *Journal of Neuroscience*, 2001, **21**, 5397-5405.
27. A. M. Poisner, *Proceedings of the Society for Experimental Biology and Medicine*, 1973, **142**, 103-105.
28. R. Borges, *Seminars in Cell & Developmental Biology*, 1997, **8**, 113-120.
29. B. A. Berkowitz, J. H. Tarver and S. Spector, *European journal of pharmacology*, 1970, **10**, 64-71.
30. W. Douglas, *Pharmacological reviews*, 1966, **18**, 471-480.
31. J. B. Wydallis, R. M. Feeny, W. Wilson, T. Kern, T. Chen, S. Tobet, M. M. Reynolds and C. S. Henry, *Lab on a Chip*, 2015, **15**, 4075-4082.
32. R. M. Feeny, J. B. Wydallis, T. Chen, S. Tobet, M. M. Reynolds and C. S. Henry, *Electroanalysis*, 2014, **26**.

CHAPTER 8. DEVELOPMENT OF A MULTI-ASSAY SYSTEM FOR DETECTION OF FELINE IMMUNODEFICIENCY VIRUS FROM DRIED BLOOD SPOTS

Feline Immunodeficiency virus (FIV) affects up to 5% of cats worldwide, and early diagnosis is critical to maintaining the cats' quality of life and preventing unnecessary euthanasia. The most common vaccination uses a killed whole-virus, making vaccinated cats indistinguishable from infected cats *via* the standard veterinary screening method, which detects FIV antibodies. Generation of a two-part assay could help minimize unnecessary euthanasia by direct detection of the virus after positive antibody detection. The project described here aims to combine paper-based and polymer-based microfluidic devices for a two-step assay to more accurately diagnose FIV with a user-friendly automated instrument. This chapter served as a research proposal. The work proposed was an extension of fields studied in completion of this dissertation.

Specific Aims

The goal of this work is to develop a two-part analysis system for diagnosis of feline immunodeficiency virus (FIV) capable of distinguishing between infected and vaccinated cats to prevent unnecessary euthanasia of healthy cats. The first step, a colorimetric enzyme-linked immunosorbent assay (ELISA), provides a simple yes/no indicator of the presence of the FIV antibodies. This will be accomplished using a paper-based microfluidic device to provide rapid and inexpensive analysis. Samples with positive results, which will come both from infected and vaccinated cats, will then be analyzed using insulated isothermal polymerase chain reaction (iiPCR). While this method is more time-consuming and costly, it directly detects the virus, providing accurate diagnoses that prevent unnecessary euthanasia. The platform will be self-contained with few procedural steps required by the user. Transfer of sample from the ELISA test to the iiPCR will be automatic and only occur for positive results. The system will be

developed to be compatible with dried blood spot samples to provide simple sample collection, storage, and volume control.

Aim 1. *Develop a colorimetric enzyme-linked immunosorbent assay (ELISA) on a paper-based microfluidic platform as a screening test for the presence of feline immunodeficiency virus (FIV) antibodies.* This analysis system will provide an inexpensive method to screen subjects for the presence of FIV antibodies prior to performing more costly and time-consuming tests to confirm the infection.

Aim 2. *Generate an insulated isothermal polymerase chain reaction (iiPCR) system with a detection system for FIV detection from dried blood spot samples.* iiPCR will provide distinction between infected and vaccinated cats by directly detecting the virus itself rather than FIV antibodies.

Aim 3. *Integrate the two platforms developed in the previous aims into a self-contained system for the sequential diagnosis of FIV from dried blood spot samples in a user-friendly device.* By combining the two analysis platforms into a single system, a rapid, accurate diagnosis can be made to help mitigate spread of the disease and prevent the unnecessary euthanasia associated with false positive results obtained in the clinical setting.

Background and Significance

Feline immunodeficiency virus (FIV) affects 2-5% of cats worldwide and is primarily transmitted from bites occurring in territorial fights.¹⁻³ Symptoms of FIV include lethargy, anorexia, neurological disorders, and cancers, and can progress to feline acquired immunodeficiency syndrome (FAIDS), ultimately leading to death.³⁻⁶ Early detection of infection is critical to maintain the cat's health and prevent spreading the infection to other healthy cats.

Current screening methods used in veterinary clinics provide fast, inexpensive screening for the presence of FIV antibodies.⁷⁻⁹ These tests, however, frequently result in false positives for vaccinated cats, as a killed whole-virus vaccine is typically used, and the screening test cannot distinguish between antibodies produced as a result of infection or those produced after vaccination.^{7, 10-12} Positive diagnosis frequently leads to euthanasia for the cat, resulting in unnecessary euthanasia for false positive cases.⁷ More expensive, time-consuming tests for the presence of the virus exist in research settings but have not been incorporated into veterinary offices. The uncertainty between vaccinated and infected cats is particularly problematic in the case of stray cats with unknown medical histories. Accurate diagnosis of this disease can prevent unnecessary euthanasia of healthy cats, improve quality of life for cats with FIV through early diagnosis and treatment, and help control the spread of the disease.

Development of a two-part analysis system for diagnosis of FIV in cats using minimally-invasive sampling methods will provide inexpensive, accurate diagnosis of FIV-positive cats, helping maintain infected cats' quality of life while controlling spread of the disease. The first stage of analysis will consist of a colorimetric enzyme-linked immunosorbent assay (ELISA) as a simple yes/no indicator of the presence of the FIV antibodies, similar to the diagnostic tests currently used in veterinary clinics. To eliminate the problem of false positives associated with vaccinated cats, samples containing FIV antibodies will be further evaluated using insulated isothermal polymerase chain reaction (iiPCR) to directly detect the virus.

Diagnostic tests used to screen large populations must be available at low cost with simple operation to be effective. Incorporation of microfluidics into the screening platform for sample control and analysis provides compatibility with small volumes of samples and reagents, which dramatically decreases the cost of each test. Sample handling and analysis using microfluidics also allows a high level of automation in the analysis. Automated fluid control in microfluidic devices has been achieved using multiple methods, including cartridges containing air spacers in tubing,¹³ capillary systems,¹⁴⁻¹⁶ continuous flow by capillary forces,¹⁷ and

integrated syringe pumps,¹⁸ among many others, minimizing the required user steps while maintaining high precision and accuracy of fluid transport during analysis. Using an automated system for FIV diagnosis minimizes the amount of training a technician must receive and simplifies the analysis procedure, decreasing the cost of each test. Development of a two-part system for the diagnosis of FIV in cats will improve the accuracy of the screening procedure, allowing quality of life for infected cats while preventing spread of the disease to healthy cats and unnecessary euthanasia.

Research Design and Methods

Development of a two-part analysis system compatible with dried blood spots will provide an inexpensive platform for accurate diagnosis of feline immunodeficiency virus. Two separate cartridges will allow rapid, inexpensive screening through detection of FIV antibodies followed by direct virus detection to eliminate false positives that can lead to unnecessary euthanasia. Automation improves ease-of-use and simplifies diagnosis.

Aim 1: Develop colorimetric ELISA to screen for FIV antibodies

Currently, clinical samples are analyzed using the IDEXX SNAP FIV/FeLV Combo Test (Figure 8.1), which uses an enzyme-linked immunosorbent assay (ELISA) with bidirectional flow to generate a colorimetric indicator of the presence of FIV antibodies. Although this clinical test has high sensitivity and specificity based on visual interpretation of results (100% and 99.6%, respectively),¹⁹ the assay does not distinguish between vaccinated and infected cats.¹²



Figure 8.1: SNAP FIV/FeLV Combo Test

Colorimetric ELISA technology will provide a simple screening method to confirm or deny the presence of FIV antibodies to determine the necessity for further sample analysis. Paper-based microfluidics offers an inexpensive, disposable platform compatible with colorimetric ELISA to screen for the presence of FIV antibodies. ELISA provides high specificity, targeting a specific analyte based on the interactions between antibodies and corresponding antigens. A schematic of the chemistry that will be employed for FIV antibody detection is outlined in Figure 8.2. Viral antigen is immobilized on the surface of the paper, which is then blocked with bovine serum albumin (BSA) to limit non-specific adsorption. Serum containing FIV-specific IgG is then reacted with the modified paper. Incubation with alkaline phosphatase (ALP)-conjugated anti-feline IgG results in immobilization of ALP, which is then reacted with the ALP substrate solution (5-bromo-4-chloro-3-indolyl phosphate and nitro blue tetrazolium, BCIP/NBT) to generate a colored precipitate for detection.

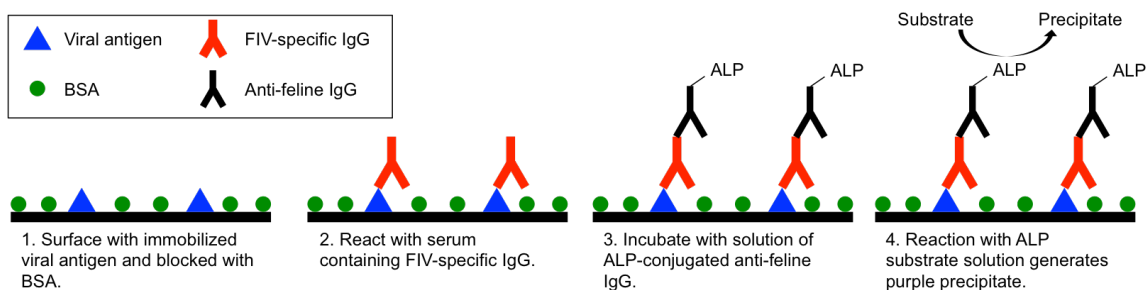


Figure 8.2: Schematic of colorimetric ELISA for detection of FIV antibodies.

Colorimetric ELISA has previously been adapted for use in paper-based microfluidics.²⁰⁻
²⁴ The inherent self-wetting property of paper through capillary action provides an ideal platform for transport of reagents and samples to a detection region in the device.²⁵⁻²⁷ Using paper-based microfluidic devices also offers the advantage of preloading reagents through absorption into the paper, minimizing the number of user steps required during the sample analysis.

FIV antibody detection through colorimetric ELISA will be developed on a paper-based microfluidic platform with built-in controls run in parallel. Paper-based ELISA devices frequently require multiple user steps throughout the analysis process, including reagent loading and wash steps, or physically moving layers of the microfluidic device to allow fluid transport for each step.^{20, 21} The system proposed here will be developed to require the user to simply load the sample and add a buffer. Further automation in Aim 3 will eliminate the need for manual buffer addition. The basic layout of the paper-based device designed as a multistep lateral flow assay is shown in Figure 8.3.

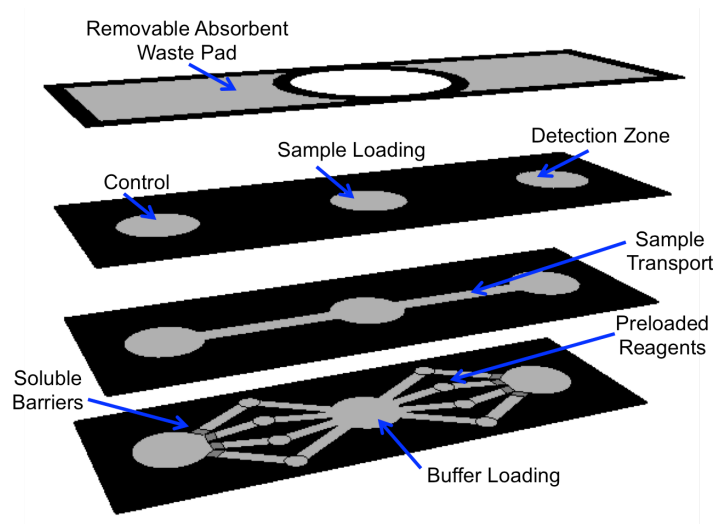


Figure 8.3: Schematic of 3D paper-based ELISA device. Black represents wax-printed barriers on filter paper represented in grey. Reagents are preloaded into individual channels on the bottom layer and are sequentially delivered to detection zones with timing controlled by soluble barriers on the paper.

A multilayer 3D paper-based device^{26, 28, 29} will be developed to minimize size and reagent volume. The channel networks on each layer are defined using standard wax-printing

techniques.³⁰⁻³² The top layer of the device is a removable absorbent waste pad to draw buffer and reagents through the detection zone of the device. Below the waste pad is a sample loading and detection layer. The detection zone will be modified with immobilized viral antigen and surface blocking agents. A control will be included in this layer to run in parallel and account for non-specific binding. Below the sample loading layer is a channel to simultaneously transport sample to the detection and control zones for incubation with immobilized antigen. The bottom layer consists of a central buffer loading zone, and the remaining outer surface area is sealed to the ambient environment using a water-impermeable adhesive layer (e.g. packing tape) to contain loaded buffer to the device. Buffer is transported to the upper layers using multiple channels branching from the common buffer loading zone. Each channel leads to the sample zone after vertical transport, and select channels contain preloaded reagents, including ALP-conjugated anti-feline IgG and ALP substrate. Preloading will be accomplished either manually, or using a reagent printer.³³⁻³⁶ Specified timing of fluid delivery to the sample and control zones will be achieved using water-soluble barriers, which have previously been used to control timing in paper-based microfluidic devices.^{37, 38} Timing of fluid flow will be optimized using previously investigated strategies.³⁹

Device operation will consist of adding sample to the sample loading zone and allowing incubation with immobilized antigen. Buffer will be added *via* the bottom layer and transported through each of the four channels to the detection zones, carrying immobilized reagents when applicable. The four steps using the transported buffer are as follows: 1) wash buffer removes unbound material from the detection zone, 2) ALP-conjugated anti-feline IgG is transported to the detection zone to react with immobilized FIV antibodies from the sample, 3) wash buffer removes unbound material from the detection zone, and 4) ALP substrate solution (BCIP/NBT) reacts with immobilized ALP to form a colored product. The waste pad is then removed and the color change is analyzed using a desktop scanner and image analysis software.

Conditions such as reagent concentrations, buffer volumes, and reaction times will be optimized to provide detection limits suitable for detection of FIV antibodies in infected and vaccinated cats. If optimizing the above conditions proves to be inadequate to provide suitable detection limits, strategies such as preconcentration will be explored, which have previously been employed in paper-based microfluidics.^{40, 41}

The paper-based ELISA platform described above can easily be adapted to be compatible with dried blood spots. Collection of dried blood spots from cats is minimally invasive and inexpensive.^{42, 43} Handling samples of blood dried onto filter cards is also simpler relative to liquid samples, and the cards can be stored for long periods of time at room temperature without degradation.^{43, 44} Dried blood spots also offer an inherent preconcentration method by extracting from the paper with low volumes or by stacking multiple samples to increase the amount of available material.

Aim 2: Develop iiPCR for detection of FIV

A system using insulated isothermal polymerase chain reaction (iiPCR) will be developed for the direct detection of FIV from dried blood spot samples. Currently, direct detection of the virus is limited to tests performed in commercial and research diagnostic laboratories.⁴⁵ Systems have been developed for FIV detection using PCR, but require many user steps and are expensive and bulky,^{46, 47} though recently, a portable, user-friendly iiPCR system has been developed for the detection of FIV.⁴⁵ For this work, a portable, user-friendly system will be developed using iiPCR in a microfluidic device for the detection of FIV from dried blood spots to distinguish between infected and vaccinated cats.

iiPCR offers several distinct advantages over conventional PCR. Temperature cycling is achieved by natural thermal convection in a closed vessel. A heating element at the bottom of the vessel provides the heat necessary for the denaturation step. Heated solution naturally cycles to the top of the vessel, where it cools, undergoes annealing and extension, and returns

to the bottom of the vessel.^{48, 49} The natural convection eliminates the need for multiple heating and cooling elements, decreasing the complexity of the required instrumentation. Reaction in a closed vessel also eliminates the need for user intervention to transfer or mix the samples.

A diagram of the iiPCR device is shown in Figure 8.4. The sample and reagents are contained in a closed vessel, such as a capillary tube, which is positioned above a heating element within an insulating material. The PCR process occurs without intervention from the user. DNA denatures at high temperatures (95 °C) then anneals with primers and extends to duplicate the DNA in a single cycle. The primers that will be investigated first will be based on the work reported by Wilkes, *et al.*, which were designed to amplify a conserved area of FIV.⁴⁵

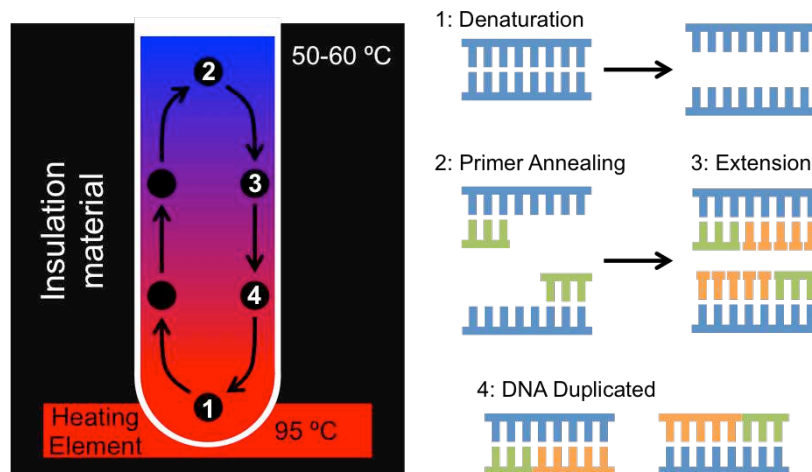


Figure 8.4: Schematic of iiPCR device for FIV detection. Natural thermal convection occurs between lower heating element and upper insulated region. DNA is duplicated in one cycle, denaturing at 95 °C and annealing with preloaded primers at 50-60 °C.

Quantification is achieved using fluorescence detection with fluorescent probe hydrolysis.⁵⁰ Conditions such as reaction time and reagent concentrations will be optimized during the development of this system. Previous systems reported have used reverse transcription iiPCR,⁴⁵ which amplifies genomic RNA and proviral forms of FIV, resulting in false positives for vaccinated cats. Performing iiPCR without the reverse transcription step will amplify only the proviral DNA, which is present only in infected cats and not in vaccinated cats.⁵¹

Ease-of-use can be further improved by preloading reagents into the reaction vessel, eliminating the need for the user to load reagents at the time of use. Preloading can be accomplished using lyophilized pellets^{52, 53} or by drying reagents onto a membrane to use during the loading process.^{33, 54} Further adaptation of the system will allow compatibility with dried blood spots as the sample platform. Blood samples collected onto filter cards will be extracted and transferred to the reaction vessels. If the sample vessels used are capillary tubes, this transfer will be accomplished simply by contacting the extracted filter cards with the capillary tube. Other methods of sample transfer will be investigated if a different type of reaction vessel is used. Preloading reagents into the reaction vessel minimizes the number of user steps required at the time of analysis.

Aim 3: Integrate paper-based ELISA and iiPCR into a self-contained system

The paper-based ELISA platform for the detection of FIV antibodies and the iiPCR for the direct detection of FIV will be integrated into a single, user-friendly system for the sequential diagnosis of FIV from dried blood spot samples. The ELISA and iiPCR assays will be contained in separate cartridges that can be individually loaded for sample analysis. Designing a system with separate cartridges allows initial sample screening *via* ELISA, followed by optional iiPCR analysis for samples positive for FIV antibodies, minimizing the cost and time required to analyze negative samples.

The system will be comprised of three main steps: sample extraction and pre-treatment, ELISA, and iiPCR. The user will simply load the dried blood spot sample into the system using disposable sample cartridges (Figure 8.5). These sample cartridges will be made from acrylic or another inexpensive plastic, and will be designed to contain fluid to the sample card, avoiding contamination of the rest of the system. Extraction and pre-treatment conditions will be optimized to provide high extraction efficiency. The extracted sample will then be transferred to two separate loading zones, one each for the ELISA and iiPCR cartridges. The ELISA cartridge

will be activated first. Buffer will be transported to the cartridge from reservoirs with internal tubing in the system. After the system has completed the ELISA, the colorimetric response will be analyzed by a simple built-in device to screen for positive samples. Based on these results, the instrument will provide a recommendation to the user whether or not to continue to the last step of the analysis (iiPCR). The user will then be able to confirm the positive or negative result and select to run iiPCR or end the analysis for that particular sample.

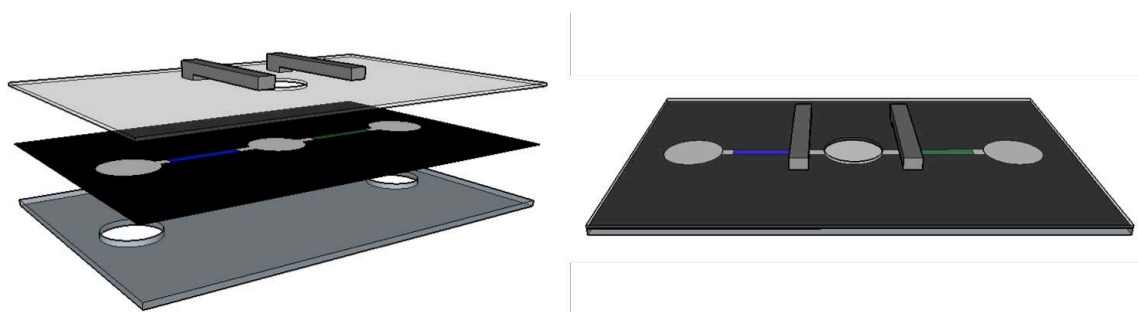


Figure 8.5: Schematic of sample cartridge. **Left)** Expanded view of cartridge. The top layer includes clips to hold the sample filter in place, with access to the center layer for transport to the ELISA and iiPCR cartridges. The center layer contains pretreatment reagents, indicated by blue and green. The bottom layer isolates the sample from the other cartridges until analysis is initiated. **Right)** Collapsed view of cartridge.

For samples requiring iiPCR after ELISA, the blood sample transported to the second loading zone of the sample cartridge will be transferred to the iiPCR cartridge. All components that contact the sample will be parts of individual cartridges rather than the instrument itself, preventing contamination and avoiding the need to clean the instrument between samples. All necessary reagents will be contained within the individual cartridge, and buffer will be transported to the cartridge *via* the system's internal tubing. Heating elements to perform iiPCR will be housed within the instrument rather than in the cartridges to minimize the cost and increase the disposability of individual cartridges. The iiPCR cartridge will contain notches or clips to snap into place in the instrument to properly align with the heating element.

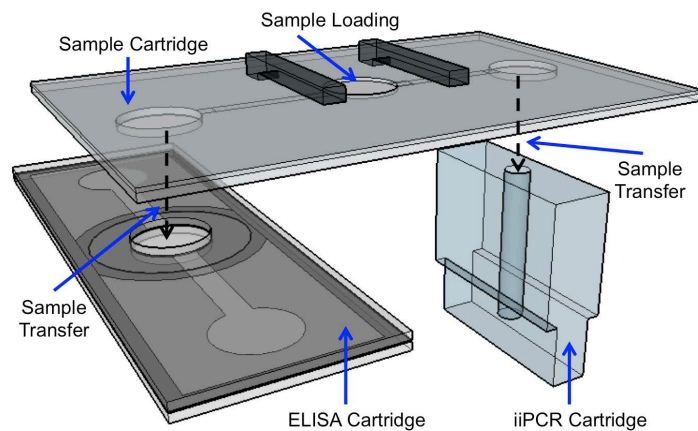


Figure 8.6: Example of integration of the three cartridges. Sample is loaded at the top center of the sample cartridge and is transported laterally to the ELISA and iiPCR cartridges. All necessary tubing and heating elements are built into the instrument and are not included in individual cartridges.

The outcome of the iiPCR assay will be analyzed by the instrument, displaying either a positive or negative result to the user. All used cartridges will then be removed from the instrument for disposal, and new cartridges loaded for the next sample. A schematic example of how the three cartridges will interface in the interface is shown in Figure 8.6.

All of the cartridges and required buffers and reagents will be contained in a single instrument (Figure 8.7) and will be easily interchangeable to allow simple operation by the end user. The required electronics and fluid control components will be built into the system, minimizing disruption by the user to provide a robust instrument.

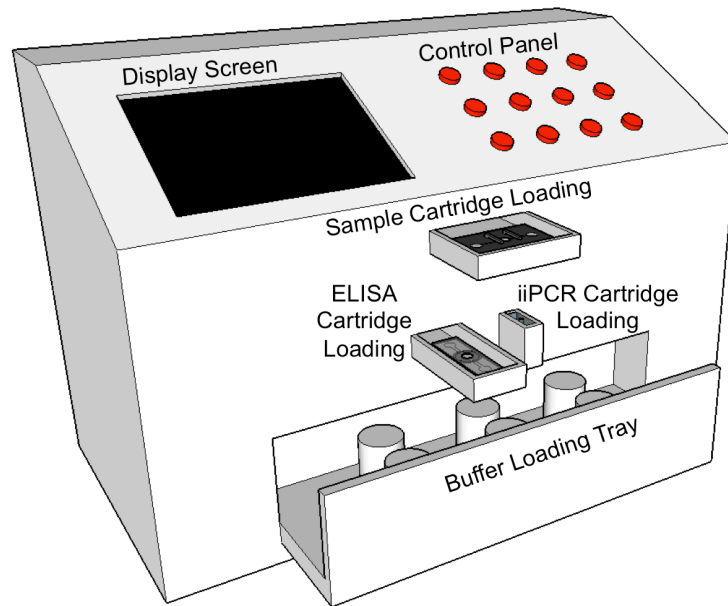


Figure 8.7: Basic schematic of instrument design. The instrument contains three drawers for loading each cartridge and a buffer loading tray. Results from the automated sample analysis are displayed on the built-in screen.

Summary and Outcomes

The work proposed here would involve the development of a user-friendly system for the diagnosis of FIV in cats. The system would provide the ability to distinguish between vaccinated and infected cats in a cohesive manner using ELISA as a screening step followed by iiPCR to confirm the presence of the virus. Accurate, rapid, and inexpensive diagnosis using the system proposed would help limit the spread of FIV in the feline population while preventing the unnecessary euthanasia of vaccinated cats associated with current diagnostic techniques. Additionally, FIV has been studied as an animal model of HIV.^{4, 55-57} Development of this system for FIV diagnosis could be applied to analysis of HIV treatments to further advance HIV research.

REFERENCES

1. J. K. Yamamoto, H. Hansen, E. W. Ho, T. Y. Morishita, T. Okuda, T. R. Sawa, R. M. Nakamura and N. C. Pedersen, *Journal of the American Veterinary Medical Association*, 1989, **194**, 213-220.
2. F. Courchamp, N. G. Yoccoz, M. Artois and D. Pontier, *Epidemiology and Infection*, 1998, **121**, 227-236.
3. N. C. Pedersen, J. K. Yamamoto, T. Ishida and H. Hansen, *Veterinary Immunology and Immunopathology*, 1989, **21**, 111-129.
4. M. Bendinelli, M. Pistello, S. Lombardi, A. Poli, C. Garzelli, D. Matteucci, L. Ceccherininelli, G. Malvaldi and F. Tozzini, *Clinical Microbiology Reviews*, 1995, **8**, 87-112.
5. K. Hartmann, *Veterinary Journal*, 1998, **155**, 123-137.
6. K. Hartmann, *Veterinary Immunology and Immunopathology*, 2011, **143**, 190-201.
7. P. C. Crawford and J. K. Levy, *Veterinary Clinics of North America-Small Animal Practice*, 2007, **37**, 335-+.
8. T. P. Oconnor, S. Tanguay, R. Steinman, R. Smith, M. C. Barr, J. K. Yamamoto, N. C. Pedersen, P. R. Andersen and Q. J. Tonelli, *Journal of Clinical Microbiology*, 1989, **27**, 474-479.
9. Q. J. Tonelli, *Journal of the American Veterinary Medical Association*, 1991, **199**, 1336-1339.
10. E. W. Uhl, T. G. Heaton-Jones, R. Pu and J. K. Yamamoto, *Veterinary Immunology and Immunopathology*, 2002, **90**, 113-132.
11. M. J. Hosie and J. A. Beatty, *Australian Veterinary Journal*, 2007, **85**, 5-12.
12. M. E. Westman, R. Malik, E. Hall, P. A. Sheehy and J. M. Norris, *Comparative Immunology Microbiology and Infectious Diseases*, 2015, **42**, 43-52.
13. V. Linder, S. K. Sia and G. M. Whitesides, *Analytical Chemistry*, 2005, **77**, 64-71.
14. D. Juncker, H. Schmid, U. Drechsler, H. Wolf, M. Wolf, B. Michel, N. de Rooij and E. Delamarche, *Analytical Chemistry*, 2002, **74**, 6139-6144.
15. L. Clime, D. Brassard, J. P. Pezacki and T. Veres, *Microfluidics and Nanofluidics*, 2012, **12**, 371-382.
16. J. Kim, E. C. Jensen, A. M. Stockton and R. A. Mathies, *Analytical Chemistry*, 2013, **85**, 7682-7688.
17. H. Tachibana, M. Saito, S. Shibuya, K. Tsuji, N. Miyagawa, K. Yamanaka and E. Tamiya, *Biosensors & Bioelectronics*, 2015, **74**, 725-730.

18. N. C. Cady, S. Stelick, M. V. Kunnavakkam and C. A. Batt, *Sensors and Actuators B-Chemical*, 2005, **107**, 332-341.
19. K. Hartmann, P. Griessmayr, B. Schulz, C. E. Greene, A. N. Vidyashankar, O. Jarrett and H. F. Egberink, *Journal of Feline Medicine and Surgery*, 2007, **9**, 439-445.
20. C. M. Cheng, A. W. Martinez, J. L. Gong, C. R. Mace, S. T. Phillips, E. Carrilho, K. A. Mirica and G. M. Whitesides, *Angewandte Chemie-International Edition*, 2010, **49**, 4771-4774.
21. X. Y. Liu, C. M. Cheng, A. W. Martinez, K. A. Mirica, X. J. Li, S. T. Phillips, M. Mascarenas, G. M. Whitesides and Ieee, Cancun, MEXICO, 2011.
22. S. M. Wang, L. Ge, X. R. Song, J. H. Yu, S. G. Ge, J. D. Huang and F. Zeng, *Biosensors & Bioelectronics*, 2012, **31**, 212-218.
23. R. C. Murdock, L. Shen, D. K. Griffin, N. Kelley-Loughnane, I. Papautsky and J. A. Hagen, *Analytical Chemistry*, 2013, **85**, 11634-11642.
24. Y. H. Chen, Z. K. Kuo and C. M. Cheng, *Trends in Biotechnology*, 2015, **33**, 4-9.
25. D. M. Cate, J. A. Adkins, J. Mettakoonpitak and C. S. Henry, *Analytical Chemistry*, 2015, **87**, 19-41.
26. Y. Y. Xia, J. Si and Z. Y. Li, *Biosensors & Bioelectronics*, 2016, **77**, 774-789.
27. J. Hu, S. Q. Wang, L. Wang, F. Li, B. Pingguan-Murphy, T. J. Lu and F. Xu, *Biosensors & Bioelectronics*, 2014, **54**, 585-597.
28. X. Li and X. Y. Liu, *Microfluidics and Nanofluidics*, 2014, **16**, 819-827.
29. A. W. Martinez, S. T. Phillips and G. M. Whitesides, *Proceedings of the National Academy of Sciences of the United States of America*, 2008, **105**, 19606-19611.
30. Y. Lu, W. W. Shi, L. Jiang, J. H. Qin and B. C. Lin, *Electrophoresis*, 2009, **30**, 1497-1500.
31. E. Carrilho, A. W. Martinez and G. M. Whitesides, *Analytical Chemistry*, 2009, **81**, 7091-7095.
32. Y. Lu, W. W. Shi, J. H. Qin and B. C. Lin, *Analytical Chemistry*, 2010, **82**, 329-335.
33. K. Yamada, T. G. Henares, K. Suzuki and D. Citterio, *Angewandte Chemie-International Edition*, 2015, **54**, 5294-5310.
34. W. H. Liang, C. H. Chu and R. J. Yang, *Talanta*, 2015, **145**, 6-11.
35. K. Maejima, S. Tomikawa, K. Suzuki and D. Citterio, *Rsc Advances*, 2013, **3**, 9258-9263.
36. K. Abe, K. Suzuki and D. Citterio, *Analytical Chemistry*, 2008, **80**, 6928-6934.
37. S. Jahanshahi-Anbuhi, A. Henry, V. Leung, C. Sicard, K. Pennings, R. Pelton, J. D. Brennan and C. D. M. Filipe, *Lab on a Chip*, 2014, **14**, 229-236.
38. E. Fu, B. Lutz, P. Kauffman and P. Yager, *Lab on a Chip*, 2010, **10**, 918-920.

39. S. Jahanshahi-Anbuhi, P. Chavan, C. Sicard, V. Leung, S. M. Z. Hossain, R. Pelton, J. D. Brennan and C. D. M. Filipe, *Lab on a Chip*, 2012, **12**, 5079-5085.
40. V. Leung, S. C. Johnstone, Y. Q. Xu, R. Pelton and C. D. M. Filipe, *Nordic Pulp & Paper Research Journal*, 2012, **27**, 814-819.
41. R. R. G. Soares, P. Novo, A. M. Azevedo, P. Fernandes, M. R. Aires-Barros, V. Chu and J. P. Conde, *Lab on a Chip*, 2014, **14**, 4284-4294.
42. R. J. W. Meesters and G. P. Hooff, *Bioanalysis*, 2013, **5**, 2187-2208.
43. T. W. McDade, S. Williams and J. J. Snodgrass, *Demography*, 2007, **44**, 899-925.
44. A. Sharma, S. Jaiswal, M. Shukla and J. Lal, *Drug Testing and Analysis*, 2014, **6**, 399-414.
45. R. P. Wilkes, S. A. Kania, Y. L. Tsai, P. Y. A. Lee, H. H. Chang, L. J. Ma, H. F. G. Chang and H. T. T. Wang, *Journal of Veterinary Diagnostic Investigation*, 2015, **27**, 510-515.
46. T. Hohdatsu, M. Yamada, M. Okada, M. Fukasawa, K. Watanabe, T. Ogasawara, M. Takagi, C. Aizawa, M. Hayami and H. Koyama, *Veterinary Microbiology*, 1992, **30**, 113-123.
47. T. Ohkura, Y. S. Shin, N. Wakamiya, N. Iwa and T. Kurimura, *Experimental Animals*, 1997, **46**, 31-39.
48. Y. L. Tsai, Y. C. Lin, P. H. Chou, P. H. Teng and P. Y. Lee, *Journal of Virological Methods*, 2012, **181**, 134-137.
49. H. F. G. Chang, Y. L. Tsai, C. F. Tsai, C. K. Lin, P. Y. Lee, P. H. Teng, C. Su and C. C. Jeng, *Biotechnology Journal*, 2012, **7**, 662-666.
50. Y. L. Tsai, H. T. T. Wang, H. F. G. Chang, C. F. Tsai, C. K. Lin, P. H. Teng, C. Su, C. C. Jeng and P. Y. Lee, *Plos One*, 2012, **7**, 10.
51. J. S. Yang, R. V. English, W. Ritchey, M. G. Davidson, T. Wasmoen, J. K. Levy, D. H. Gebhard, M. B. Tompkins and W. A. F. Tompkins, *Journal of Virology*, 1996, **70**, 3011-3017.
52. *Netherlands Pat.*, 1972.
53. I. Aziah, M. Ravichandran and A. Ismail, *Diagnostic Microbiology and Infectious Disease*, 2007, **59**, 373-377.
54. S. F. Cheung, S. K. L. Cheng and D. T. Kamei, *Jala*, 2015, **20**, 316-333.
55. B. J. Willett, J. N. Flynn and M. J. Hosie, *Immunology Today*, 1997, **18**, 182-189.
56. J. K. Yamamoto, M. P. Sanou, J. R. Abbott and J. K. Coleman, *Current Hiv Research*, 2010, **8**, 14-25.
57. M. J. Burkhard and G. A. Dean, *Current HIV Research*, 2003, **1**, 15-29.

CHAPTER 9. CONCLUSION

There is an existing need to advance the development of tools and techniques for biomarker detection. Necessary improvements include increasing accessibility of the devices by decreasing cost and improving portability and ease-of-use, and improving the sensing capabilities of the platform by increasing sensitivity and selectivity. Interfacing electrochemistry and microfluidics provides access to tools for improving biosensor systems by generating tunable platforms for a wide variety of bioanalytical applications. The microfluidic components allow improvements in cost and portability through the ability to manipulate small volumes of fluids, enabling system miniaturization. Electrochemical systems offer improvements in the field of biosensors by providing detection of a wide variety of biomarkers with high sensitivity and selectivity. By interfacing electrochemical detection systems with microfluidic devices, new tools and techniques can be developed for use in bioanalytical applications.

The work presented in this thesis detailed three main tools developed for biomarker detection using microfluidic electrochemical sensors. First, a mechanism for fluid transport was described.¹ Utilization of a degassed PDMS pump in a microfluidic device provided a simple, user-friendly, inexpensive, portable method to generate flow in a microfluidic channel after controlled extraction from a dried filter sample. This tool expanded on existing technology utilizing degassed PDMS for fluid transport, but increased the amount of control that the user has over the system. The degassed PDMS pump could be further employed in other microfluidic systems as portable fluid transport mechanism.

Second, a microfluidic device containing functionalized gold electrodes for impedance-based sensing was reported.² The simple electrode functionalization steps with DNA provided a highly selective detection motif for C-reactive protein using electrochemical impedance spectroscopy. Due to the electrode modification process, translation of this platform to detect other relevant proteins would be simple. Furthermore, developing the described system into a

multiplexed detection platform would be straightforward, allowing simultaneous, selective detection of multiple biomarkers using electrochemical impedance spectroscopy at DNA-modified gold electrodes.

Lastly, a high-density platinum microelectrode array was designed and interfaced with PDMS microfluidic devices for high spatiotemporal imaging of biomarker release from live tissue slices.^{3, 4} Miniaturization of platinum electrodes on a silicon microchip provided an array of sensors of adequate size to accommodate a live murine adrenal tissue slice and achieve spatial resolution across the different regions of the tissue. Microfluidic systems interfaced directly with the microchip and tissue slice to provide precise spatial and temporal control of fluid delivery, which can allow a more thorough investigation of how chemical gradients drive biological processes. With further development, the electrochemical imaging platform described could be adapted for sensing with higher selectivity. For example, fast scan cyclic voltammetry could be employed at each electrode to obtain resolution between catecholamines released from adrenal slices to understand how chemical gradients interact with one another and drive the biology of the tissue. Alternatively, electrode modifications could provide chemical imaging of electrochemically inactive biomarkers, or multiplexed detection across the array.

Future Directions

All of the systems described in this work aimed at interfacing electrochemical detection with microfluidic devices to generate additional tools for biomarker detection. While each tool was described within the context of a specific system, they each were designed to be translatable to other biologically relevant systems to continue to advance bioanalytical sensing. Additional improvements must be implemented to maximize the potential of each system before they can be widely utilized in the scientific community. For example, the high-density electrode arrays described were fabricated using processes intended for microchips in consumer electronics, not for direct contact with biological samples and extended exposure to aqueous

samples. As a result, the microchips have very limited lifetimes as biosensors, necessitating development of post-production treatments to extend their compatibility with aqueous environments to access long-term experiments.

The field of microfluidics has recently been rapidly advancing due to the progression of 3D printing technology. Although 3D printers were first developed in the 1980s, it was only recently that advancements in technology have made them feasible for device prototyping in a research laboratory. Specifically, with improvements in the resolution capabilities of commercially available printers, 3D printed microfluidic devices have gained significant attention. Work in this dissertation employed 3D printed parts with limited utility. The extrusion printer (A-101, Lulzbot, Loveland, CO, US) was unable to print enclosed channels due to ceiling collapse, and had limited resolution capabilities, and as result was exclusively used to print manifolds for device alignment and enclosure. Alternatively, technology has recently advanced stereolithography 3D printers to bring them into a market feasible for microfluidic device prototyping in research laboratories.

Initial investigation has begun in the Henry Laboratory using a Form 1+ (Formlabs, Somerville, MA, US) to generate 3D printed microfluidic devices for bioanalytical applications. The printer is able to achieve 300 μm resolution in the XY-plane, and 25 μm resolution in the Z-direction, allowing direct printing of enclosed microfluidic channels. Proof-of-concept devices have been printed to demonstrate the feasibility of using the 3D printer for bioanalytical microfluidic experiments. The first device, shown in Figure 9.1, contained four separate microfluidic channels connecting to a common well at the center of the device. In the figure, each channel contains a different color of dye solution for visualization. This aims to demonstrate that a live tissue sample could be incorporated into the well, and samples could be taken from four different locations on the tissue to achieve spatial resolution. Using 3D printing, this device could be advanced with simple changes, allowing sampling from many more points within the well. Unlike in conventional microfluidic devices, overlapping channels exiting from a

common well would not be a concern, as center channels could be easily dropped to a lower Z-position during the fabrication step. Fabrication of 3D microfluidic networks using conventional methods is challenging and time-consuming, but 3D printing makes it simple to create complicated 3D microfluidic networks.

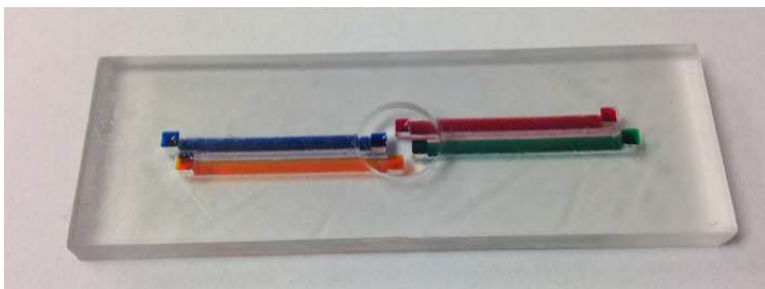


Figure 9.1: 3D printed microfluidic device. Four channels, each containing a different color dye solution for visualization, are connected to a common well and are individually accessible to demonstrate spatially resolved sampling from a biological sample, such as a live tissue slice.

A second, more complicated device was printed to control exposure of live tissue slices to two different controlled environments simultaneously. The device, shown in Figure 9.2, was composed of two separately printed parts, each containing a microfluidic channels. In each part, the microfluidic channel reached across the width of the device and passed a reservoir at the center. A tissue slice would act as a barrier between the two separate solutions when they reached the center reservoir, allowing each face of the tissue to be exposed to a different aqueous environment. Perpendicular alignment of the microfluidic channels upon device assembly would allow interfacing with external tubing to provide solution delivery to the microfluidic device.

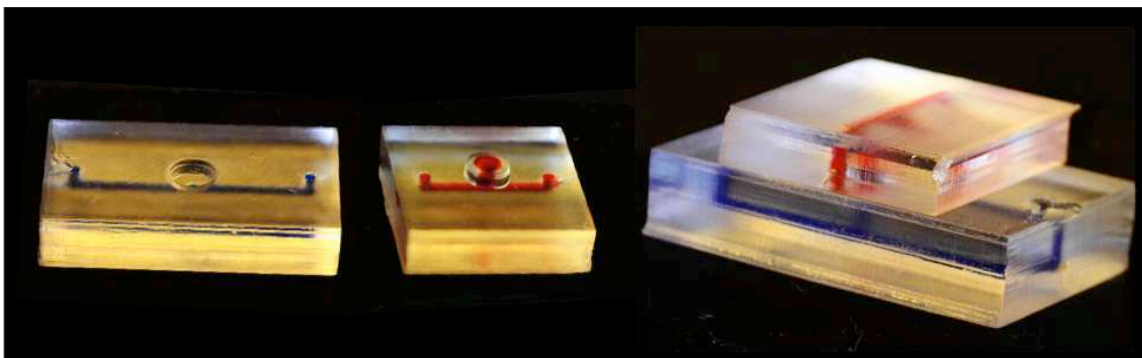


Figure 9.2: Two-part 3D printed microfluidic device. The left side of the figure shows the two individual microfluidic components, each containing a different color dye for visualization. The right side of the figure shows the two microfluidic channels assembled together into one device to provide fluid delivery to opposite sides of a live tissue slice.

Further development of 3D printed microfluidic devices could include incorporation of electrodes into the devices for electrochemical biomarker detection. The combination of improved resolution capabilities, decreased cost, and an increase in the materials available for printing make 3D printing a feasible option for advancing the field of electrochemical microfluidic biosensors.

With the existing need for implementation and accessibility to biosensor systems for an expanding range of bioanalytical applications, the continuing advancement of sensor technology is critical. Newly developed tools and those adapted from existing systems can be used to generate advanced systems to further our understanding of the complexity of the relationship between chemical and biological systems.

REFERENCES

1. R. M. Feeny, N. L. Puissant and C. S. Henry, *Analytical Methods*, 2016, DOI: 10.1039/c6ay01880g.
2. T. Songjaroen, R. M. Feeny, M. M. Mensack, W. Laiwattanapaisal and C. S. Henry, *Sensing and Bio-Sensing Research*, 2016, **8**, 14-19.
3. R. M. Feeny, J. B. Wydallis, T. Chen, S. Tobet, M. M. Reynolds and C. S. Henry, *Electroanalysis*, 2014, **26**.
4. J. B. Wydallis, R. M. Feeny, W. Wilson, T. Kern, T. Chen, S. Tobet, M. M. Reynolds and C. S. Henry, *Lab on a Chip*, 2015, **15**, 4075-4082.